

A COMBINED HYDROGRAPHIC, ADCP AND ALTIMETRIC

DESCRIPTION OF THE AGULHAS RETROFLECTION

by

Kathryn Ozimek

SCHOOL OF OCEAN AND EARTH SCIENCES AND TECHNOLOGY

UNIVERSITY OF HAWAII AT MANOA

1991

UNIVERSITY OF HAWAII AT MANOA

**A COMBINED HYDROGRAPHIC, ADCP AND ALTIMETRIC
DESCRIPTION OF THE AGULHAS RETROFLECTION**

A thesis submitted in partial fulfillment

of the requirements for the degree

Master of Science in Oceanography

by

Kathryn Ozimek

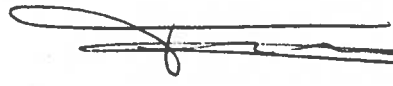
Thesis committee:

Pierre Flament, Chairman
Eric Firing
Gary Mitchum

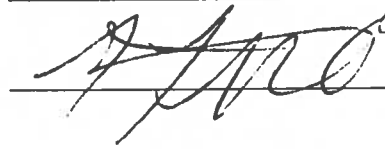
1991

We certify that we have read this thesis and that, in our opinion, it is satisfactory in scope and quality as a thesis for the degree of Master of Science in Oceanography.

THESIS COMMITTEE


P. FLAMENT
Chairperson


Eric Firing


G. Mitchum

ACKNOWLEDGEMENTS

I would first like to express my gratitude to God and my family, especially my husband, my parents and Hank and Janice Ozimek for their love and support in helping me to complete this paper.

I appreciate the insight and helpful advice that each of my committee members has given me throughout this project. I would like to thank Pierre Flament for offering me the opportunity to continue the work on the Agulhas Current that he had started at the Woods Hole Oceanographic Institution and for his generous support of this work. I also thank Eric Firing, for guiding me through the complexity of the ADCP processing, Gary Mitchum, for letting me use his processed GEOSAT data, and Julie Ranada and Willa Zhu, for sharing their programming expertise.

I would also like to thank Dr. J. Luyten, from Woods Hole Oceanographic Institution, who initiated the Agulhas Retroflection Experiment and without whom the rich data set used here would not have been collected, Dr. Raymond Pollard, from the Institute of Ocean Science, who provided both the SeaSoar and ADCP data, and his co-workers Jane Reid and Gwyn Griffiths, for many clarifications. The Agulhas Retroflection Experiment was funded by the Office of Naval Research under the Southern Atlantic Accelerated Research Initiative.

ABSTRACT

Acoustic Doppler Current Profiler (ADCP) and hydrographic data from a 1987 RRS Discovery cruise in the Agulhas retroflection is used to compute absolute sea level along ship tracks which coincide with GEOSAT ground tracks. Combination of this one-time absolute sea level with GEOSAT relative sea level measurements yields a mean sea surface height along each track. Ageostrophic effects and measurement uncertainties are estimated to contribute a 12.5% or smaller error to the mean sea level difference across the Agulhas current in the retroflection region. The mean sea surface height is then added to GEOSAT relative sea level data to produce a two year time series of absolute sea level along each track. Unlike the relative current flow usually available from GEOSAT measurements, absolute current flow computed from the absolute height time series can be used to calculate current transports and detect changes in the absolute flow of the Agulhas current.

TABLE OF CONTENTS

	Page
Acknowledgements	iii
Abstract	iv
List of tables	vii
List of figures	viii
1. Introduction and overview	1
Figure for chapter 1	3
2. Conceptual background	4
3. Description of the data	6
3.1. ADCP data	6
3.2. SeaSoar data	6
3.3. GEOSAT data	7
3.4. Current meter moorings	9
3.5. Gridding of data	9
Figures for chapter 3	10
Table for chapter 3	15
4. Scale of ageostrophic effects	16
4.1. Divergent flow	16
4.2. Balance of terms in the momentum equation	16
4.2.1. Time change term	17
4.2.2. Advection terms	17
4.2.3. Coriolis and pressure gradient terms	18
4.2.4. Friction terms	18
4.3. Comparison between ADCP and SeaSoar data	19

4.4. Summary on ageostrophic scaling	21
Figures for chapter 4	22
Table for chapter 4	26
5. Discussion of ageostrophic effects	27
5.1. Cyclostrophy	27
5.2. Ekman flow	30
5.3. Internal waves	30
5.4. Depth dependence of ageostrophic effects	32
5.5. Conclusion on ageostrophic effects	33
Figures for chapter 5	34
6. Results	43
6.1 Mean sea surface height	43
6.2 Time series of absolute flow in the Agulhas	45
6.3 Transport time series	46
6.4 Summary of results	46
Figures for chapter 6	48
7. Final conclusions	57
Appendix A	58
Appendix B	68
References	125

LIST OF TABLES

	Page
1. GEOSAT processing steps	15
2. Estimated magnitude of terms in the momentum equation	26
B-1. Velocity errors resulting from misalignment	124

LIST OF FIGURES

		Page
1.	Positions of the moorings, mean currents at the upper instruments (solid: 200m, dashed: 750m), and cruise tracks along which simultaneous SeaSoar and ADCP data were collected. The overlay shows the distribution of GEOSAT ground tracks. Note the close correspondence between the moored grid and the orbit grid over the retroflection.	3
2.	Labeled tracks of ADCP and SeaSoar data collection.....	10
3.	Time series of GEOSAT-measured relative sea level (in meters) by cycle number for the first 10 cycles (November 1986-April 1987) at selected points on tracks 2 and 3. The times at which the ship crossed these points are indicated by dotted lines.....	11
4.	GEOSAT-measured RMS variability, ranging from 0.1 to 0.45 meters, plotted on a map of tracks 2-5.	12
5.	GEOSAT relative sea level measurements along tracks 2-5. Solid line is the time-interpolated sea level at the time of ship passage. Dot-dashed and dashed lines are measured sea level during preceding and following GEOSAT passes.	13
6.	Velocity Shears between 25 and 150 meters and between 50 and 150 meters for (a) section 2, (b) section 3, (c) section 4 and (d) section 5. Solid lines represent velocity shears measured by ADCP. Dotted lines represent geostrophic velocity computed from SeaSoar densities.	22
7.	Diagram showing unit vectors in natural coordinates.	34
8.	Residual velocities along (a) track 2, (b) track 3, (c) track 4 and (d) track 5 after removing the vertical mean. Northward velocity vectors point upward. Constant rotation with depth or along track probably reflects inertial oscillation.	35
9.	Geopotential Anomaly in m^2s^{-2} between 25 and 150 meters and between 50 and 150 meters along (a) section 2, (b) section 3, (c) section 4 and (d) section 5. Solid lines represent anomalies computed from ADCP velocity shears. Dotted lines represent anomalies computed from SeaSoar densities.	37
10.	Sea surface height along (a) section 2, (b) section 3, (c) section 4 and (d) section	

	5. Solid lines represent heights calculated from near-surface ADCP velocities. Dotted lines represent heights calculated from ADCP velocities at 150 m and geopotential difference from 150 m to the surface from SeaSoar densities.	41
11.	Mean sea surface height and GEOSAT-measured RMS variability along (a) section 2, (b) section 3, (c) section 4 and (d) section 5.	48
12.	Mean sea surface height and resulting mean cross-track current plotted on a map of tracks 2-5. Overlay shows mean current at approximately 200 m (dashed) and 750 m (solid) measured by moored current meters.	52
13.	Time series of absolute sea surface height slope along (a) track 2, (b) track 3, (c) track 4 and (d) track 5. This slope is directly proportional to absolute current flow across the tracks. Gaps in GEOSAT data are unshaded.	53
14.	Smoothed absolute sea surface height difference between selected points on (a) section 2, (b) section 3, (c) section 4 and (d) section 5. Absolute height difference serves as an index for transport across the section. Breaks in plots are GEOSAT data gaps.	55
A-1.	Numbered GEOSAT tracks near South Africa. A typical position of the Agulhas current is depicted.	61
A-2.	Un-filtered (a), smoothed (b) and rms slope of (c) significant wave height along GEOSAT track d006, pass 034 (June 9, 1988). Height is in decimeters; slope is in decimeters/degree latitude.	62
A-3.	Representative plots of significant wave height rms slope (in decimeters/degree latitude) for individual passes along the tracks.	64
A-4.	Representative plots of average significant wave height (in decimeters) and rms slope (in decimeters/degree latitude).	66
B-1.	Summary of ADCP processing steps.	76
B-2.	Amplitude, DS8701.	77
B-3.	Percent Good, DS8701.	77
B-4.	W component, DS8701.	78
B-5.	Error velocity, DS8701.	78
B-6.	U component, DS8701.	79
B-7.	V component, DS8701.	79
B-8.	Numbered sections of ship track.	80
B-9.	Average reference layer velocity between fixes (piecewise constant) and the final, smoothed reference layer velocity.	81

B-10. Absolute current velocity vectors computed from the ADCP data. 94

B-11. Two sets of contoured cross-track velocities, one set of absolute velocities and
one set of relative velocities referenced to 200 meters. 99

CHAPTER 1

INTRODUCTION AND OVERVIEW

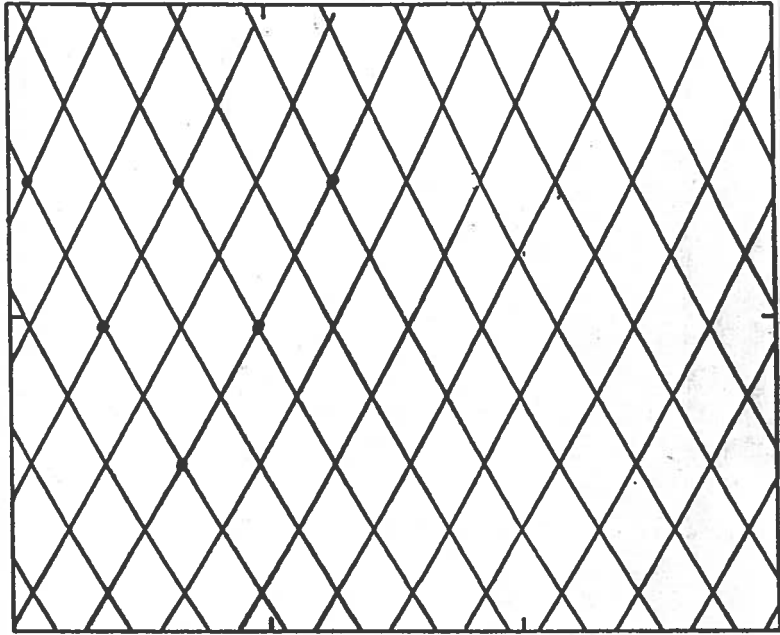
The Agulhas Current is the western boundary current in the subtropical gyre of the South Indian Ocean. It is a deep, strong flow, with typical velocities exceeding 2 m/s along the eastern coast of South Africa. Although it has not been studied as much as other western boundary currents, it has several unique features which make it particularly interesting. One such feature, the Agulhas Retroflexion, is an area where this strong current completely reverses direction. Once it reaches the end of the South African continental boundary, it is deflected eastward along the Antarctic Circumpolar Current. Then the Agulhas makes a sharp turn northward, apparently diverted around the Agulhas Plateau, a topographic feature at about 2500 meters depth. Eddies are often formed through changing paths of the retroflexion. Some of them travel up the South African west coast into the Atlantic Ocean and may be a significant path of water exchange between the Indian and Atlantic Oceans. Yet another reason for interest in the Agulhas Current is the unusually steep, high waves that have been reported by ships in the region (see appendix A for details). Possible explanations for these waves range from superposition of numerous storm swells following specific weather patterns (Mallory, 1974) to wave refraction resulting from the curvature of the current (Irvine, 1987). Understanding in these areas of interest would be enhanced by more complete data on the velocity field.

Satellite altimetry is a convenient way to collect large amounts of sea surface height data from which velocity can be computed. Repeated samples can be taken over long periods of time with an altimeter that would be impossible to obtain with traditional shipboard methods. Its main drawback, however, is that in practice, the altimeter only gives us surface height relative to the mean. The earth's geoid signal (~ 60 m) is much larger than that of the ocean surface (~ 60 cm), and it is poorly known. Therefore, processing altimeter data involves removal of the mean signal to eliminate the earth's geoid. Unfortunately, this process also removes the mean ocean signal, leaving only relative surface measurements from which relative current velocity is computed. Absolute current flow cannot be determined from the altimeter alone.

An extensive observational program to study the currents in the Agulhas retroflexion was conducted from 1985 to 1987 (Luyten *et al.*, 1990). An array of ten subsurface moorings was deployed in 1985 in the positions shown in Fig. 1. Recovery of the moorings was accomplished in February 1987 during RRS Discovery Cruise 165A. During the cruise, simultaneous SeaSoar hydrographic sections and Acoustic Doppler Current Profiles (ADCP) were collected between the moorings.

GEOSAT Altimeter data taken at the time of the 1987 cruise is also available. Four sections of the cruise track along which SeaSoar and ADCP data were taken nearly coincide with orbit ground tracks (see overlay for Fig. 1). The simultaneous altimeter, ADCP and hydrographic measurements collected during the 1987 Discovery cruise in the Agulhas region present an excellent opportunity to calculate a mean sea level along these tracks. The objectives of this work are to obtain a mean sea level, assess its potential errors and combine the result with GEOSAT data to produce a time series of absolute current flow across each of these four sections of the Agulhas retroflection.

Chapter 2 introduces the basic concepts and chapter 3 describes the data. Chapters 4 and 5 discuss potential errors due to ageostrophy, and could be skipped for a faster reading. Chapter 6 presents the results, followed by conclusions in chapter 7.



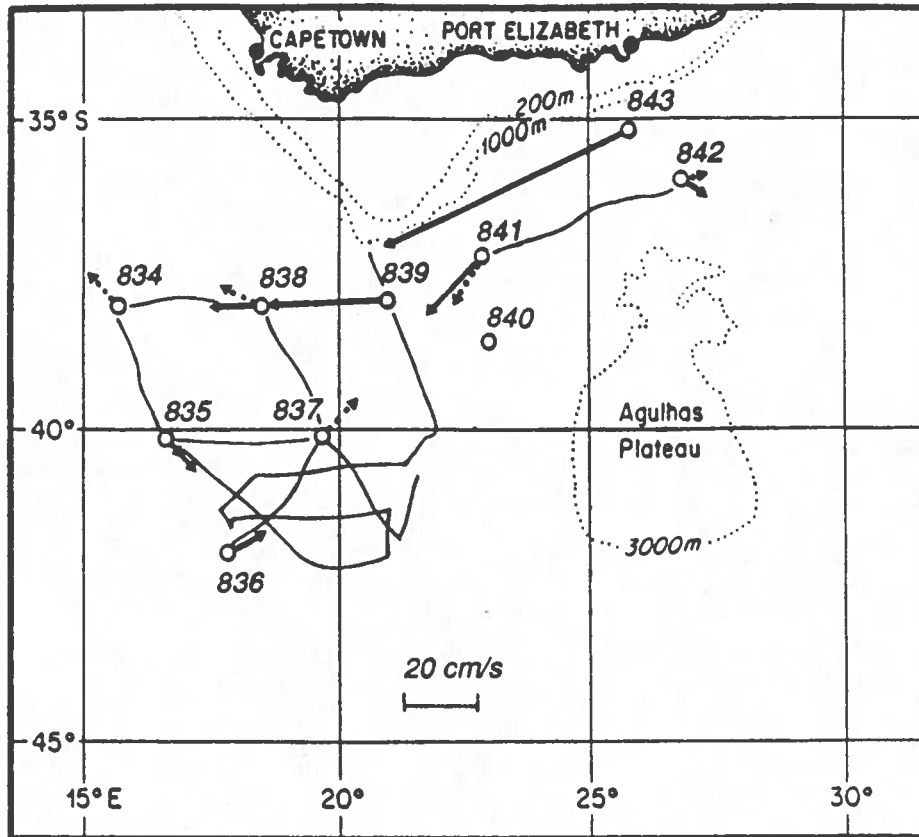


Fig. 1. Positions of the moorings, mean currents at the upper instruments (solid: 200m, dashed: 750m), and cruise tracks along which simultaneous SeaSoar and ADCP data were collected. The overlay shows the distribution of GEOSAT ground tracks. Note the close correspondence between the moored grid and the orbit grid over the retroflection.

CHAPTER 2

CONCEPTUAL BACKGROUND

Mean sea level can be calculated by combining GEOSAT and shipboard measurements. The altimeter-measured surface height $a(t)$ is equal to the sum of the geoid (G) and the ocean signal $h(t)$.

$$a(t) = G + h(t) \quad (2.1)$$

The geoid signal is much larger than the ocean signal, but does not vary in time. Therefore, the geoid is removed by first taking the time mean of the above equation,

$$\langle a(t) \rangle_t = G + \langle h(t) \rangle_t \quad (2.2)$$

and then subtracting the mean equation from the original one. The variation from the mean of a given altimeter measurement and/or ocean signal will be called relative sea level, $h'(t)$:

$$h'(t) = h(t) - \langle h(t) \rangle_t = a(t) - \langle a(t) \rangle_t \quad (2.3)$$

Since altimeter measurements can be averaged for the same point over many repeat cycles, $h'(t)$ can be determined from the altimeter. To determine the mean sea level for the period over which the altimeter was averaged, an independent estimate of $h(t_0)$ at some time (t_0) must be obtained from shipboard measurements.

The calculation of a proper absolute sea level from adcp and hydrographic data depends on the type of flow present in the region of study. A careful examination of the flow characteristics must be conducted to determine if geostrophic balance applies or if ageostrophic effects are important in the balance of forces. The y axis will be aligned with the along track direction and the y component of the horizontal momentum equation will be used to describe the motion:

$$\frac{\partial v}{\partial t} + u \frac{\partial v}{\partial x} + v \frac{\partial v}{\partial y} + w \frac{\partial v}{\partial z} + f u = -\alpha \frac{\partial p}{\partial y} + A_x \frac{\partial^2 v}{\partial x^2} + A_y \frac{\partial^2 v}{\partial y^2} + A_z \frac{\partial^2 v}{\partial z^2} \quad (2.4)$$

in which (u, v, w) is the velocity vector, f is the Coriolis parameter, α is the specific volume of water, p is the pressure and A_i are eddy viscosities. The first four terms in equation (2.4) represent acceleration in the rotating reference frame of the earth. $f u$ and $-\alpha \frac{\partial p}{\partial y}$ represent acceleration from the Coriolis and pressure gradient forces, respectively. The last three terms are parameterizations for acceleration due to friction. A full discussion of momentum equation terms and their relative

importance is provided in chapter 4.

A geostrophic balance neglects all non-linear and friction terms assuming them to be insignificant compared to the Coriolis and pressure gradient forces:

$$fu = -\alpha \frac{\partial p}{\partial y} \quad (2.5)$$

The pressure gradient term can also be expressed as a geopotential gradient:

$$-\alpha \left[\frac{\partial p}{\partial y} \right]_{\Phi} = - \left[\frac{\partial \Phi}{\partial y} \right]_p \quad (2.6)$$

At the ocean's surface (p_0),

$$\Phi_0 = g h \quad (2.7)$$

where h is the height of the ocean surface above $z=0$. Therefore, the geostrophic balance at the ocean's surface becomes

$$fu = -g \frac{\partial h}{\partial y} \quad (2.8)$$

and h at point B along the ship track can be expressed as follows.

$$h_B = \frac{-f}{g} \int_A^B u \, dy + h_A \quad (2.9)$$

Note that h_A is always an unknown reference level. However, only the slope of the height is important in determining current flow, and the slope is independent of the value chosen for h_A . If geostrophic balance is a valid assumption, then an $h(t_0)$ can be computed from surface ADCP velocity at the time of a survey. When $h(t_0)$ is combined with the GEOSAT-derived $h'(t_0)$, the mean sea level ($\langle h(t) \rangle_t$) for the averaging period of the altimeter can be obtained.

CHAPTER 3

DESCRIPTION OF THE DATA

A rich collection of data is available from the 1987 RRS Discovery cruise. The following paragraphs describe each type of data and discuss associated issues such as accuracy and resolution.

3.1. ADCP data

The Acoustic Doppler Current Profiler (ADCP) is a device which transmits sound pulses into the water and uses the Doppler frequency shift measured in returning sound signals to compute water velocity relative to the ship. Velocity measurements are vertically averaged into 8 meter bins. The maximum available depth range for this cruise is 16 to 408 meters, although quality data is generally only available between 24 and 200 meters. Satellite positioning and ship heading is recorded and used to obtain the ship track over the ground. Subtracting the ship speed over the ground from the relative velocity results in the final absolute current velocity. Because the absolute velocity is a small difference between two large vectors, small misalignment errors in the transducer or gyro compass can introduce significant error to the absolute velocity. As discussed in appendix B, absolute ADCP velocity is estimated to be accurate to within ± 13 cm/s. Most of this error results from alignment uncertainty. The spatial resolution of the ADCP data depends on a combination of the distance between satellite fixes and smoothing applied to the navigation data. Although it varies throughout the cruise, the average resolution of absolute current velocity is around 100 km. Fig. 2 shows the segments of straight ship track along which ADCP data is available for comparison to GEOSAT and SeaSoar data. Vector diagrams and contour plots of ADCP velocity as well as a more detailed description of the processing of ADCP data are provided in appendix B.

3.2. SEASOAR data

CTD measurements were taken by SeaSoar along most of the cruise track for which ADCP data were available, except the southern half of track 4 (labeled 4b in Fig. 2). The SeaSoar is a CTD device which is towed behind the ship and continuously ascends and descends between the surface and 350 meters depth. A more detailed description of SeaSoar data collection and calibration is provided in Read *et al.* (1987) and Pollard *et al.* (1987), from which the following summary was extracted.

Data were logged on a Neil Brown Instrument System deck unit, written to tapes for backup, displayed on a microcomputer and transferred to a PDP11/34 for editing, averaging and logging. Some spikes in the data were removed at this stage and the data were averaged to one sample per second. These averaged data were then calibrated. Every 12 hours, the files were merged with navigation, gridded and contoured. Primarily transit fixes were used, which were screened for bad fixes or fixes less than one hour from a better fix and edited. The final track used for gridding was produced by combining fixes with dead reckoning from the ship's calibrated electromagnetic log. The data were gridded into 4 km x 8 dbar boxes by directly averaging all one-second data cycles within each box. This typically included 16-24 measurements per gridded average. The gridded file was further smoothed by averaging over three adjacent columns (12 km) to minimize internal wave noise and permit meaningful geostrophic calculations. Smoothed files were subsampled every 4 km along-track.

Laboratory calibrations for pressure and temperature were used until the temperature sensor failed on 16 February (mid-way through track 4). The failed sensor was replaced by a spare platinum resistance thermometer, for which a calibration was derived using plotted T/S relations from Agulhas waters. No offsets were found between the final calibrated temperatures and the T/S curves from previous runs, which led Read *et al.* (1987) to assume that the new calibration was within 0.01° C, equivalent to the minimum detectable error in salinity. Relative salinity calibration was maintained through editing of plots which revealed salinity spikes or offsets larger than about 0.1. Absolute calibration was then accomplished through post-cruise reconciliation of the shallowest SeaSoar salinity reading (6 db) with bottle samples drawn hourly off the ship's uncontaminated water supply. The standard deviation of the difference between bottle and SeaSoar salinities led Read *et al.* (1987) to conclude that salinities were absolutely calibrated to within 0.015. These values of temperature and salinity error equate to a maximum density error of less than 0.009 kgm⁻³.

3.3. GEOSAT data

The GEOSAT altimeter has a 17-day exact repeat orbit with approximately 130-km track-to-track and 7-km along-track sampling in the study area. This orbit is ideal for studying strong, variable currents such as the Agulhas, because the orbital errors have large wavelengths (Cheney, 1989). Aliasing should also be minimal because power spectra of velocity variance based on current meter measurements show that most of the variability occurs at periods of 50-150 days (Luyten *et al.*, 1990), longer than twice the repeat cycle. Time series plots of the first 10 cycles (November 1986 to April 1987) at points along each track used for this study demonstrate variability on this time scale. Fig. 3 shows several examples of such time series. A map of RMS variability for November 1986 to

November 1988 along the four GEOSAT tracks corresponding to ship tracks is shown in Fig. 4.

GEOSAT data for this work was obtained from NOAA-NESDIS and processed by G. Mitchum. Table 1 summarizes the processing steps taken. A detailed description of the corrections applied can be found in the GEOSAT Altimeter GDR User Handbook (Cheney *et al.*, 1987). Most of the data corrections have signals with long wavelengths of about one orbit. Errors in the corrections are largely removed in adjustments for the orbit error, which also has a wavelength of about one orbit. Unlike most corrections, the wet tropospheric effect can be highly variable on spatial scales smaller than one orbit. However, the Agulhas Retroreflection region has relatively low atmospheric water vapor content (Stewart, 1985, Fig. 4.8) so the atmospheric model used to obtain the correction is considered accurate to within 5 cm for this area. Orbit errors are large for GEOSAT. Cheney *et al.* (1987) modeled orbit error over the Pacific ocean with a quadratic polynomial to evaluate its importance. After removal of the quadratic function from each pass in the test area (between 40°N and 40°S), the residual error was 7.5 cm rms. The Agulhas GEOSAT data were corrected for orbit error using a modulated, once around the earth harmonic, which is more accurate than a polynomial fit (Flament *et al.*, 1991). The maximum residual orbit error is therefore assumed to be 7.5 cm rms.

The mean altimeter measurement subtracted during GEOSAT processing was computed from 22 samples (see table 1). This sample mean may not be an accurate representation of the true mean ocean surface during the time span of sampling. Although the true distribution of sea level is not known, we can estimate the accuracy of our sample mean by assuming it is normal and random. The standard deviation for the mean of n independent normal distributions is $\frac{\sigma}{\sqrt{n}}$, where σ is the standard deviation of individual distributions. Using a typical rms variability of 0.3 m (Fig. 4) for σ , the standard deviation of the mean is 6.4 cm. Combining this range of error for the mean with GEOSAT instrument errors, the total rms error of the altimeter measurements is estimated to be ± 11 cm.

Noise dominates the GEOSAT along-track power spectrum of relative topography at wavenumbers higher than about $1/50 \text{ km}^{-1}$ (Flament *et al.*, 1989), so the effective spatial resolution of GEOSAT data is no better than 50 km. The median filter applied to the Agulhas data removes outliers from the data while still preserving smaller scale variability that would be lost in an averaging filter of the same size. Although the filter is approximately 80 km wide, the filtered data retain smaller spatial signals. Therefore, spatial resolution is limited by the measurement noise to approximately 50 km.

3.4. Current meter moorings

Fig. 1 shows the locations of the ten current meter moorings deployed in 1985 and recovered two years later during RRS Discovery cruise 165A. A complete description of current meter data collection and processing as well as various displays of the data are provided in Luyten *et al.* (1990), from which the following summary was extracted.

Two types of current meters were used on the moorings. The burst sampling meter (model 850) turns on at preselected time intervals and begins recording a sequence of strobes. One strobe contains temperature, another contains time, and the remainder are pairs of rotor counts and compass/vane readings. After the data are recorded on magnetic tape, the instrument turns off until the next activation time. The other type of meter, the vector averaging current meter, continuously sums vector increments of water flow sensed by the rotor and vane. It then records the data on a magnetic cassette tape at intervals set prior to deployment. Data from the tapes were edited to remove bad data points and launch/retrieval transients. Gaps were filled by linear interpolation and a Gaussian filter was applied to obtain a low-passed version of the data. This smoothed series was then subsampled once per day.

3.5. Gridding of data

Before combining ADCP, SeaSoar and GEOSAT data for calculation of mean sea level, the data were interpolated to a common grid. As mentioned previously, the GEOSAT spatial resolution is about 50 km. All offsets between ship tracks 2 through 5 (see Fig. 2) and corresponding GEOSAT tracks (Fig. 1) are less than 50 km. Therefore, corresponding ship and GEOSAT tracks were treated as if they coincided exactly. When combining different types of data for sea level calculations, ADCP data were linearly interpolated by latitude to the SeaSoar or GEOSAT latitude grid. GEOSAT data from successive repeat cycles were linearly interpolated in time to the time at which the ship passed the midpoint of the corresponding track (see Figs. 3 and 5a-5d).

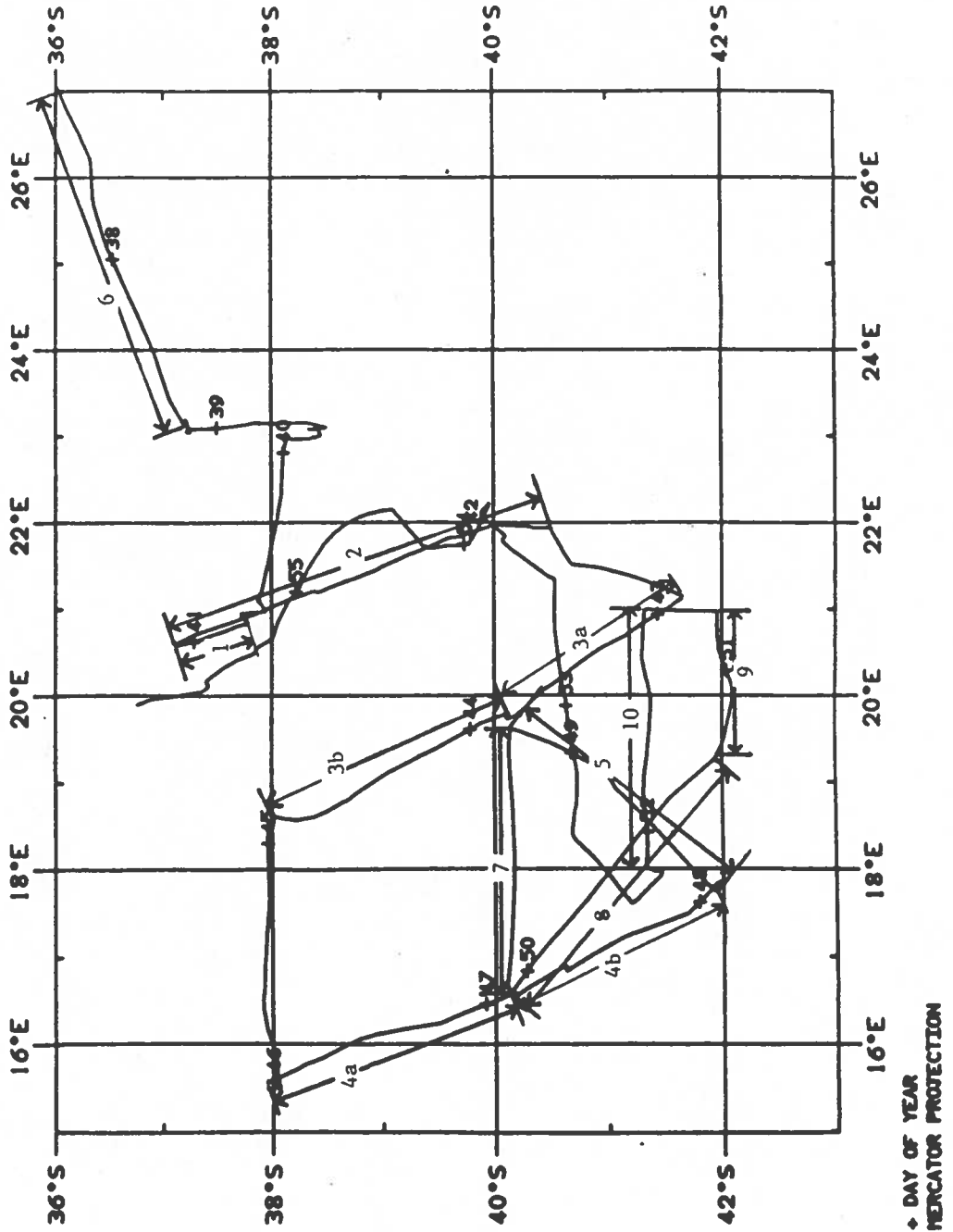


Fig. 2. Labeled tracks of ADCP and SeaSoar data collection.

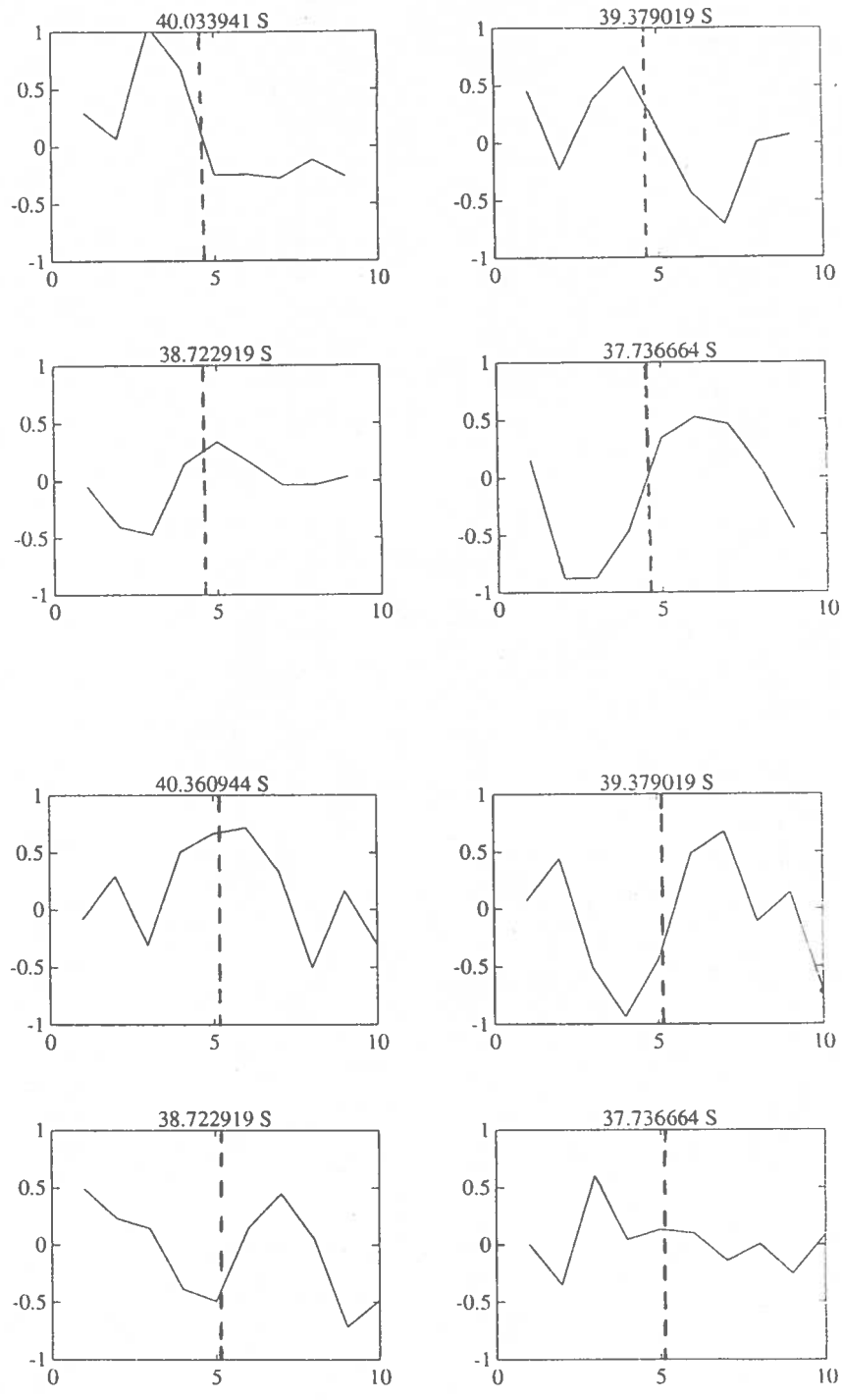


Fig. 3. Time series of GEOSAT-measured relative sea level (in meters) by cycle number for the first 10 cycles (November 1986-April 1987) at selected points on tracks 2 and 3. The times at which the ship crossed these points are indicated by dotted lines.

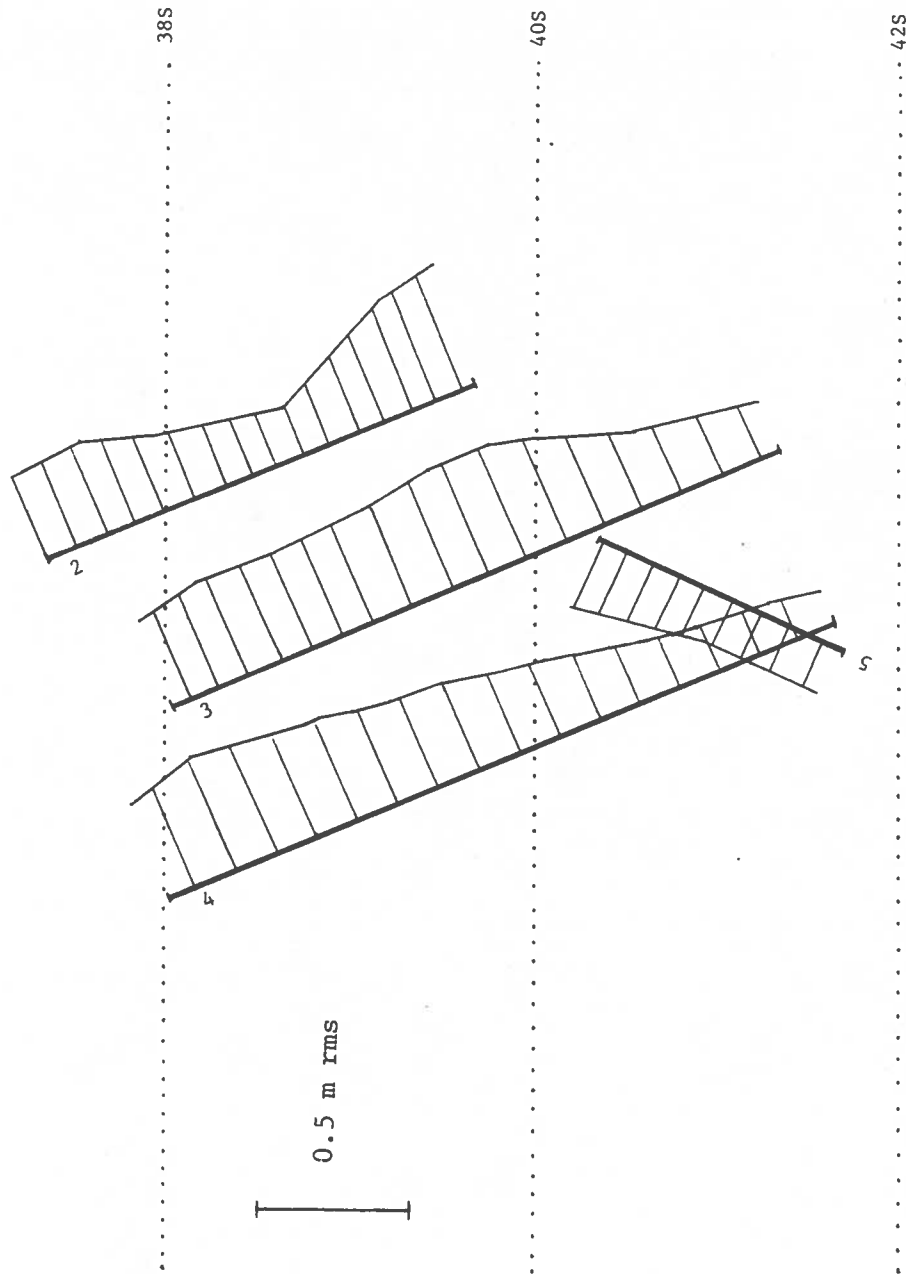


Fig. 4. GEOSAT-measured RMS variability, ranging from 0.1 to 0.45 meters, plotted on a map of tracks 2-5.

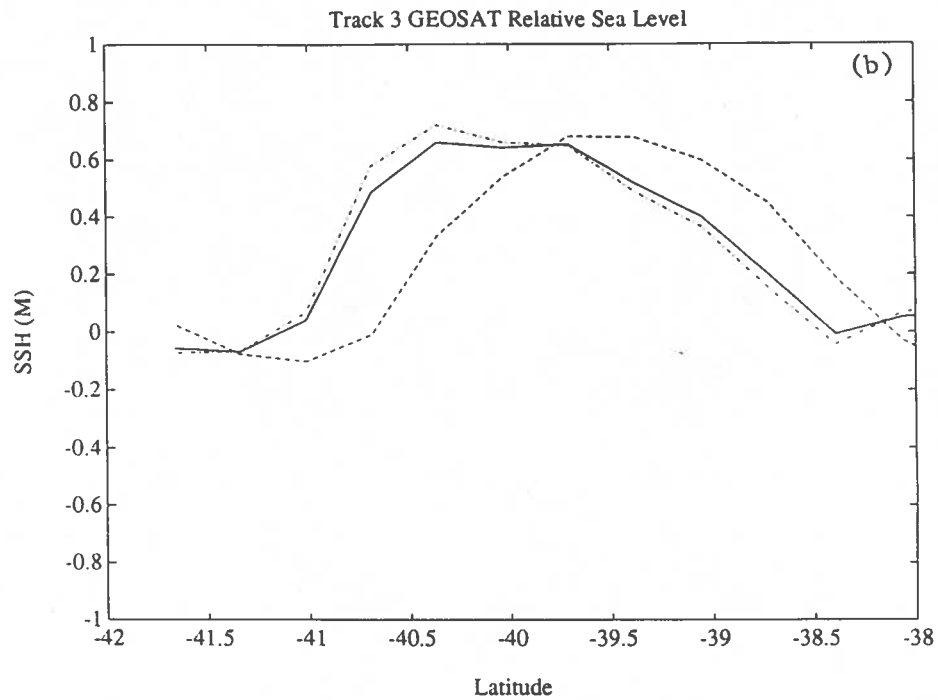
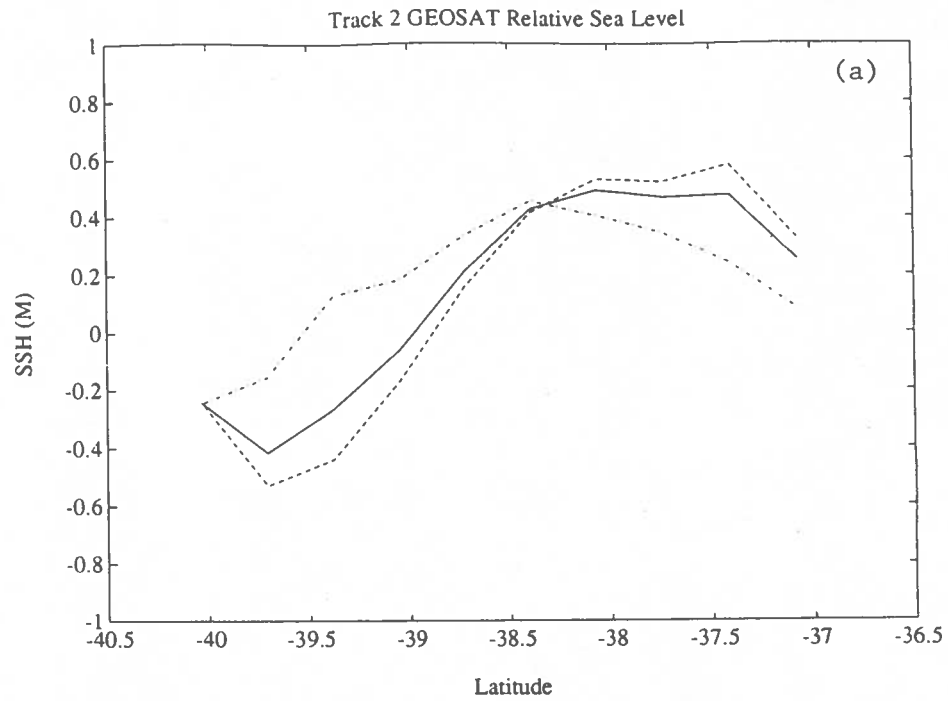


Fig. 5. GEOSAT relative sea level measurements along tracks 2-5. Solid line is the time-interpolated sea level at the time of ship passage. Dot-dashed and dashed lines are measured sea level during preceding and following GEOSAT passes.

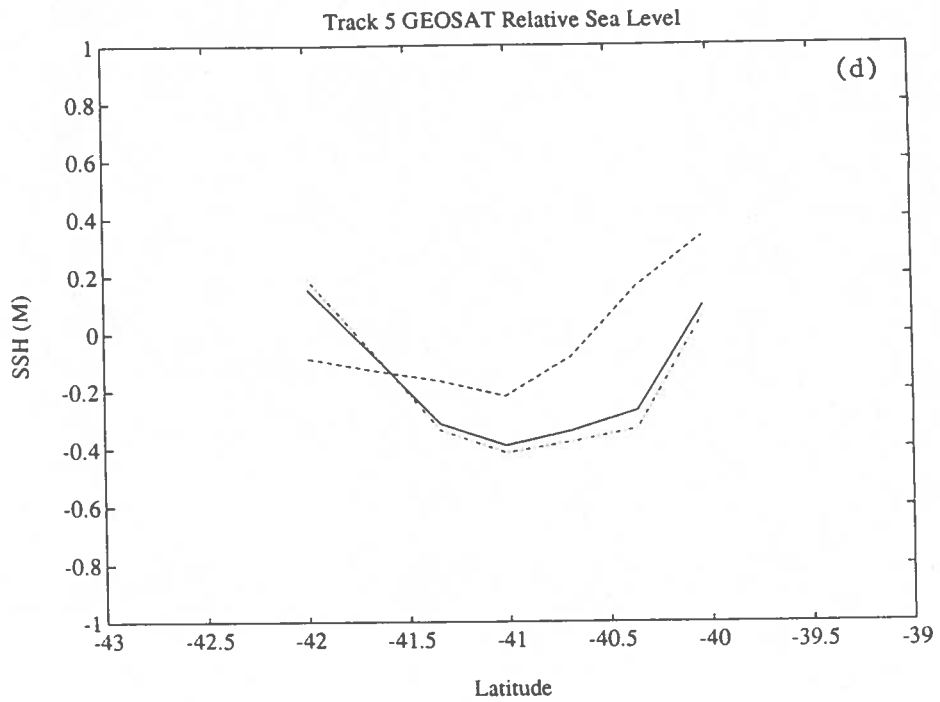
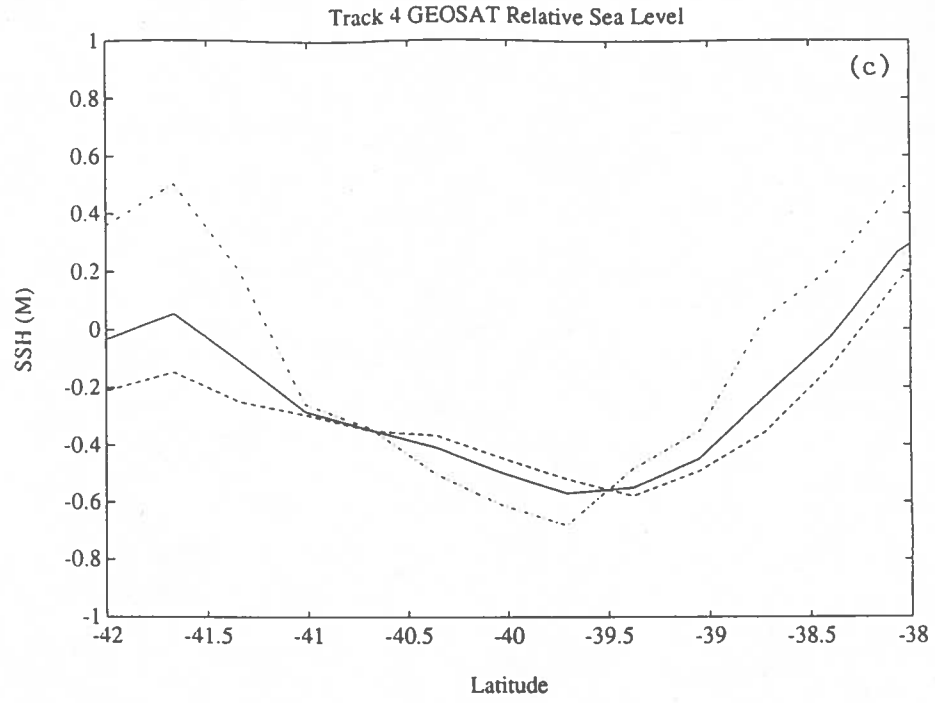


Table 1

GEOSAT Processing Steps

Number	Step Taken
1	Corrections provided by NOAA for ocean and earth tides, water vapor, tropospheric and ionospheric delays, surface pressure, and electromagnetic bias were applied.
2	Each profile was linearly interpolated to a common grid.
3	A reference cycle was subtracted from all other cycles to remove the geoid.
4	Several quality control checks were conducted on all data. Any arc which failed one or more of the checks was plotted and inspected visually. Glitches in the data were edited out.
5	Data were filtered using an 11 point median filter.
6	The data were subsampled every 6 points, leaving measurements about every 44 km.
7	The residual orbit error (with a period of approximately one orbit) was computed using a modulated harmonic fit and removed.
8	The temporal mean from the first year of GEOSAT operation (first 22 cycles) was removed.

CHAPTER 4

SCALE OF AGEOSTROPHIC EFFECTS

Before trying to determine what types of ageostrophic motion are present in the Agulhas, we will first look at the magnitude of ageostrophic effects. Evaluating the scale of ageostrophic effects is critical in assessing the validity of the geostrophic assumption. Several methods will be applied to the available data to estimate the importance of these effects.

4.1. Divergent flow

An initial check of the magnitude of non-geostrophic effects is to test for divergence. Since to the zeroth order, geostrophic flow is non-divergent, the integration of geostrophic current flow around a closed loop should ideally result in zero. Assuming the ADCP velocity field represents absolute velocity, an imbalance of integrated ADCP flow around a closed loop should represent ageostrophic flow. As Fig. 2 shows, ADCP data are available for several sets of nearly connecting sections on which this divergence can be tested. Using absolute current velocity from the ADCP between depths of 20 and 100 meters, the net transport balances around these loops range from -0.7 to $-4.1 \times 10^6 \text{m}^3 \text{s}^{-1}$. Loops which cover a larger time span (up to 68 hours) have the largest residual transports, and each of the loops have some missing data. Since the total ADCP-measured transport in the Agulhas over the same depth range and distance is between 14 and $50 \times 10^6 \text{m}^3 \text{s}^{-1}$ the divergent flow represents 10% or less of the measured current flow along any given loop. As discussed in chapter 3, small offsets of the ship's gyro or transducer can cause current velocity errors. Residual transports of 1 to $5 \times 10^6 \text{m}^3 \text{s}^{-1}$ could be caused by a consistent $1/2^\circ$ alignment error around the loops. Additionally, temporal changes in the flow during the time required for the ship to traverse the loop may contribute to apparent divergence. These errors may have similarly reduced the calculated divergence, but one could at least estimate the net ageostrophic effects to be 20% or less from this crude exercise.

4.2. Balance of terms in the momentum equation

The usual test of whether or not the geostrophic assumption is a good one is the balance of terms in the equation of motion. Table 2 lists the terms from equation (2.4) along with their estimated magnitude for the surface layer in the Agulhas retroflexion area. The shallowest ADCP-measured velocities (24 m) are assumed to be similar to the surface flow when making these

estimates. The value of each term divided by fu is also listed to clearly show the importance of the term relative to the Coriolis term. An explanation of how the estimates were obtained is provided below.

4.2.1. Time change term

$\frac{\partial v}{\partial t}$ was estimated using GEOSAT altimeter data over the first ten cycles (November 1986 - April 1987). The average change in sea surface slope at points along the tracks of interest was converted into an average velocity change between each cycle. Taking the time derivative of equation (2.8),

$$\frac{\partial u}{\partial t} = -\frac{g}{f} \frac{\partial}{\partial t} \left(\frac{\partial h}{\partial y} \right) \quad (4.5)$$

Although this method actually estimated $\frac{\partial u}{\partial t}$, the values for tracks 2-4 were indistinguishable from that of track 5, which is roughly perpendicular. Therefore, the $\frac{\partial u}{\partial t}$ and $\frac{\partial v}{\partial t}$ terms were assumed to be of the same order of magnitude.

4.2.2. Advection terms

Due to the high current speeds and small scale of the meanders of the Agulhas retroflection, horizontal advection terms ($u\frac{\partial v}{\partial x}$ and $v\frac{\partial v}{\partial y}$) may be important. The $v\frac{\partial v}{\partial y}$ term for tracks 2-5 was estimated directly from the ADCP along-track velocity and its change with distance travelled. Although $\frac{\partial v}{\partial x}$ could not be determined directly from ADCP data for tracks 2-5, it was estimated from crosstrack velocity variance along tracks 6-10, which are approximately perpendicular to tracks 2-5 (see Fig. 2). An average value of 1 m/s was used for u and v .

If the momentum balance at the ocean's surface is desired, w becomes zero, eliminating the vertical advection term. However, since the shallowest ADCP velocities available were actually measured at 24 meters rather than at the surface, an estimate of vertical advection was made. According to the continuity equation, the magnitude of $\frac{\partial w}{\partial z}$ can be estimated by horizontal divergence.

$$\frac{\partial u}{\partial x} + \frac{\partial v}{\partial y} = -\frac{\partial w}{\partial z} \quad (4.6)$$

Using the horizontal divergence calculated around closed loops in the upper 100 meters, $\frac{\partial w}{\partial z}$ was

estimated to be $4.5 \times 10^{-12} \text{s}^{-1}$. This yielded a w of about $-1.1 \times 10^{-10} \text{ m/s}$ at a depth of 24 m. Vertical shear was estimated from ADCP data, and combined with w to obtain a vertical advection term on the order of 10^{-13}ms^{-2} .

4.2.3. Coriolis and pressure gradient terms

Coriolis acceleration was estimated using f at a latitude of 40S and average velocity of 1 m/s. The pressure gradient term can be expressed in terms of geopotential gradient (eqn. 2.6). Close agreement between ADCP-measured and SeaSoar-calculated velocity shears to be discussed in section 4.3 (Figs. 6a-6d) demonstrates that the Coriolis and pressure gradient terms are of the same order of magnitude. Therefore, although a specific estimate of the pressure gradient term is not made, it is listed as order one relative to fu in table 2.

4.2.4. Friction terms

The friction terms as written in equation (2.4) are parameterizations of acceleration resulting from turbulent stresses, assumed to be related to the mean velocity gradient by an "eddy viscosity" (A). For example,

$$-\rho \overline{v'u'} = \rho A_x \frac{\partial \bar{v}}{\partial x} \quad (4.7)$$

Assuming the spatial variation in eddy viscosity is small relative to spatial velocity variation, the acceleration term is expressed as

$$\frac{\partial \overline{v'u'}}{\partial x} = A_x \frac{\partial^2 \bar{v}}{\partial x^2} \quad (4.8)$$

Values for horizontal eddy viscosity vary widely, and are difficult to determine accurately. The values used in this analysis were estimated using a rough scaling approach. The horizontal length scale of velocity variations in the retroreflection area is about 50 km. v' and u' were estimated to be about 10 cm/s, resulting in a horizontal eddy viscosity of roughly $500 \text{ m}^2 \text{s}^{-1}$. This estimate was combined with ADCP estimates of $\frac{\partial^2 v}{\partial x^2}$ and $\frac{\partial^2 v}{\partial y^2}$ to obtain the horizontal friction terms listed in table 2.

The dominant force creating vertical friction near the ocean surface is the wind. Vertical stress due to wind in the y direction can be expressed in three different ways:

$$-\rho \overline{v'w'} = \rho A_z \frac{\partial \bar{v}}{\partial z} = -\tau_y \quad (4.9)$$

Therefore, the vertical friction term in equation (2.4) can also be expressed in terms of τ_y .

$$A_z \frac{\partial^2 v}{\partial z^2} = -\frac{1}{\rho} \frac{\partial \tau_y}{\partial z} \quad (4.10)$$

Momentum generated at the ocean's surface is spread fairly evenly and quickly throughout the mixed layer, acting as a body force on the whole layer. As a result, in the mixed layer, $\frac{\partial \tau_y}{\partial z}$ becomes $\frac{\tau_y}{a}$ where a is the depth of the mixed layer (Pollard, 1970). Wind stress (τ) was estimated from the speed of the wind (W), density of air ($\rho_a = 1.3 \text{ kgm}^{-3}$) and a drag coefficient ($C_D \approx 1.2 \times 10^{-3}$):

$$\tau = \rho_a C_D W^2 \quad (4.11)$$

The average wind speed (in all directions) reported by ships passing near the area was 8 m/s (Comprehensive Ocean-Atmosphere Data Set, 1985). The 0.015 magnitude of the vertical friction term in the mixed layer was obtained using this wind speed with an average mixed layer depth (70 m) estimated from CTD casts during the cruise (Read *et al.*, 1987). The wind reported by ships may be a poor reflection of actual winds in the retroreflection region, as the main shipping route is close to the coast, and not many ships actually cross the retroreflection. Although wind was not recorded regularly in the available logs from RRS Discovery, one instance of heavy weather with a wind speed of 40 kts ($\approx 20 \text{ m/s}$) was recorded. This is probably an upper limit to the range of the wind, and it results in a maximum vertical wind stress term of about 0.09 times the coriolis term. Below the surface mixed layer, the stress gradient and therefore the vertical friction term are much smaller.

4.3. Comparison between ADCP and SeaSoar data

Another way to look at the location and importance of ageostrophic effects is to compare SeaSoar and ADCP velocities. Although absolute velocities cannot be computed from SeaSoar data, geostrophic velocity shear can be computed from density. SeaSoar measurements are assumed to be quite accurate, as discussed in chapter 3. However, vertical displacement of the isopycnal surfaces by high frequency internal waves is a potential source of contamination for the estimate of geostrophic velocity shear. Wave-like vertical displacements are not evident in density sections drawn from the smoothed SeaSoar data (Read *et al.*, 1987), so it seems that smoothing of the SeaSoar data over 12 km (chapter 3) was effective in removing most of the internal wave noise. Therefore, velocity shear calculated from SeaSoar data is considered to be a good estimate of geostrophic shear. Since ADCP velocity represents true flow (ignoring instrument errors), the difference between corresponding ADCP and SeaSoar velocity shears represents the ageostrophic component of the absolute velocity shear.

Geostrophic velocity shear was computed from SeaSoar data in the following manner. Specific volume was computed using the 1980 international equation of state (Unesco, 1981). Specific volume anomaly (α') was integrated over pressure values to obtain geopotential anomaly (Φ') at each level. Then the geopotential anomalies at 22 db and at 46 db, referenced to 150 db, were calculated along each track:

$$d\Phi' = g dz = -\alpha' dp \quad (4.1)$$

$$\Phi_1' - \Phi_2' = \int_{z_1}^{z_2} \alpha' dp \quad (4.2)$$

Velocity shear was then computed from the gradient of geopotential anomaly along the track; from equations (2.5) and (2.6):

$$u = -\frac{1}{f} \left[\frac{\partial \Phi'}{\partial y} \right] \quad (4.3)$$

$$u_1 - u_2 = -\frac{1}{f} \left[\frac{\partial(\Phi_1' - \Phi_2')}{\partial y} \right] \quad (4.4)$$

Due to the offset in grids between the two data sets, and the difference between pressure and depth coordinates, the ADCP and SeaSoar shears are vertically offset from each other by about 3 meters. The ADCP 24-152 m and SeaSoar 22-150 db data will be referred to as 25-150 m shears. Likewise, 50-150 m shears will refer to those calculated from 48-152 m ADCP and 46-150 db SeaSoar data. These differences are negligible for practical purposes.

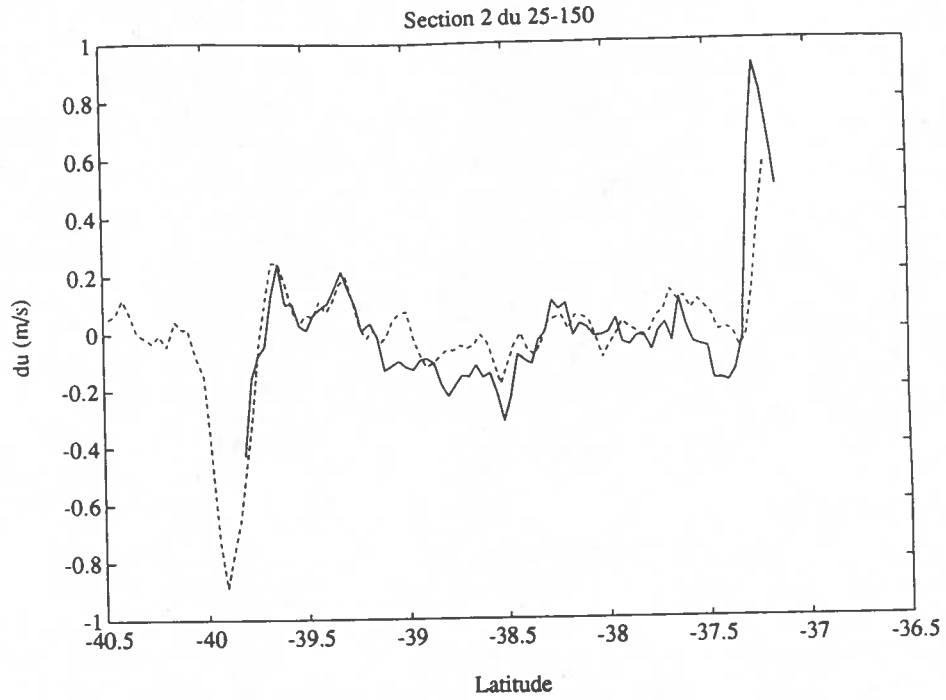
Some of the errors in ADCP absolute velocity measurements discussed in appendix B are absent in shear measurements. The position errors and loss of resolution of ADCP velocity resulting from smoothing navigation data do not apply to shear measurements because navigation is not required to obtain velocity shear. The ADCP shear was horizontally averaged over roughly 4 km along-track sections for comparison with SeaSoar shear. Misalignment of the transducer or gyro is constant within the same profile, minimizing errors due to misalignment. Error due to surface wave-induced variability should also be negligible in velocity shear above 150 m. ADCP measurement error is estimated to be well below 5 cm/s for velocity shear. Therefore, the difference between ADCP and SeaSoar velocity shears is considered to be a fairly accurate measure of ageostrophic signal on a scale of about 12 km, the averaging interval for the SeaSoar data.

The 25-150 m and 50-150 m shear velocity was computed for both data sets and plotted for all of the tracks shown in Fig. 2. Velocity shears for tracks 2, 3, 4 and 5 are shown in Figs. 6a-6d. These are the tracks of most interest because Geosat, ADCP and SeaSoar data are all available for

them (except SeaSoar is not available for the southern half of track 4). The ADCP and SeaSoar velocity shears agree quite well in most places, showing similar features on surprisingly small scales. In spite of the overall agreement, there are also portions with significant differences. Strong ageostrophic flow is inferred wherever the difference is large compared to the size of the geostrophic shear shown by the SeaSoar plot. This difference will be discussed in detail in chapter 5.

4.4. Summary on ageostrophic scaling

The overall balance of terms in the momentum equation indicates that the magnitude of ageostrophic effects is relatively small. As shown in table 2, the magnitude of all individual non-linear and friction terms is 5% or less of that of the Coriolis term. A combined rms estimate of the ageostrophic effects is less than 7%. These estimates agree with the estimated divergent flow around loops of connecting ship tracks of 10% or less. Although ADCP and SeaSoar data agree well overall, there are sometimes fairly large differences, possibly suggesting strong small-scale ageostrophic flow at these points.



(a)

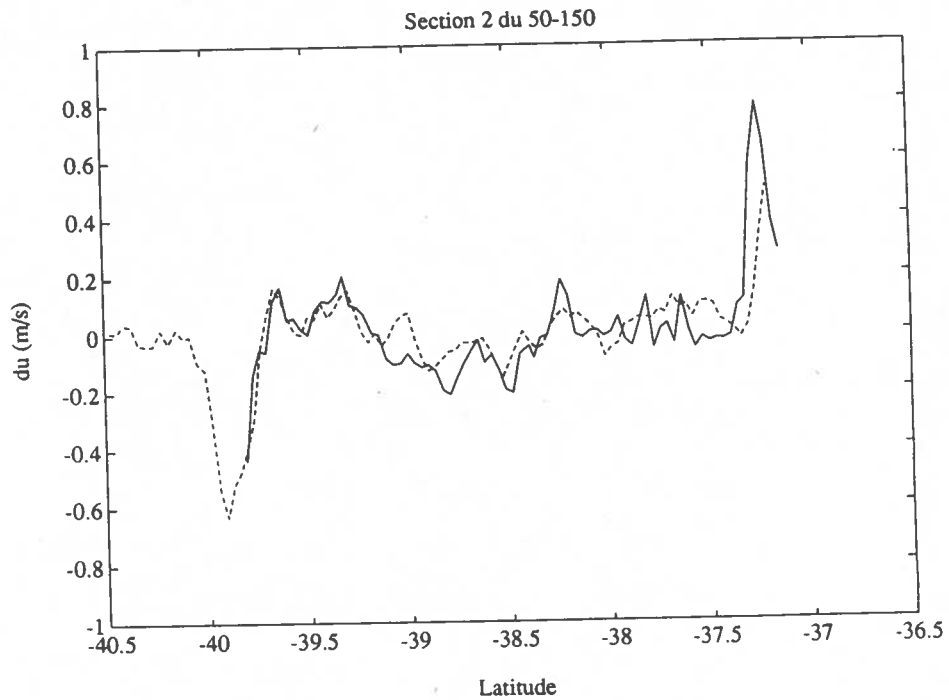
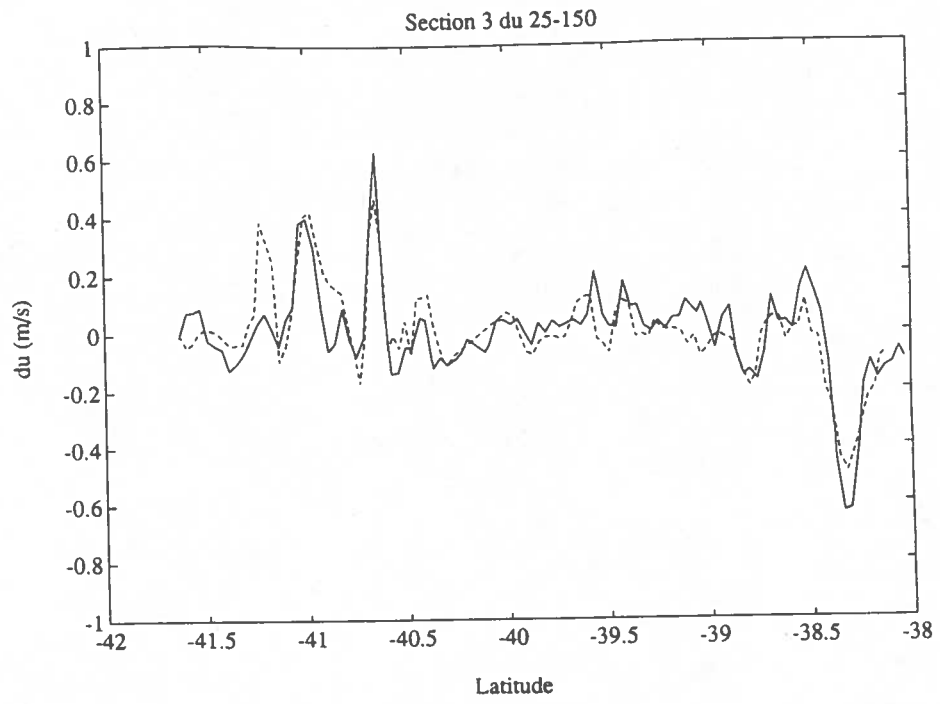
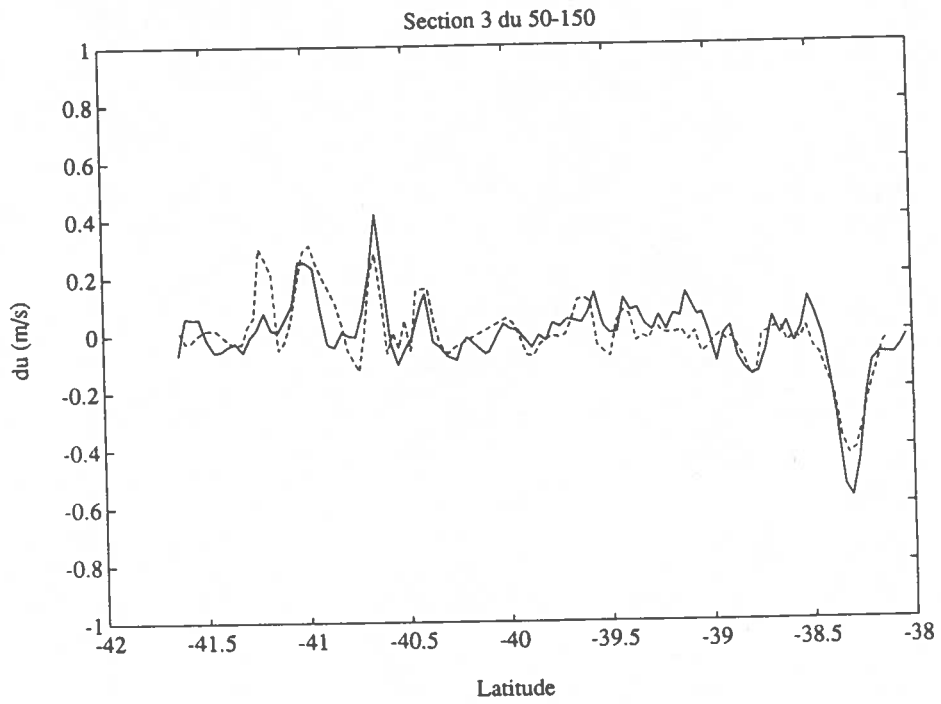
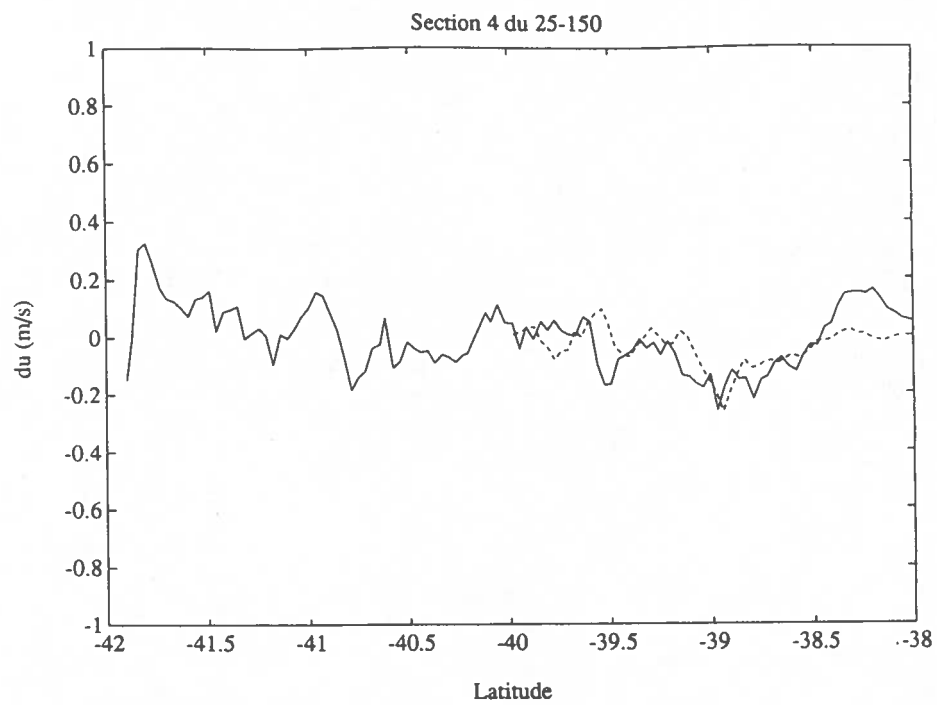


Fig. 6. Velocity Shears between 25 and 150 meters and between 50 and 150 meters for (a) section 2, (b) section 3, (c) section 4 and (d) section 5. Solid lines represent velocity shears measured by ADCP. Dotted lines represent geostrophic velocity computed from SeaSoar densities.

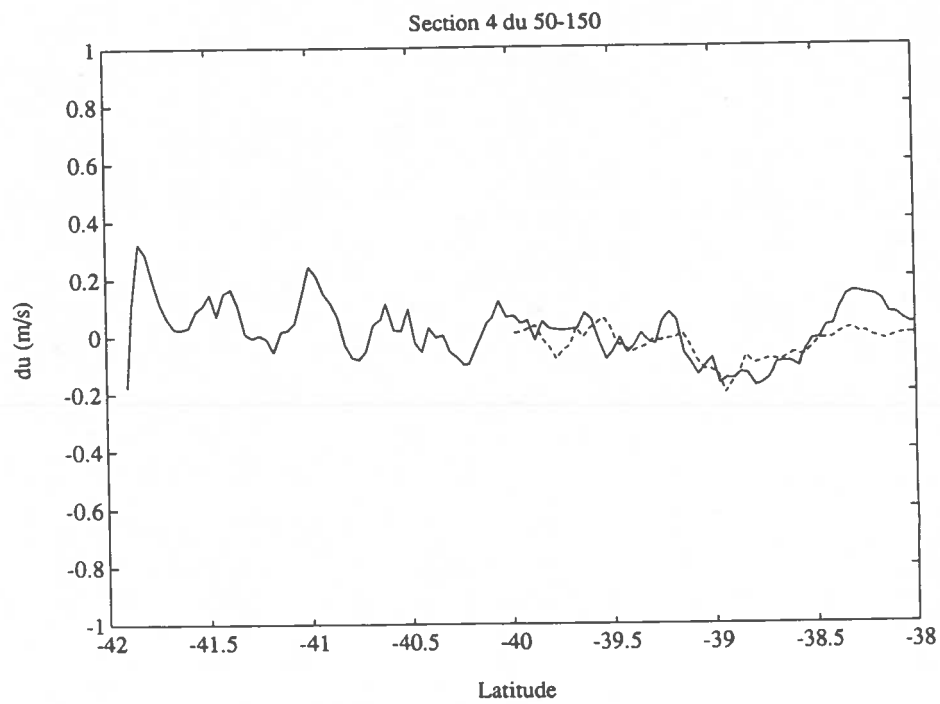


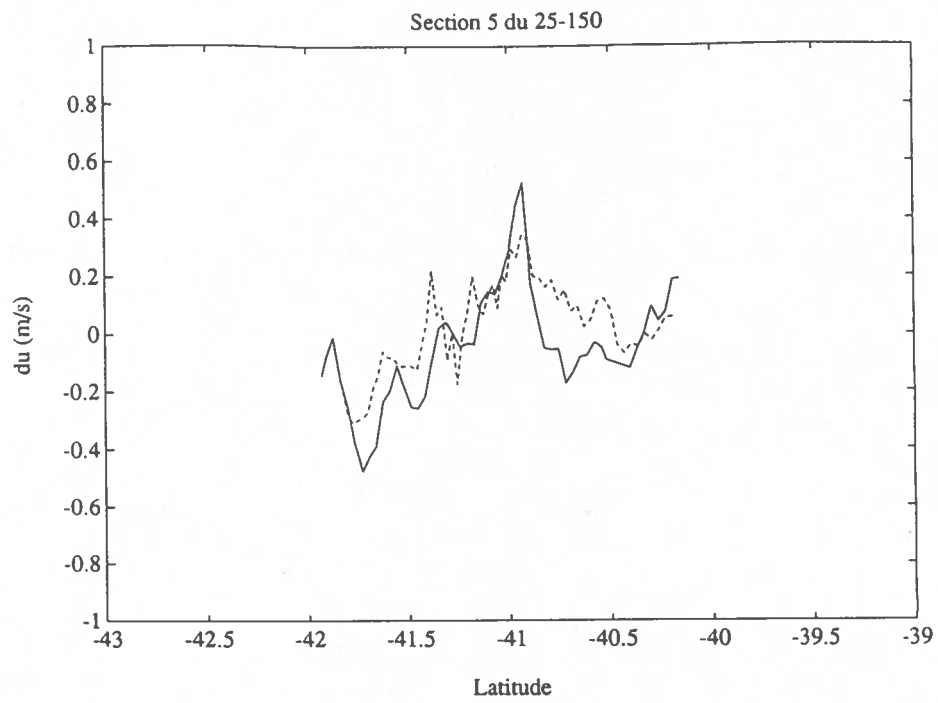
(b)





(c)





(d)

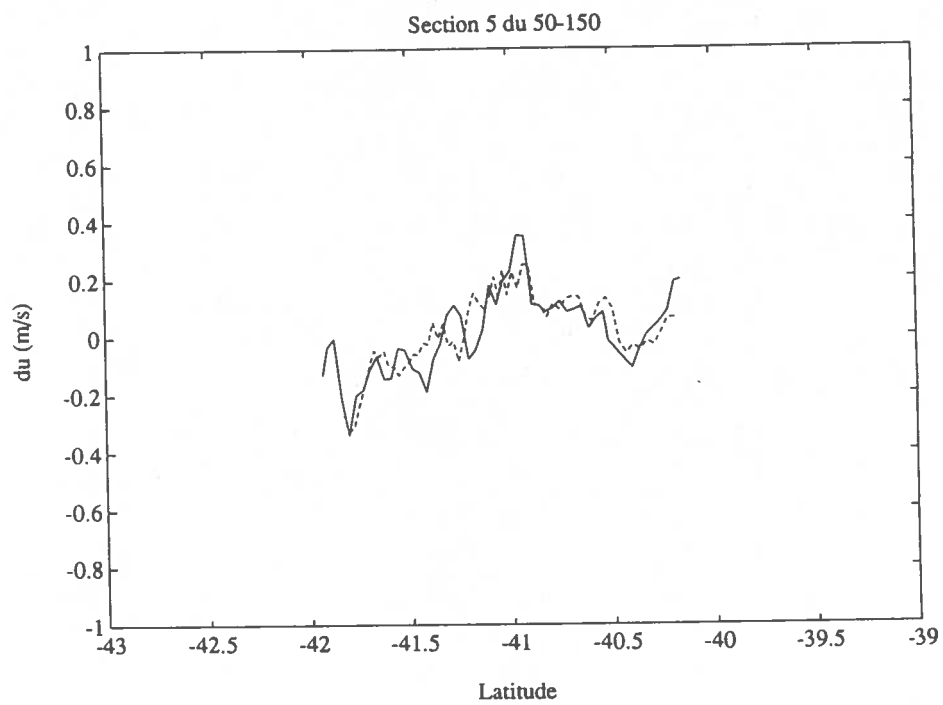


Table 2

Estimated magnitude of terms in the momentum equation

Term	Magnitude (m/s^2)	Relative to fu
$\frac{\partial v}{\partial t}$	6.3×10^{-7}	0.01
$u \frac{\partial v}{\partial x}$	4.3×10^{-6}	0.05
$v \frac{\partial v}{\partial y}$	3.2×10^{-6}	0.03
$w \frac{\partial v}{\partial z}$	2.8×10^{-13} *	10^{-9} *
fu	9.4×10^{-5}	1
$-\alpha \frac{\partial p}{\partial y}$	**	1
$A_H \frac{\partial^2 v}{\partial x^2}$	1.6×10^{-6}	0.02
$A_H \frac{\partial^2 v}{\partial y^2}$	1.6×10^{-6}	0.02
$A_Z \frac{\partial^2 v}{\partial z^2}$	1.4×10^{-6}	0.015

*This term becomes 0 at the surface

**No specific estimate from data, see text

CHAPTER 5

DISCUSSION OF AGEOSTROPHIC EFFECTS

The magnitudes of terms in the momentum equation imply that the geostrophic assumption is accurate within 7 percent. However, ADCP and SeaSoar data compared in chapter 4 indicate intermittently stronger ageostrophic effects. We will now investigate the various types of ageostrophic motion reflected in the measurements and try to clarify the impact these motions have on the computed absolute sea level.

5.1. Cyclostrophy

One form of advection in the Agulhas retroflection is cyclostrophy. Cyclostrophic flow is a balance between centrifugal force and pressure gradient force (Neumann and Pierson, 1966). When circular motion of the current causes centrifugal force to be significant relative to coriolis force in the equation of motion, both terms must be considered. If we neglect friction terms and assume we are at the surface, the momentum equation (2.4) can be expressed in vector form as follows:

$$\frac{d\vec{U}}{dt} + f\hat{k} \times \vec{U} = -g \nabla h \quad (5.1)$$

The gradient current relation, representing a balance between pressure gradient, coriolis and centrifugal forces, can then be derived in natural coordinates in the following manner. Let \vec{U} represent velocity of a fluid particle along a streamline with magnitude U and direction defined by unit vector \hat{t} . $\hat{\nu}$ is defined as $\hat{k} \times \hat{t}$ where \hat{k} is in the vertical direction. s and n are the coordinates measuring distance in the \hat{t} and $\hat{\nu}$ directions, respectively. Therefore,

$$U = \frac{ds}{dt} \quad (5.2)$$

Since only s varies in time along a streamline,

$$\frac{d\vec{U}}{dt} = \frac{d\vec{U}}{ds} \frac{ds}{dt} = \left[\frac{\partial U}{\partial s} \hat{t} + U \frac{\partial \hat{t}}{\partial s} \right] \frac{ds}{dt} \quad (5.3)$$

Using the definition of U and substituting this value of $\frac{d\vec{U}}{dt}$ into the horizontal momentum equation gives:

$$\left[\frac{\partial U}{\partial s} \hat{t} + U \frac{\partial \hat{t}}{\partial s} \right] U + f\hat{k} \times \vec{U} = -g \nabla h \quad (5.4)$$

This equation leads to the following component equations in the \hat{t} and \hat{v} directions.

$$\frac{\partial U}{\partial s} U = -g \frac{\partial h}{\partial s} \quad (5.5)$$

$$U^2 \frac{\partial \hat{t}}{\partial s} + fU = -g \frac{\partial h}{\partial n} \quad (5.6)$$

As shown in Fig. 7,

$$\frac{\partial \hat{t}}{\partial s} = \kappa \hat{v} \quad (5.7)$$

The reciprocal of κ is R , the radius of curvature. Substituting this into the \hat{v} component equation above gives the gradient current relation in its usual form.

$$\frac{U^2}{R} + fU = -g \frac{\partial h}{\partial n} \quad (5.8)$$

Note that the gradient current relation can also be written

$$\left[\frac{U}{fR} + 1 \right] fU = -g \frac{\partial h}{\partial n} \quad (5.9)$$

where $\frac{U}{fR}$ (the Rossby number) represents the ratio of the nonlinear, centrifugal acceleration to the Coriolis acceleration.

ADCP-measured current velocities and estimated radii of curvature based on NOAA-9 satellite thermal infrared images were used to estimate the contribution of cyclostrophic flow to the motion in this region. Twenty individual images and three composite images taken from February through October 1985 (Luyten *et al.*, 1990) were used to estimate the average radius of curvature in various sections of the Agulhas. The composite images were formed by selecting the warmest temperature for a period of about one week for each 4.4 km pixel. The large turn or retroflexion had a fairly consistent radius of about 130 km. The other, less consistent meanders had an average radius of about 85 km, with sizes ranging from 55 to 150 km. Applying estimated radii and typical ADCP-measured current speeds for each area gives Rossby numbers of 0.082 and 0.109 for the main retroflexion and other meander areas, respectively. If maximum ADCP-measured current speeds are used, the Rossby number increases to 0.144 in the main retroflexion turn, with slightly smaller values in the other meanders. Thus, cyclostrophy would be expected to contribute an 8-14% error in a geostrophic computation of absolute sea level from ADCP velocities in current meanders.

It is possible that centrifugal force accounts for most of the apparent ageostrophic motion in the region. If so, one would expect the sum of the horizontal advection terms from chapter 4 to be

greater than other non-geostrophic terms and comparable to estimated cyclostrophic motion (since derivation of the gradient current relation includes both horizontal advection terms). The sum of the horizontal advection terms is about 0.08 times the Coriolis term. This is larger than the other non-geostrophic terms and is close to the value of $\frac{U}{fR}$ computed for the main retroflection area. The difference between SeaSoar and ADCP velocity shears discussed in chapter 4 represents ageostrophic motion on a scale of approximately 12 km. If this ageostrophic motion is mostly cyclostrophic, its magnitude should generally correspond with the radii of curvature and direction of meandering visible in AVHRR images of the region.

The radius of curvature corresponding to ADCP/SeaSoar shear differences can be calculated from the gradient current and geostrophic equations in the following manner. If the ship track is parallel to \hat{v} , the cross-track ADCP velocity shear can be described by the vertical derivative of the gradient current relation.

$$\left[f + 2 \frac{U}{R} \right] \frac{\partial U}{\partial z} = -g \frac{\partial}{\partial z} \left[\frac{\partial h}{\partial n} \right] \quad (5.10)$$

Seasoar velocity shear can be described by the vertical derivative of the geostrophic balance.

$$f \hat{k} \times \frac{\partial \vec{U}}{\partial z} = -g \frac{\partial}{\partial z} \nabla h \quad (5.11)$$

If the ship track is parallel to \hat{v} , the cross-track velocity shear computed from Seasoar data will be described by:

$$f \frac{\partial U}{\partial z} = -g \frac{\partial}{\partial z} \left[\frac{\partial h}{\partial n} \right] \quad (5.12)$$

Subtracting the Seasoar velocity equation from the ADCP velocity equation results in a relationship which can be used to solve for R .

$$f \left[\frac{\partial U_{adcp}}{\partial z} - \frac{\partial U_{seasoar}}{\partial z} \right] + 2 \frac{U}{R} \frac{\partial U_{adcp}}{\partial z} = 0 \quad (5.13)$$

If the ship track is offset from \hat{v} by θ degrees, the radius of curvature calculated in this manner would be multiplied by a factor of $\cos \theta$.

Computation of R from 50-150 m ADCP and SeaSoar velocity shears as described above yielded unrealistic values. The same calculation using 25-150 m velocity shears would produce even worse results, as they do not agree as well as the 50-150 m velocity shears do (see Figs. 6a-6d). In cases where the ship track appeared to be close to \hat{v} in Agulhas AVHRR images, R seemed to be the

correct sign to correspond to visible curves in the Agulhas, but the magnitude of R was on the order of 1-5 km rather than 50-100 km as was expected. Many variations in the computed R were unexplainable based on the visual images available. The small values of computed R indicate a larger difference between ADCP and SeaSoar velocities than can be accounted for by cyclostrophy. Therefore, some other type of ageostrophic motion must be important on the 12 km scale reflected by the ADCP and SeaSoar velocity shear comparison.

5.2. Ekman flow

Ekman flow results from a balance between Coriolis force and the vertical derivative of friction or stress on the ocean's surface caused by the wind. Neglecting all other terms in the momentum equation (eqn 2.4) results in the Ekman balance:

$$fu = A_z \frac{\partial^2 v}{\partial z^2} = \frac{\tau_y}{\rho a} \quad (5.14)$$

where the vertical friction term is also expressed in terms of wind stress (τ) and mixed layer depth (a) as discussed in chapter 4. It is difficult to accurately detect Ekman flow with current measurements, so the velocity is estimated from the wind stress. The vertical friction term computed in chapter 4 from average wind stress is about one percent of the Coriolis term. The corresponding Ekman velocity is only 1.5 cm/s. The maximum wind stress of 20 m/s recorded onboard the RRS Discovery could generate an Ekman current of about 10 cm/s if it were sustained long enough, but a period of a few days is required to produce the steady-state situation in which the Ekman current would reach this magnitude (Pond and Pickard, 1983). Therefore, the average wind stress is more representative of the actual Ekman currents.

5.3. Internal waves

Internal waves are caused by the oscillation of water particles in response to some combination of rotation and buoyancy. The time variation of velocity due to internal waves is on a much shorter scale than that considered in the large scale momentum equation (eqn 2.4). However, internal waves are present throughout the ocean, and the measurements taken during the Agulhas cruise may well be affected by internal wave noise. High frequency internal waves are governed mostly by buoyancy, resulting in primarily vertical motion. This type of motion would not be expected to affect horizontal ADCP velocity measurements significantly. As mentioned in chapter 4, vertical displacement of the smoothed SeaSoar measurements due to internal waves seems to be minimal. Low frequency or "near-inertial" internal waves are governed more by rotation, resulting in primarily horizontal motion. This type of motion would not be expected to be reflected in SeaSoar measurements, but

would manifest itself as ageostrophic velocity in ADCP measurements.

Near-inertial internal waves, also referred to as inertial motions, are often generated by winds at the ocean's surface (Pollard, 1970). Inertial motion is sustained by a balance between acceleration in the frame of reference and Coriolis force.

$$\frac{d\vec{V}}{dt} + \vec{f} \times \vec{V} = 0 \quad (5.15)$$

Although Ekman currents generated from steady winds in the Agulhas region are estimated to be small ($\sim 1\text{-}2$ cm/s), inertial motions are likely to be greater. Whereas Ekman flow develops with steady wind blowing for a period of days, inertial motions can be generated with short bursts of wind. Pollard (1970) points out that changes in the wind field with time scales less than one inertial period (17.5 hours, in this case) have the most influence on inertial oscillations. These short term changes in the wind field can generate or destroy inertial oscillations, depending on the direction of the wind and current vectors (Pollard and Millard, 1970). Therefore, estimates for ageostrophic velocity due to inertial motion would range from zero to a velocity corresponding to the maximum wind stress experienced. As previously mentioned, the current generated by the maximum wind stress recorded during the RRS Discovery cruise is about 10 cm/s.

Inertial motions are often displayed in stick diagrams like those of Figs. 8a-8d. These figures show the direction and magnitude of ADCP-measured velocity with the vertical mean removed. Ideally, inertial oscillations would show up in plots like these as vectors which rotate smoothly in one direction with depth or along track, reflecting the circling nature of the motion. The measurements were taken from a moving ship, however, and without knowledge of the horizontal structure of the waves, it is unclear how the temporal and spatial change in the measuring platform affects the appearance of inertial oscillations in the plots. There are several examples in Figs. 8a-8d where a steady rotation of the vectors is evident, indicating the presence of at least some inertial motion. The magnitude of the rotating vectors is about 10 cm/s.

If inertial motions were responsible for much of the ageostrophic velocity implied by Figs. 6a-6d, their effects would probably be greatly reduced in the along-track integration to calculate sea level. D'Asaro and Perkins (1984) produced internal wave frequency spectra indicating that the peak energy of near-inertial internal waves occurs at horizontal wavelengths of approximately 25-75 km. The inertial motions apparent in Figs. 6a-6d seem to have wavelengths of about 55 km. Ship tracks 2 through 5 (depicted in Fig. 2) are 200 km or more in length. If the direction of motion changes on small scales relative to the length of the track, most inertial motion will probably cancel itself out when integrated over the ship track to obtain sea level.

5.4. Depth dependence of ageostrophic effects

Ageostrophic effects seem to decline with depth in this particular data set. This trend is most visible in plots of ADCP and SeaSoar geopotential difference (Figs. 9a-9d). 25-150 m and 50-150 m geopotential differences were calculated from SeaSoar data as described in chapter 3. The corresponding differences were computed from ADCP data by integrating the velocity shear along track and multiplying by $-f$. From equation (4.4),

$$-f \int_A^B (u_1 - u_2) dy + (u_1 - u_2)_A = \Phi_1 - \Phi_2 \quad (5.16)$$

As for velocity shear discussed in chapter 4, the difference between ADCP and SeaSoar plots approximates the ageostrophic component of geopotential anomaly on a scale of about 12 km. In most places, this difference is smaller for 50-150 m anomalies than for 25-150 m anomalies, indicating less ageostrophic flow at 50 m than at 25 m. Such a trend could be attributed to several factors. Ekman flow and inertial oscillations may be decaying away from the generating force of the wind. Gusts of 15-20 m/s were recorded in the ship's log along track 5, where a large discrepancy between the 25-150 m and 50-150 m plots exists. Also, slightly slower current velocity at depth would result in smaller cyclostrophic flow ($\frac{U^2}{R}$). In some places, the difference between ageostrophic flow at 25 m and at 50 m seems quite large (especially on track 5). Will large errors be reflected in the sea surface height computed from ADCP "surface" velocities (~ 25 m) as a result of this apparently large ageostrophic flow near the surface?

Two different methods were used to compute absolute sea level from the available data in an attempt to address this question. First, the height was computed using near-surface ADCP velocity in equation (2.9). Second, the ADCP velocity at approximately 150 m was combined with the change in geopotential from 150 m to the surface (from SeaSoar density) to obtain the height. Using equation (4.2), geopotential at pressure surface i (150 m, in this case) can be defined:

$$\Phi_i = \int_{p_0}^{p_i} -\alpha(p) dp + \Phi_0 \quad (5.17)$$

where p_0 and Φ_0 represent the pressure and geopotential at a reference level (at the surface, in this case). Geostrophy implies that (from equations (2.5) and (2.6)):

$$fu = -\frac{\partial \Phi}{\partial y} \quad (5.18)$$

Using equation (2.7) in equations (5.17) and (5.18),

$$fu = -\frac{\partial}{\partial y} \left[\int_{p_0}^{p_i} -\alpha(p) dp + gh \right] \quad (5.19)$$

$$h = \frac{1}{g} \left[\int_{p_0}^{p_i} \alpha(p) dp - \int_A^B fu \partial y - h_A \right] \quad (5.20)$$

Because of the apparent decrease in ageostrophic motion with depth in this data, the second method of sea level calculation is probably more accurate. The difference between the two methods could be interpreted as a reduction in ageostrophic effects on sea level between 25 m and 150 m.

Absolute sea level, calculated in both ways for tracks 2-5, is shown in Figs. 10a-10d. The maximum difference between sea level calculated with the two methods is about 13 cm (on track 3), with most differences well under 10 cm. This represents less than 10% of the sea level change across the current in contrast to the difference between 25 m and 50 m ageostrophic signals implied by Figs. 9a-9d, which are sometimes 50-100% of the overall geopotential anomaly signal. This result may indicate that some of the large ageostrophic signals apparent in Figs. 9a-9d are due to inertial motions which are averaged out in the integration process to obtain absolute sea level along the track.

5.5. Conclusion on ageostrophic effects

Although we cannot conclude the exact proportion of each type of ageostrophic motion, the two largest seem to be cyclostrophy and inertial oscillation. If horizontal advection terms are assumed to be largely cyclostrophic, they could be considered jointly in the assessment of the momentum equation. Combining the horizontal advection terms, the rms value of ageostrophic terms in the momentum equation is 8.5% of the Coriolis term. Inertial oscillations occur on a smaller time scale than that addressed in the large scale momentum equation. However, the magnitude of velocity generated by these oscillations is estimated to be only around 10 cm/s and a large portion of their effects will probably average out in the calculation of absolute sea level. Therefore, the total ageostrophic effect on calculated sea level is estimated to be less than 9%.

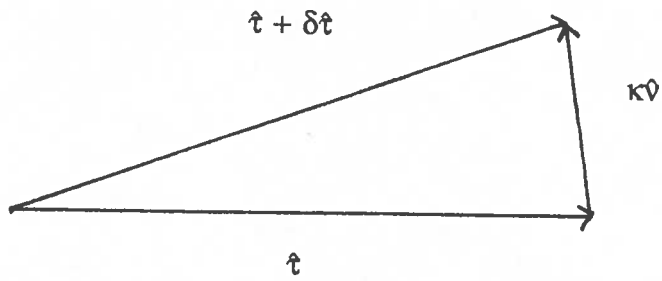


Fig. 7. Diagram showing unit vectors in natural coordinates.

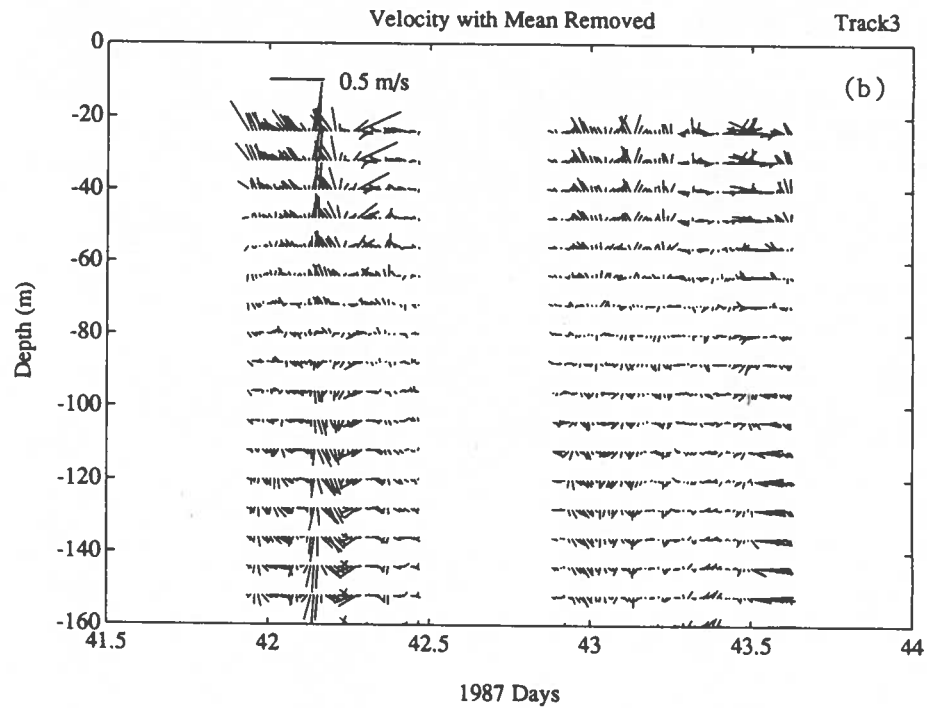
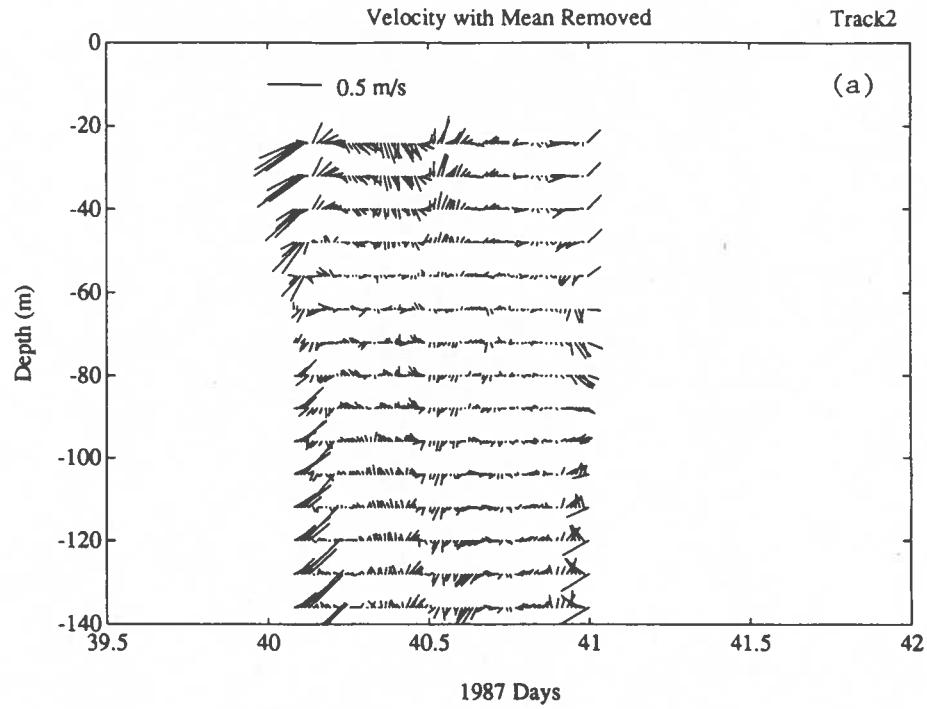
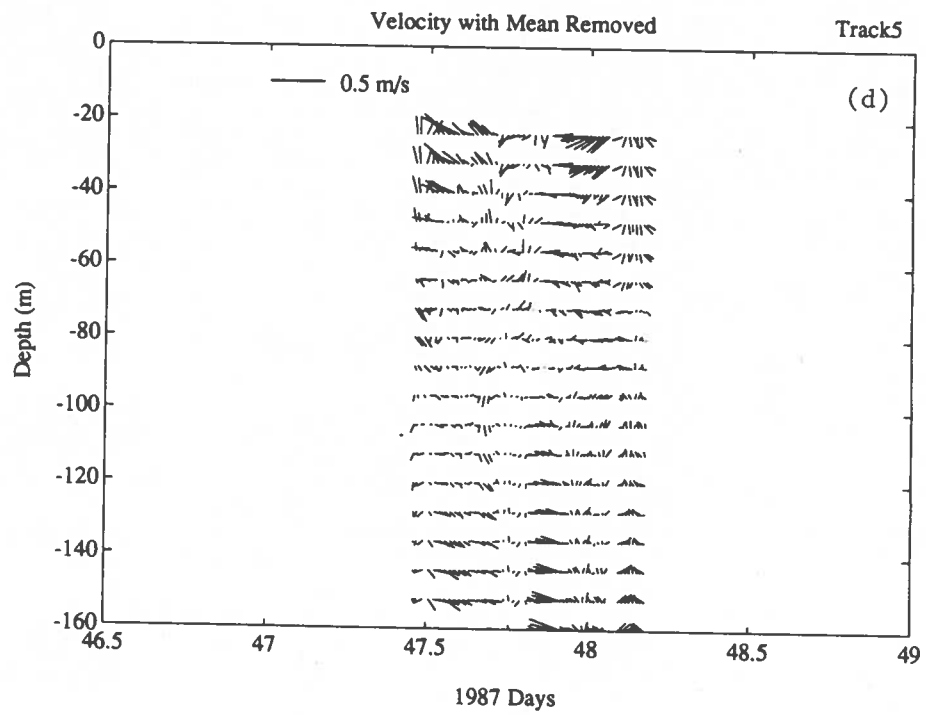
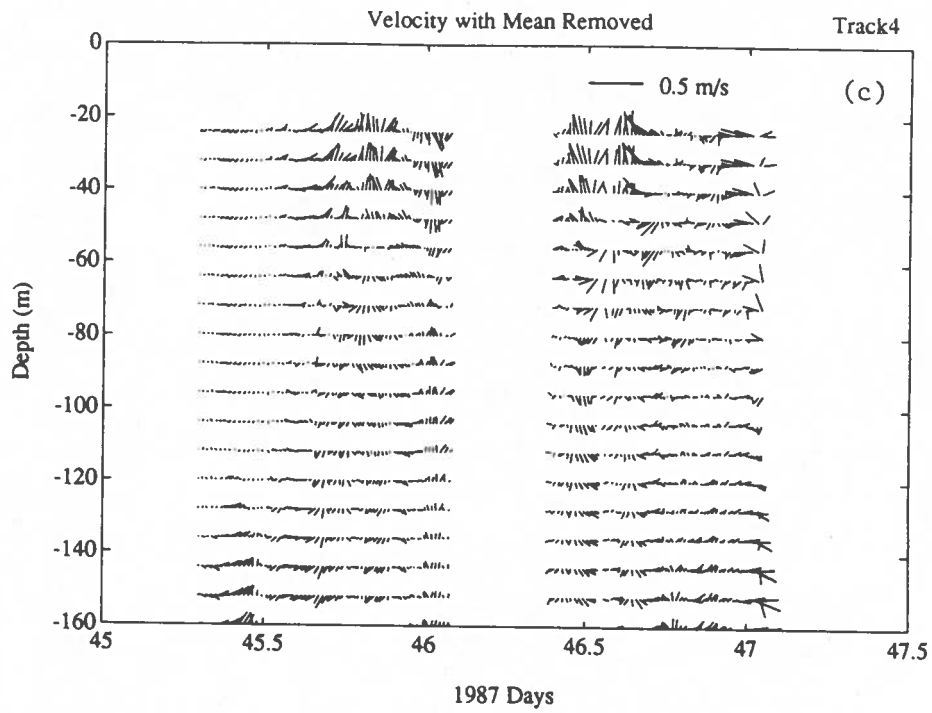
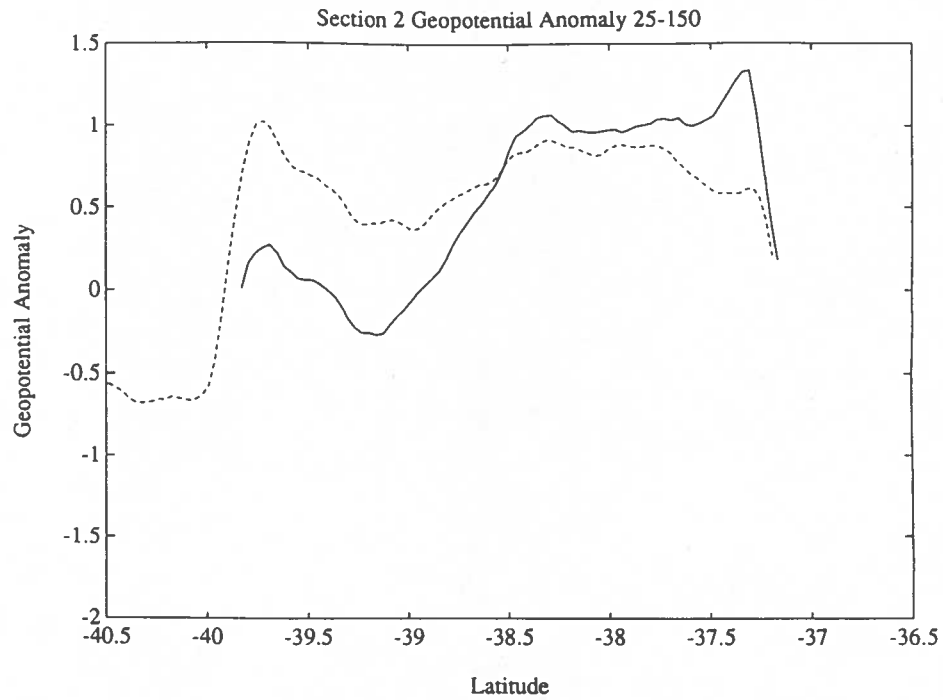


Fig. 8. Residual velocities along (a) track 2, (b) track 3, (c) track 4 and (d) track 5 after removing the vertical mean. Northward velocity vectors point upward. Constant rotation with depth or along track probably reflects inertial oscillation.





(a)

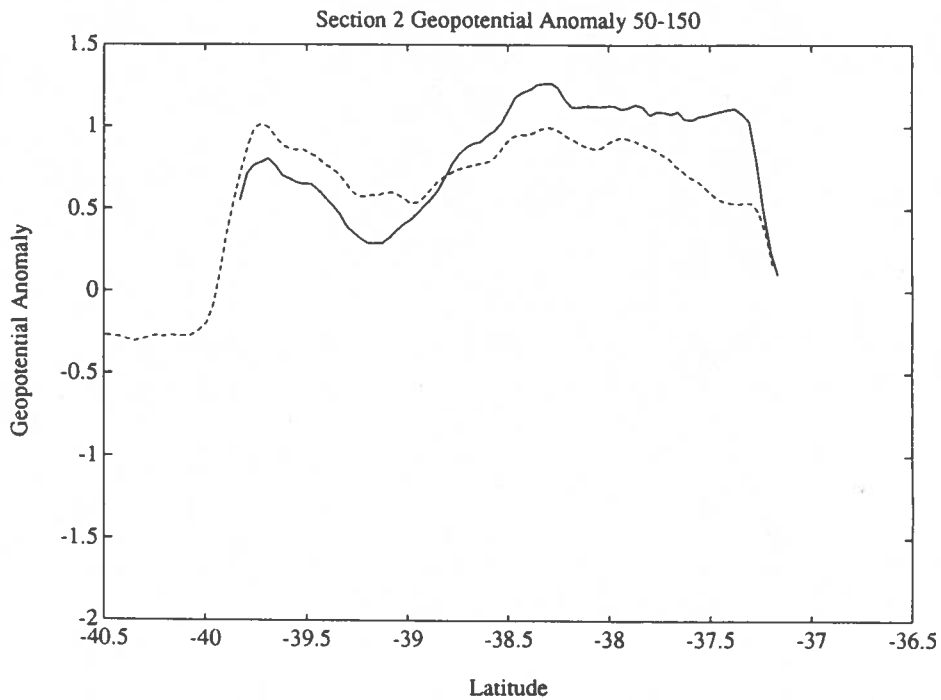
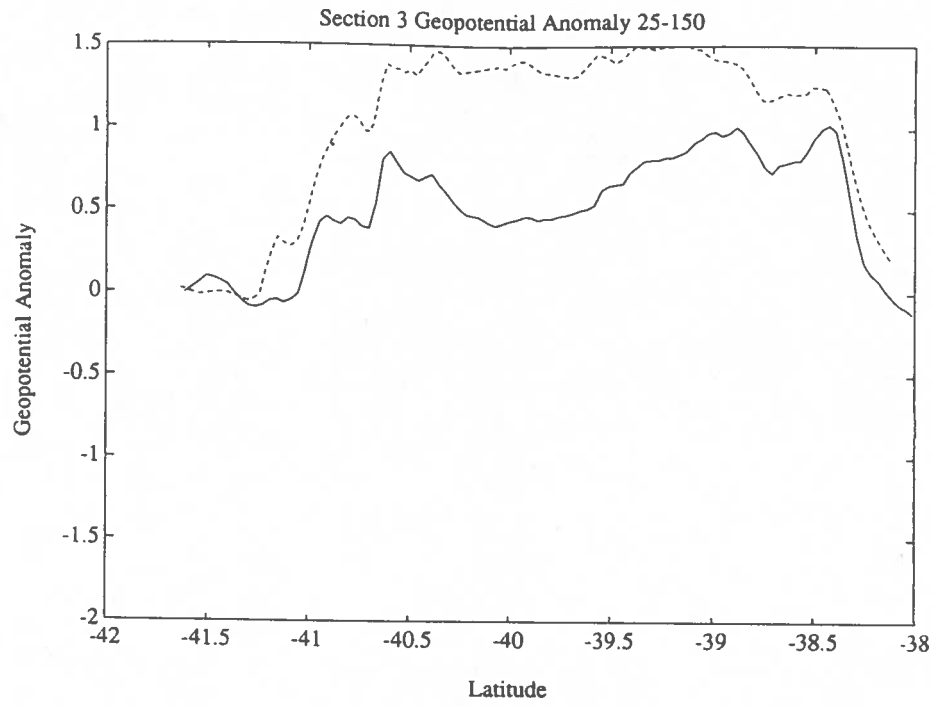
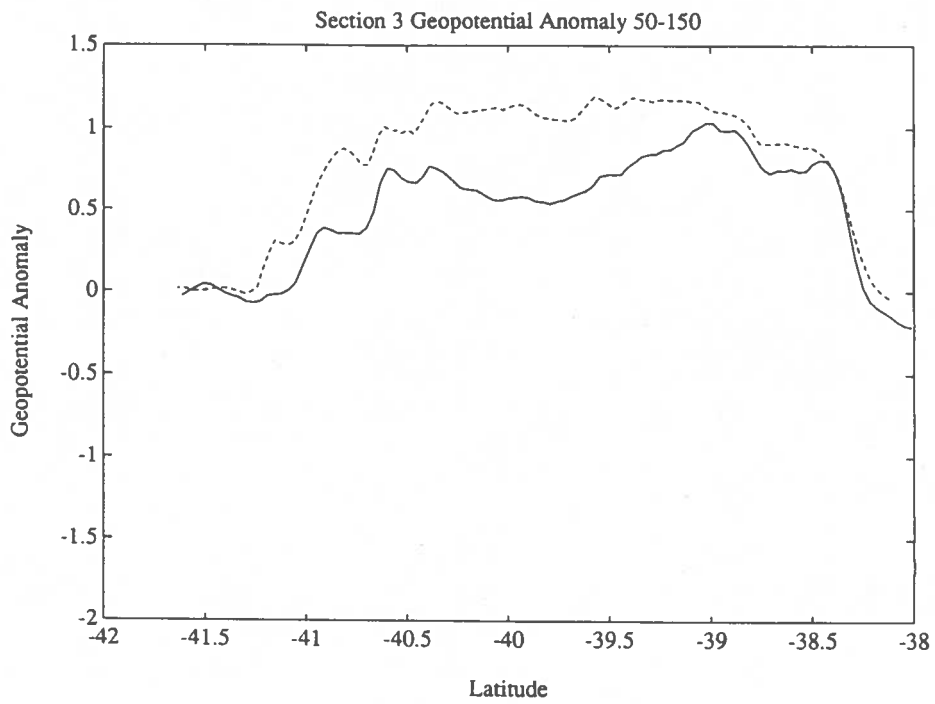
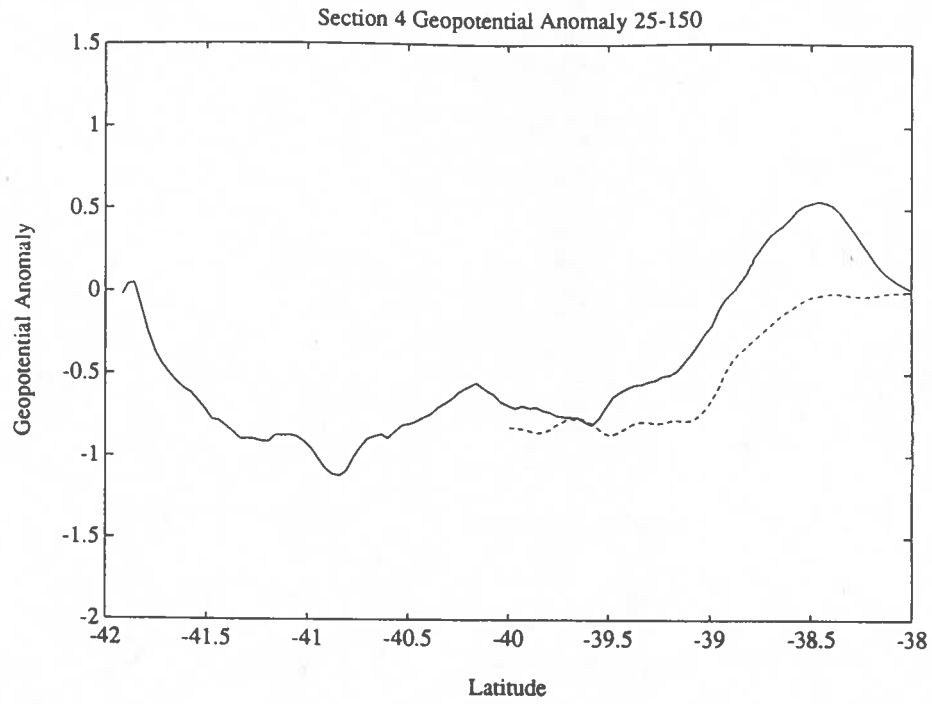


Fig. 9. Geopotential Anomaly in m^2s^{-2} between 25 and 150 meters and between 50 and 150 meters along (a) section 2, (b) section 3, (c) section 4 and (d) section 5. Solid lines represent anomalies computed from ADCP velocity shears. Dotted lines represent anomalies computed from SeaSoar densities.

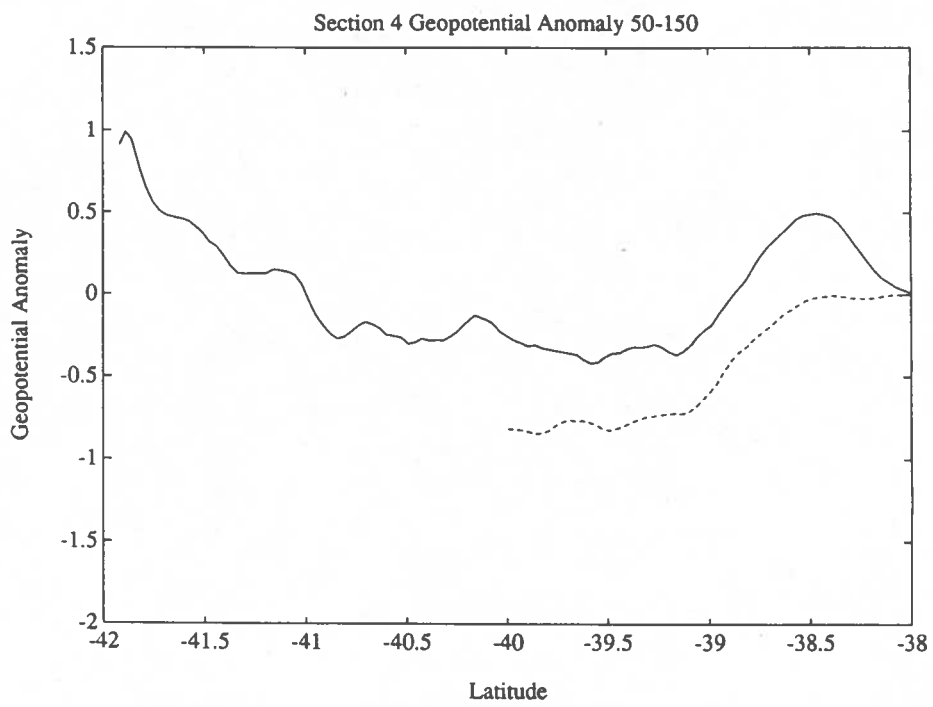


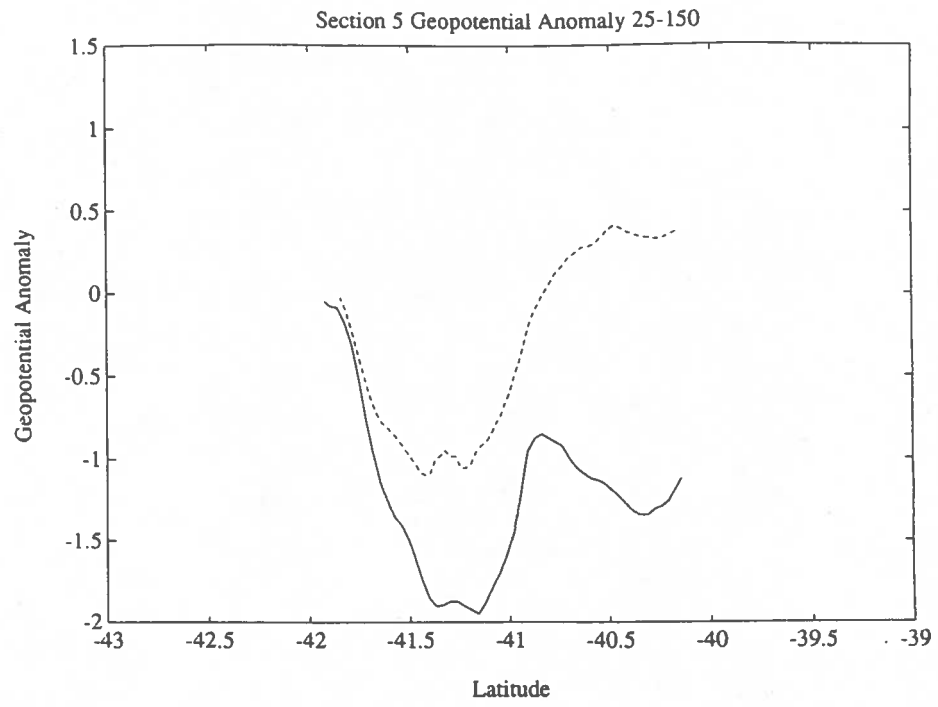
(b)



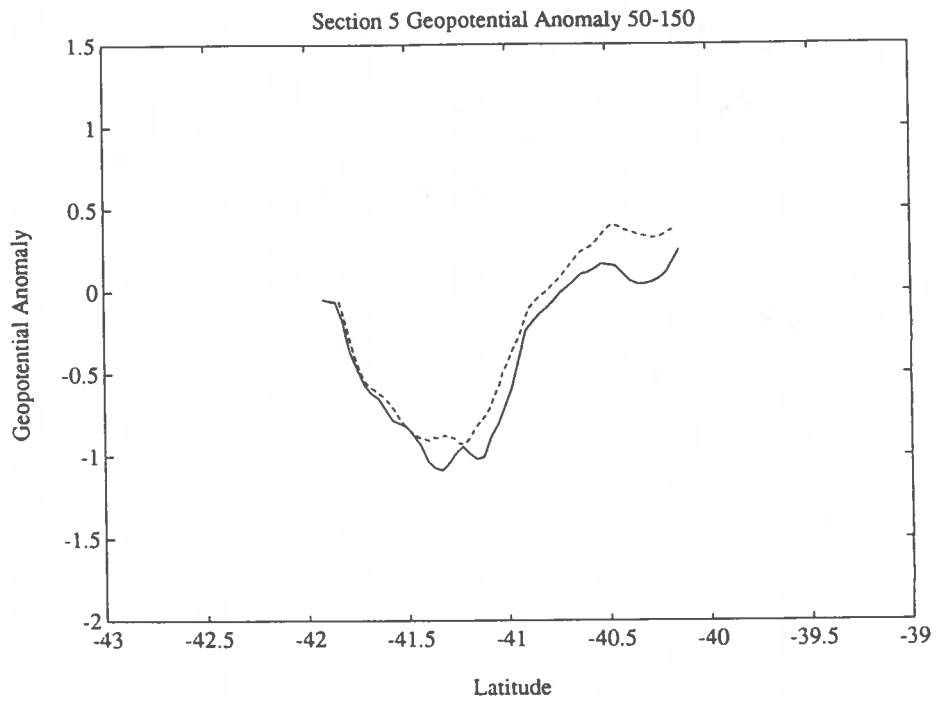


(c)





(d)



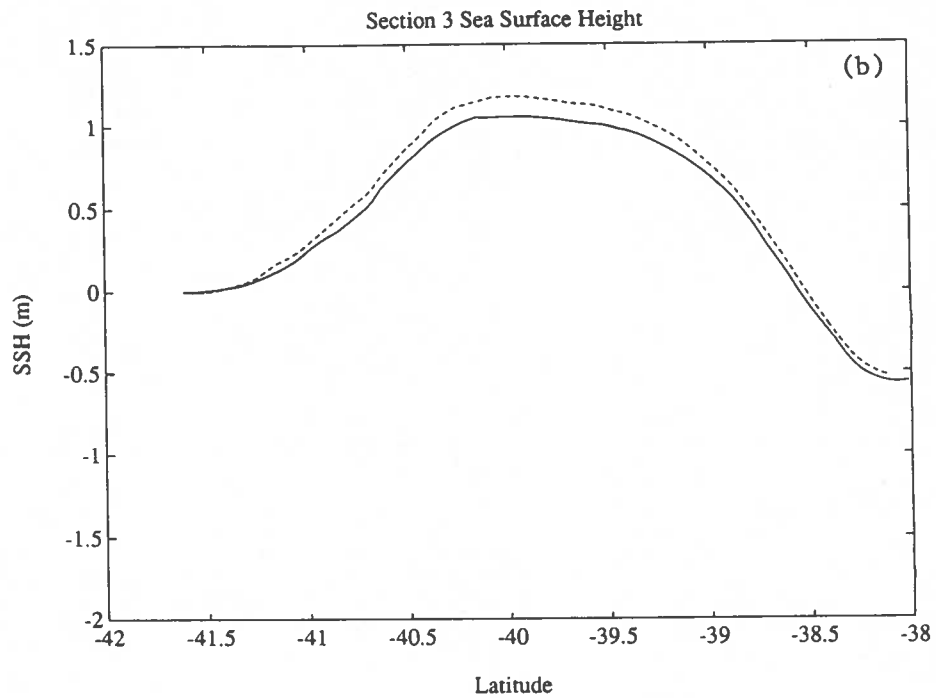
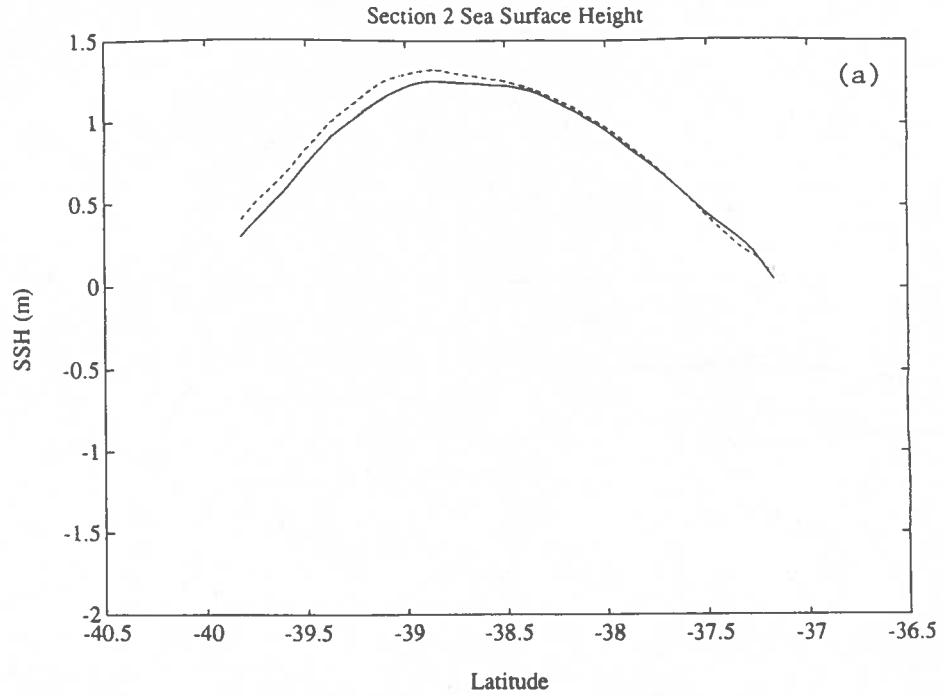
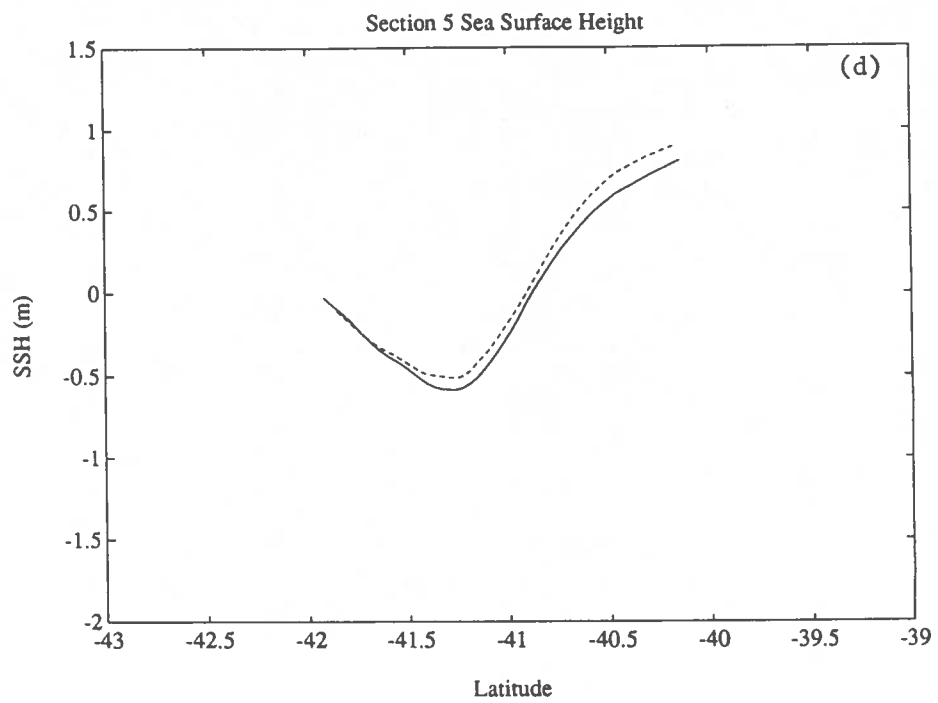
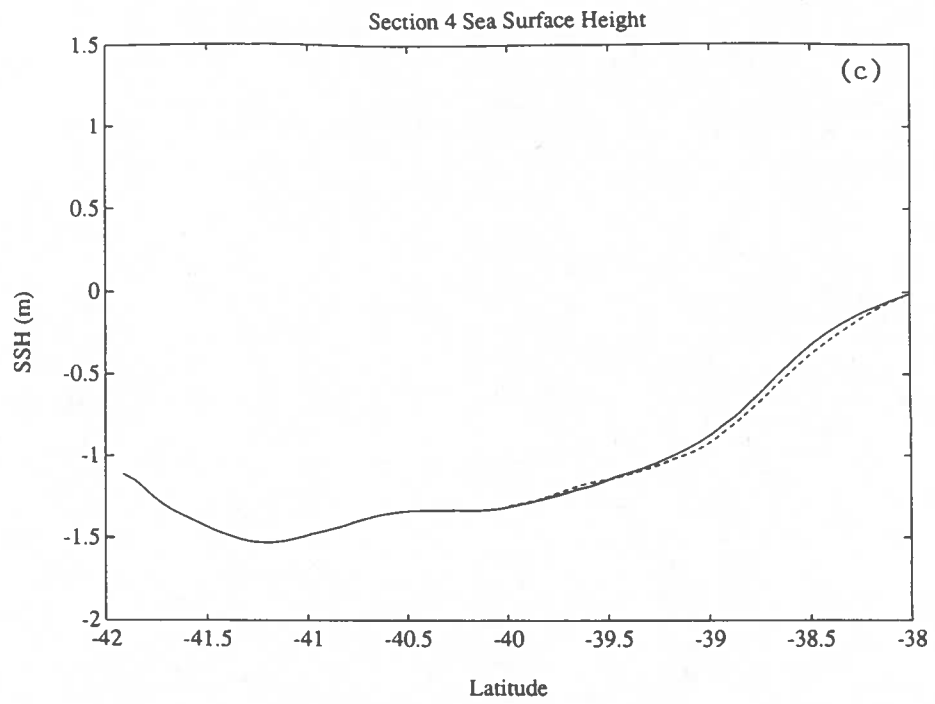


Fig. 10. Sea surface height along (a) section 2, (b) section 3, (c) section 4 and (d) section 5. Solid lines represent heights calculated from near-surface ADCP velocities. Dotted lines represent heights calculated from ADCP velocities at 150 m and geopotential difference from 150 m to the surface from SeaSoar densities.



CHAPTER 6

RESULTS

Evaluation of the ageostrophic effects shows that an absolute sea level for the time of the RRS Discovery cruise can be calculated from the geostrophic balance with errors smaller than 10% of the sea level variations. This absolute sea level is the key to obtaining a mean sea surface height to which GEOSAT relative sea level measurements can be added to produce an absolute flow time series.

6.1. Mean sea surface height

Mean sea surface height, computed by subtracting GEOSAT altimeter measurements ($h'(t_0)$) from absolute sea level ($h(t_0)$), is shown in Figs. 11a-11d. GEOSAT-measured sea level variability is also shown in each figure. Because SeaSoar data is not available for half of track 4, the absolute sea level computed from near-surface velocity (method 1 in previous chapter) was used to obtain mean height along all the tracks. Figure 12 shows the mean height on a map of the tracks to enhance physical interpretation. Mean current flow corresponding to the major surface slopes is shown in the diagram by arrows.

The plots show some important features of the mean height. The slope and amplitude of the mean height are consistent with the expected flow of the Agulhas. The northern portion of sections 2 and 3 cross the current where it flows consistently to the southwest and there are few meanders. This consistency is reflected in a relatively large mean current to the west shown in figure 12. The high variability in these northern portions indicates that the southwesterly current flow is sometimes much stronger than the mean flow. The middle portion of section 3 is nearly flat. This is an area through which the retroflexion passes. Since the position of the retroflexion tends to vary, this flat section in the mean height probably corresponds to an area in which the flow alternates directions on a regular basis and averages out in the mean. Note the high variability depicted across the middle latitudes of section 3 in Fig. 11b. The southern portions of sections 2 and 3 have mean flow to the northeast, which agrees well with the normal direction of the retroflected current. Variability in the southern portion of section 3 is relatively low, indicating a fairly constant return flow there. In contrast, variability is high in the southern portion of section 2, possibly because the return flow does not always extend far enough north to cross section 2. The mean current across section 4 is to the east in the direction of the Antarctic Circumpolar Current. This suggests that the westward flowing

Agulhas normally retroflects to the east of track 4. Harris *et al.* (1978) note that the Agulhas appears to have two modes of retroflexion, one at 14E (which would cross track 4) and one at 20E (which would not). The strongest mean flow is across section 5 to the east. This strong mean flow probably represents a joining of the retroflected Agulhas and the general easterly flow in the direction of the Antarctic Circumpolar Current.

Mean current vectors for February 1985 to February 1987 from 200-m and 750-m moorings (Luyten *et al.*, 1990) are shown on the overlay for Fig. 12. The cross-track component of these vectors generally agrees in direction with velocity derived from mean height, representing the period from November 1986 to November 1987. The magnitude of the cross-track component of mean current meter velocity, however, is much smaller than that of the velocity computed from mean height. The velocity shown in Fig. 12 represents the mid-slope velocity computed from the major sea surface slopes on each track. In some cases, the slope is more gentle at the end of the track, and agrees better with current meter measurements. However, there still seems to be a discrepancy between the two velocity fields. Although the nominal current meter depths are approximately 200 m and 750 m, examination of the time series of pressure from one 200-m instrument indicates that the instrument was often dragged as deep as 1000 m in strong flows. Since velocities decrease with depth, this means that the current meter measurements will be biased toward lower velocities. That the mean current itself changed between the February 1985-1987 period and the November 1986-1987 period is also possible and cannot be excluded.

To estimate the range of error for the calculated mean height, the combined errors of ADCP and GEOSAT measurements and ageostrophic motion must be considered. Based on the available calibration data and divergence estimates around closed loops, a constant misalignment angle in the ADCP transducer or ship's gyro of more than $1/2^\circ$ for a significant distance is unlikely. Therefore, the sea level error which would result from a constant $1/2^\circ$ misalignment over 100 km (7 cm) is considered a conservative estimate of ADCP instrument error in the mean height. As discussed in chapter 3, the estimated error in GEOSAT measurements is 11 cm or less. Finally, the estimated ageostrophic effect on the calculated sea level is 13.5 cm (9% of the average 1.5-m difference across the current). Therefore, the combined rms estimate of error for mean height is about 19 cm. This error represents only 12.5% of the mean difference in sea level across the Agulhas (depicted in Fig. 12), so it should not seriously degrade the accuracy of estimated mean current flow across the sections.

6.2. Time Series of absolute flow in the Agulhas

GEOSAT relative sea level measurements for the period November 1986 to November 1988 were added to the calculated mean heights to obtain a time series of absolute sea level in the Agulhas. The first difference of these heights along the GEOSAT track was then calculated and plotted against time. From equation (2.8),

$$u = -\frac{g}{f} \frac{\partial h}{\partial y} \quad (6.1)$$

So, the change in height along the track is directly proportional to and serves as an index for cross-track velocity. This velocity index time series would have been difficult to collect via conventional ship-board or mooring methods. With the data gathered during one cruise, absolute current flow over those tracks can be obtained for as long as an altimeter operates along the same repeat track. With the absolute flow, one can estimate transports in the Agulhas and distinguish between changes in strength and reversals of flow.

The height difference or velocity index time series for each of the four tracks coinciding with GEOSAT paths is shown in Figs. 13a-13d. Positive (negative) differences indicate flow to the east (west) of the track, with differences of 0.5 being equivalent to velocities of approximately 120 cm/s. Several interesting features are evident in the plots. The two sections with the largest mean signal, sections 2 and 5, have cross-track flow in fairly consistent directions, but with varying strength. Knowledge of such variations may be helpful in comparing the strength of the Agulhas with other factors such as seasonal wind patterns in the Indian Ocean. The peak velocities in these plots seem to occur in cycles with periods of about 50-150 days, agreeing with variability shown by current meter measurements (Luyten *et al.*, 1990). Sections 3 and 4 show significant variation in direction of cross-track velocity as well as in strength. For section 3, since it is in the vicinity of the main retroflection turn, these direction changes seem to reflect the meandering of the retroflection to the north and south of the track. In many places, strong flow is present in opposite directions across the northern and southern portions of track 3, probably representative of the retroflection being centered on the track. The mean flow across all of section 4 to the east is evident in the absolute flow time series. There are many times in the plot where the flow changes direction, however. These are probably indicative of times when the westward flowing Agulhas current reaches farther to the west than normal and crosses track 4 before retroflecting back to the east. This stretching of the Agulhas retroflection to the west provides favorable conditions for eddy formation. Strong flows in opposite directions and in close proximity to each other such as those depicted around day 80 in Fig. 13d may represent developing eddies.

6.3. Transport time series

Another way to look at the absolute flow across these tracks is to plot the estimated transport between selected points on the track. The volume transport across a track is the integration of cross-track velocity along the track and with depth. From equation (2.8),

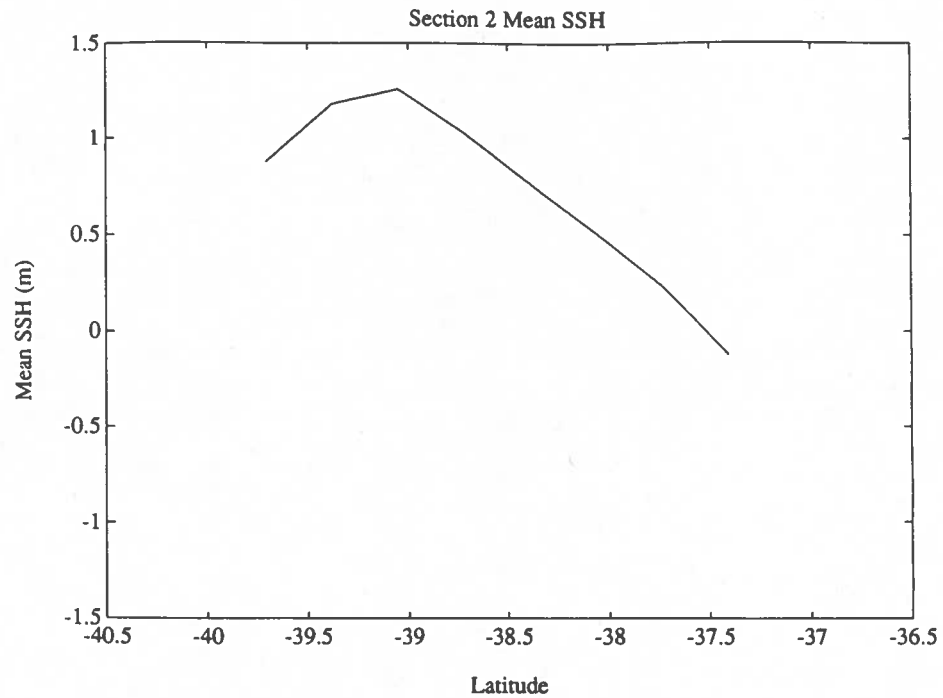
$$\int_A^B u \partial y = -\frac{g}{f} \int_A^B \partial h = -\frac{g}{f} (h_B - h_A) \quad (6.1)$$

Therefore, an index of the transport between points A and B per unit depth is simply the difference in absolute sea level between the two points. The difference in absolute sea level between selected points on tracks 2 through 5 is plotted in Figs. 14a-14d. The difference has been smoothed with a three point Hanning filter and a line is drawn through the median value on each plot to represent the central tendency. Since cross-track transport largely cancels itself out on portions of the track where flow consistently reverses direction, points between which a steady mean surface slope is shown in Fig. 12 are used as end points for calculation of the transport index. For example, the transport index for track 3 is computed between approximately 38S and 39S rather than for the whole track. Positive (negative) transport indices indicate current flow in the easterly (westerly) cross-track direction. The character of the variations about the median changes from one track to the next. The transport index across section 2 varies in a fairly regular manner with an amplitude of about 0.5 meters, and demonstrates the 50-150 day period discussed previously. In contrast, sections 3 and 4 seem to have less regular fluctuations in transport, marked by larger events of about 1 meter in amplitude. The large events around days 100 and 400 in Figs. 14b and 14c seem to be related, with track 3 leading track 4 at the start of both events. This type of transport signature might occur when part of a meander stretches across both tracks. Cross-track transport reflects the position of the current relative to the section as well as the strength of the current. Section 5 transport has regular, smaller variations like section 2, but they seem to be superimposed on an additional low-frequency signal. An inter-annual fluctuation in the easterly current to the south of the Agulhas may be responsible for this signal, since it is not visible in the other plots. Except for the large events across sections 3 and 4 discussed above, there does not appear to be a strong correlation between transports across the four sections.

6.4. Summary of results

ADCP velocities from one cruise were combined with GEOSAT relative sea level measurements to compute the mean ocean surface signal between November 1986 and November 1987. GEOSAT relative sea level measurements were then added to the computed mean signal to obtain a two year time series of absolute sea level. The current flow corresponding to the absolute surface

slope agrees with what is known about the Agulhas current. Unlike the relative flow normally computed from altimeter measurements, the absolute flow can be used to detect changes in the current's path and to estimate transports across the sections. For instance, the direction of calculated flow changes frequently across sections 3 and 4, probably a result of the meandering of the retroflection. Regular fluctuation in transport across sections 3 and 4 seems to be occasionally interrupted by larger events, possibly related to meanders. In contrast, variations in the strong easterly transport across section 5 seem to be superimposed on an unexpected low-frequency fluctuation which is not evident in the other sections.



(a)

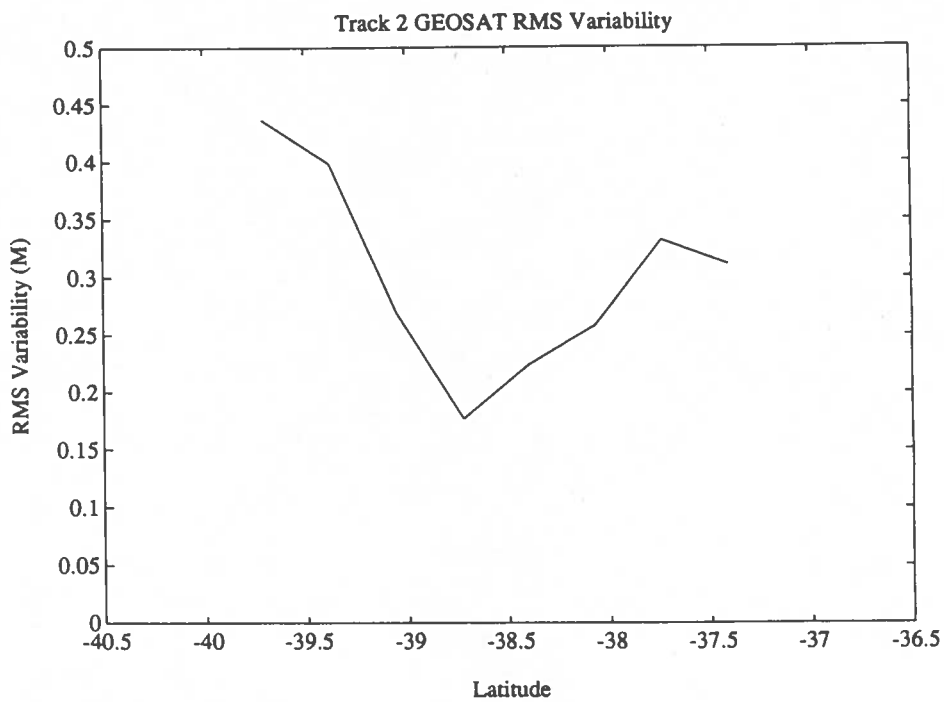
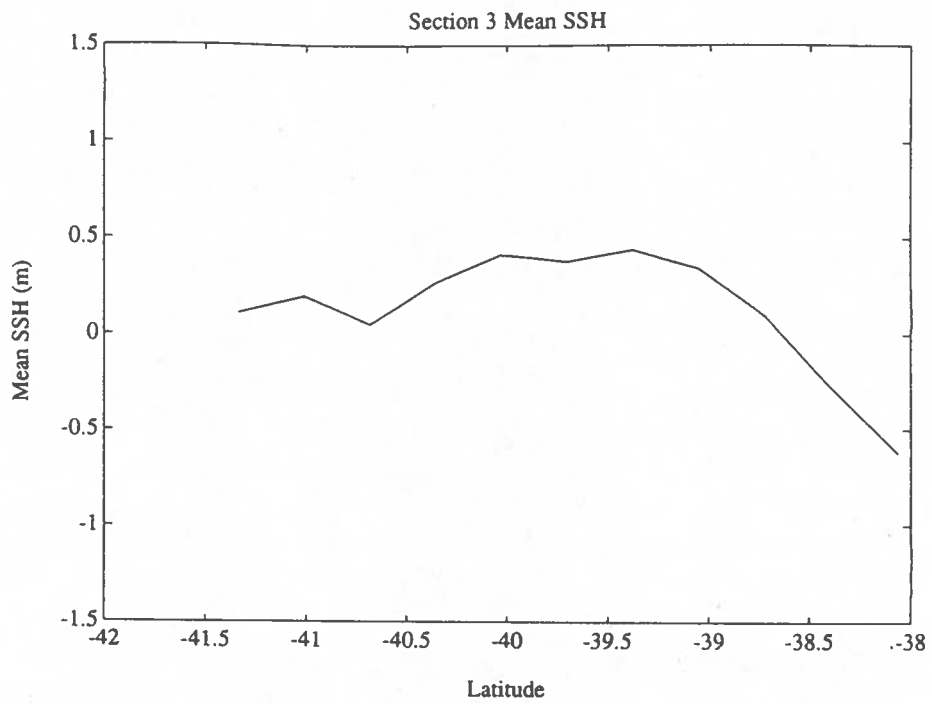
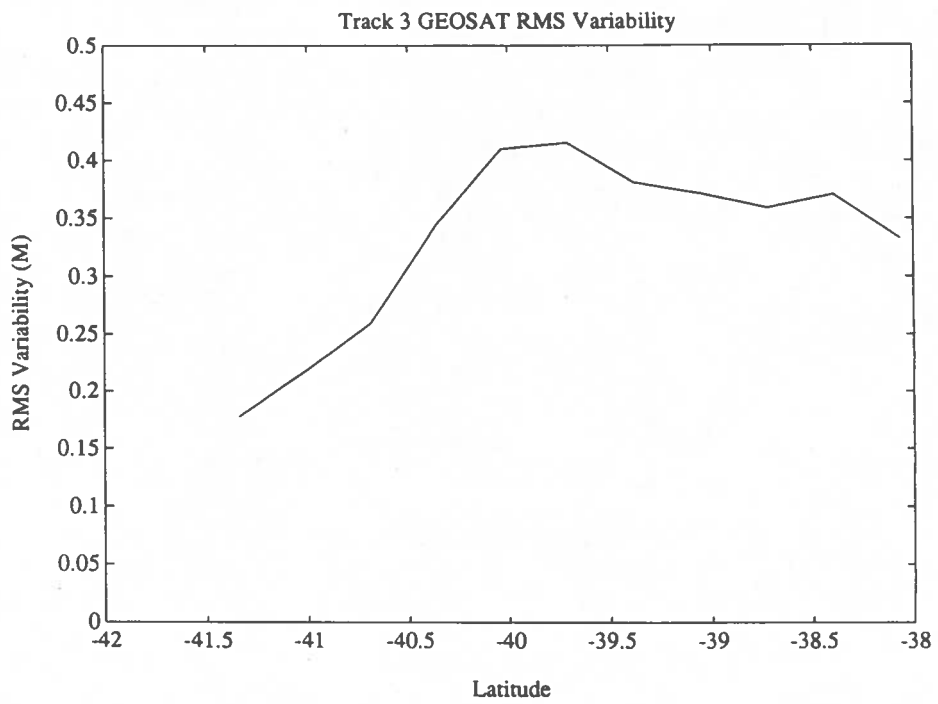
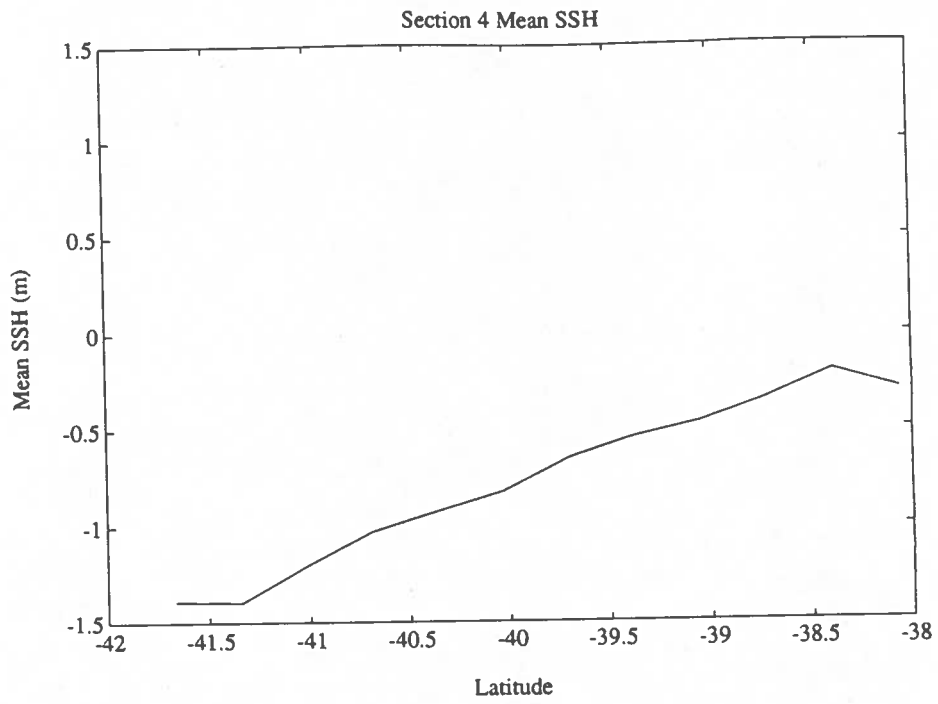


Fig. 11. Mean sea surface height and GEOSAT-measured RMS variability along (a) section 2, (b) section 3, (c) section 4 and (d) section 5.

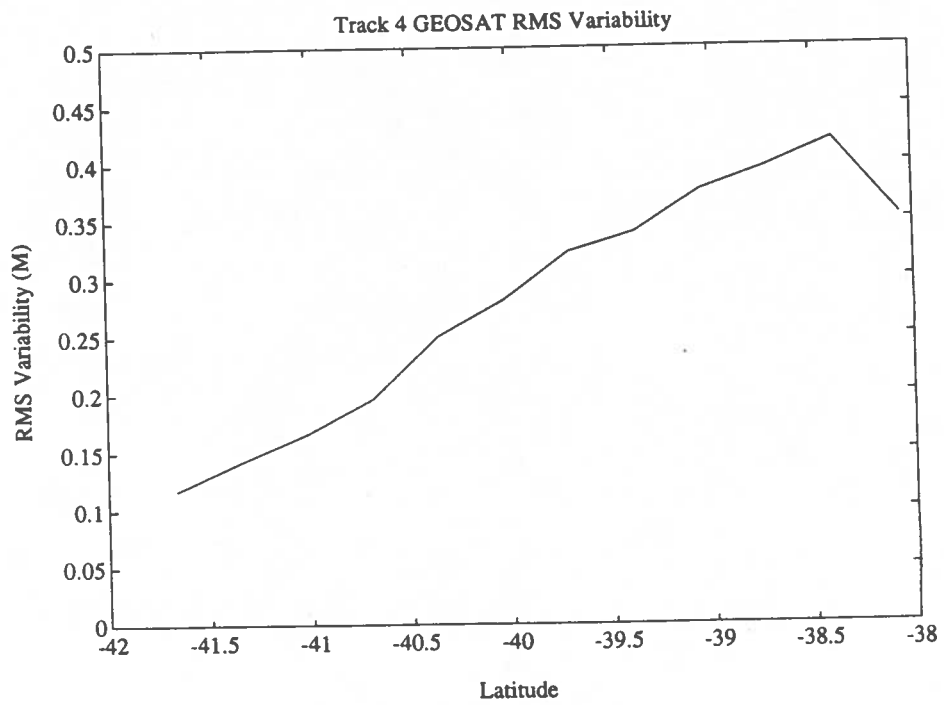


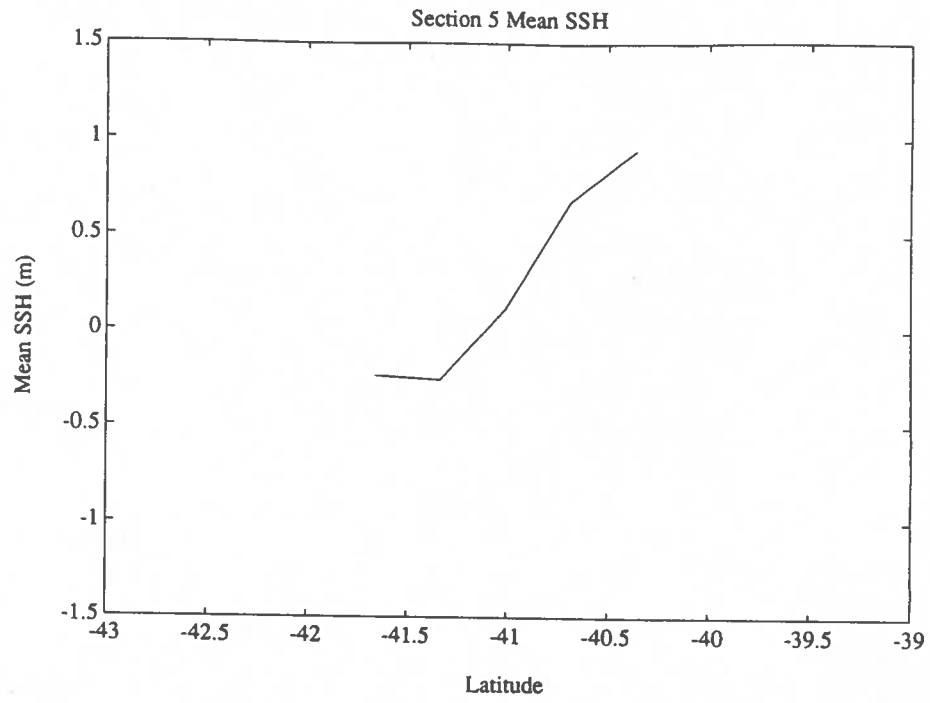
(b)



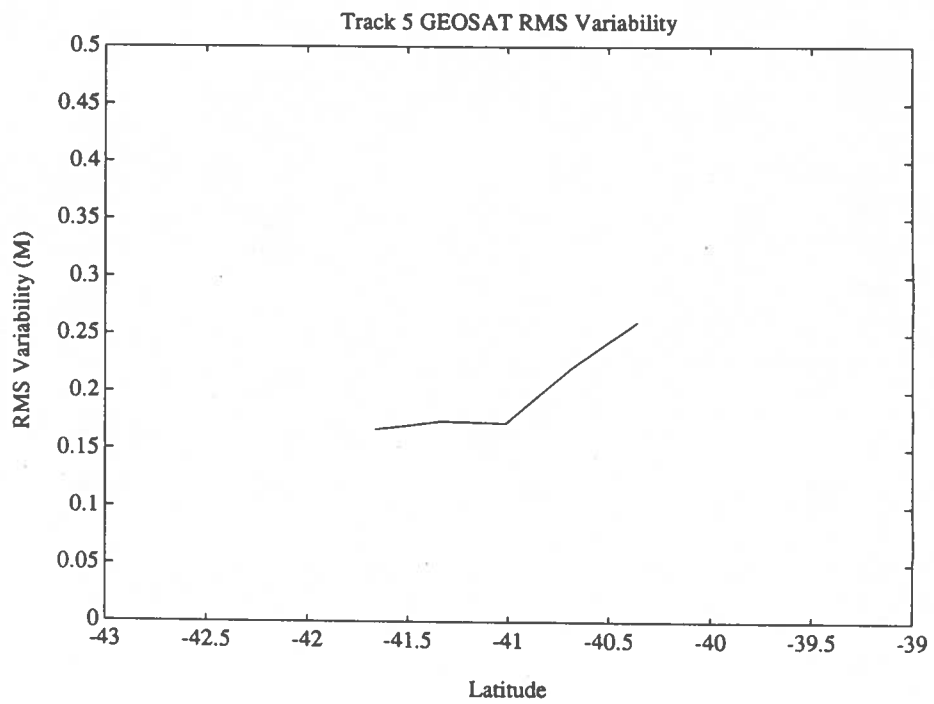


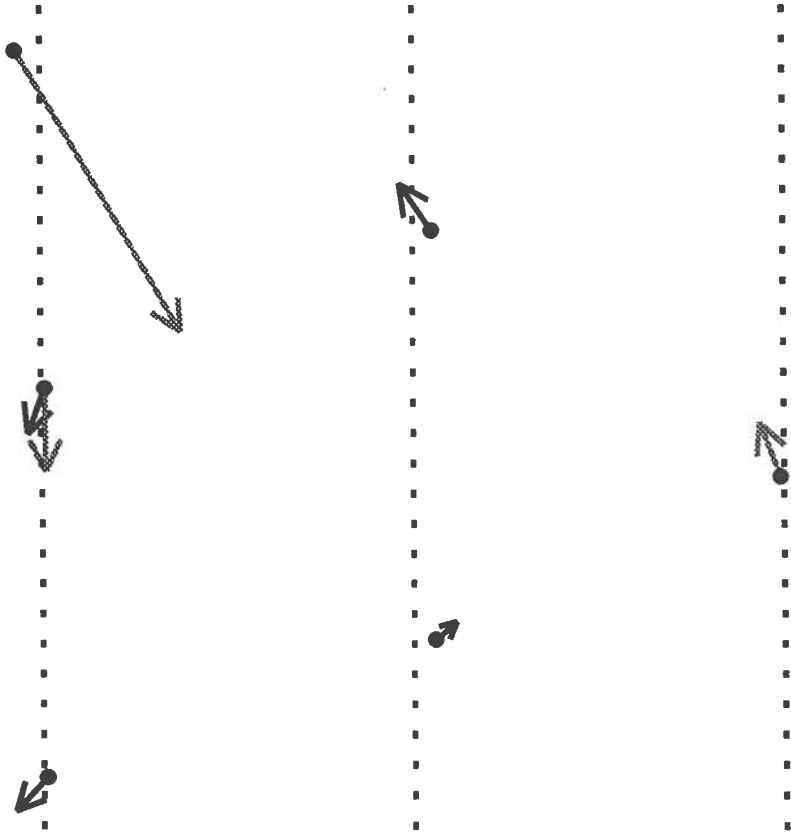
(c)





(d)





1 m/s

A horizontal arrow pointing to the left, with a small black dot at its tail on the right. The text "1 m/s" is positioned below the arrow.

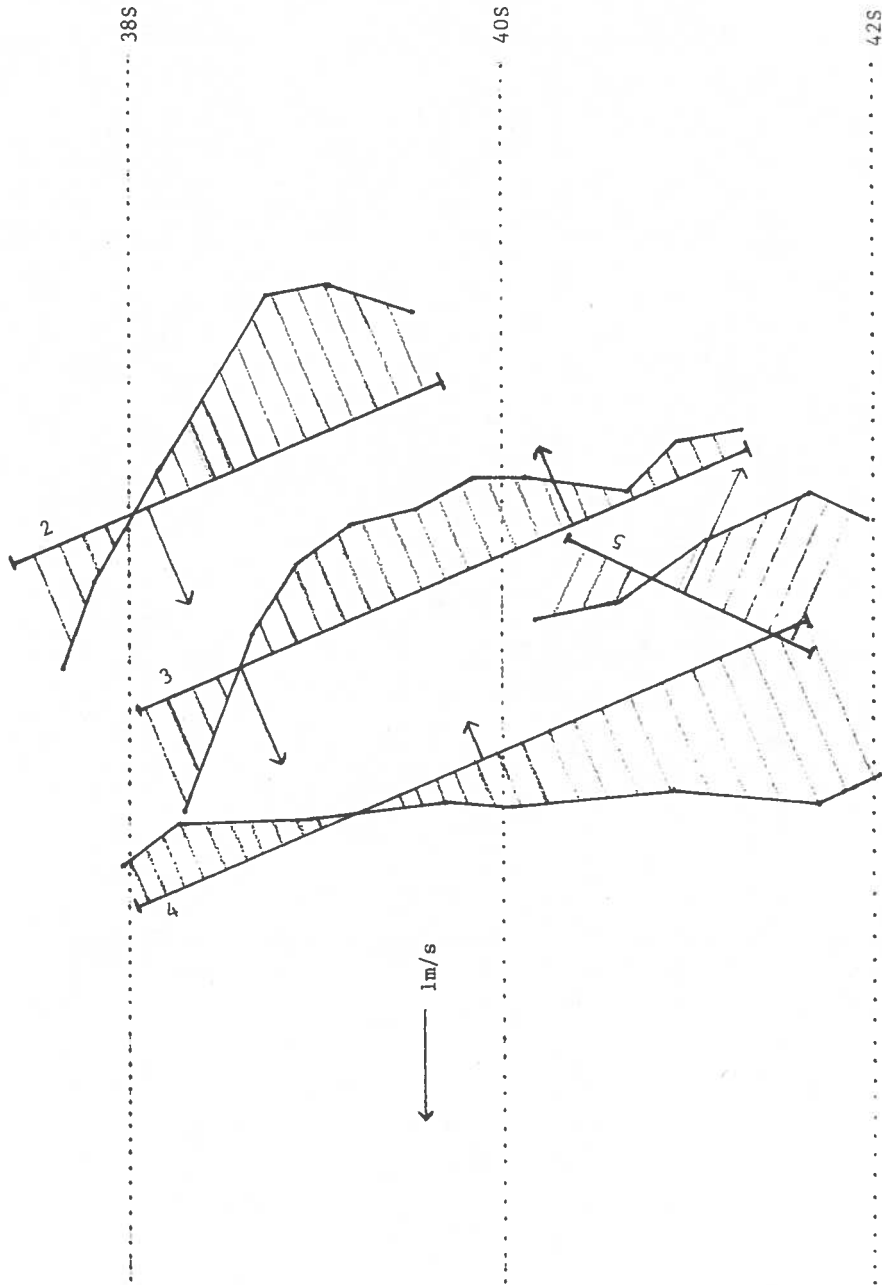


Fig. 12. Mean sea surface height and resulting mean cross-track current plotted on a map of tracks 2-5. Overlay shows mean current at approximately 200 m (dashed) and 750 m (solid) measured by moored current meters.

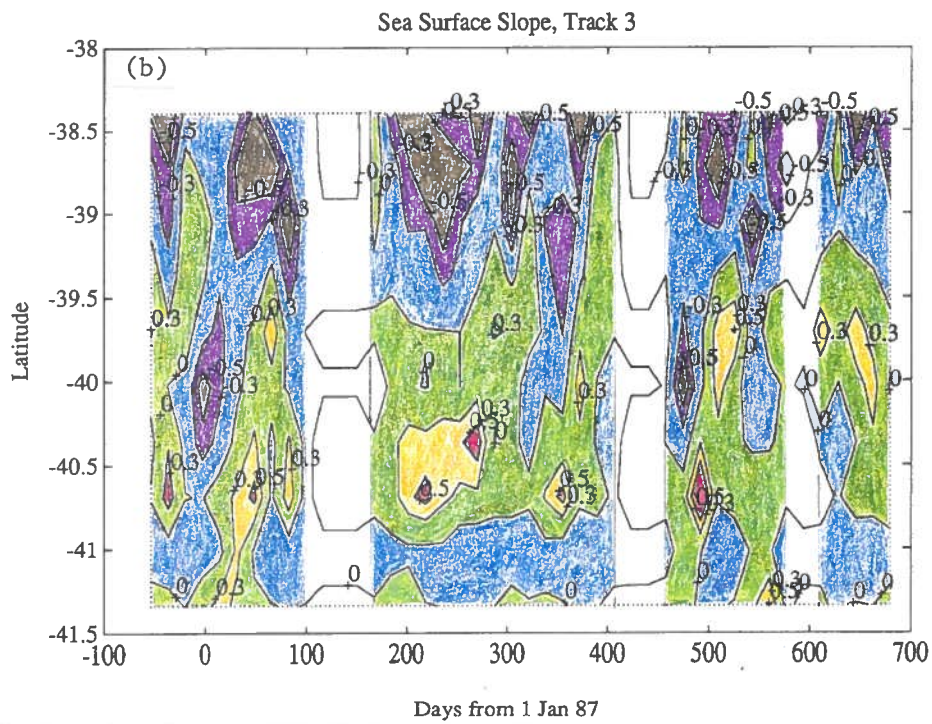
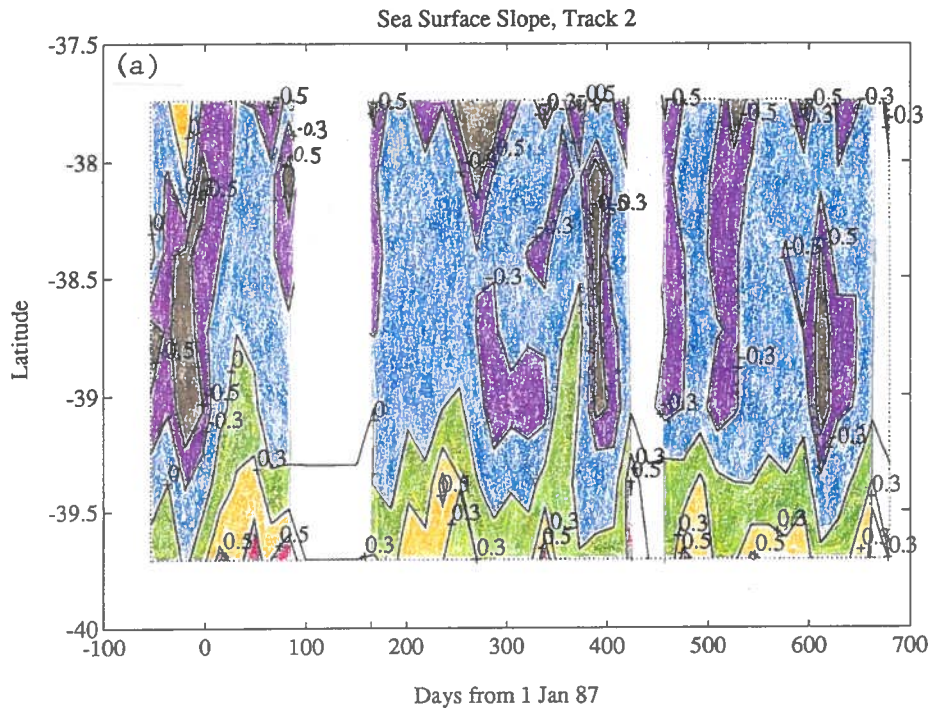
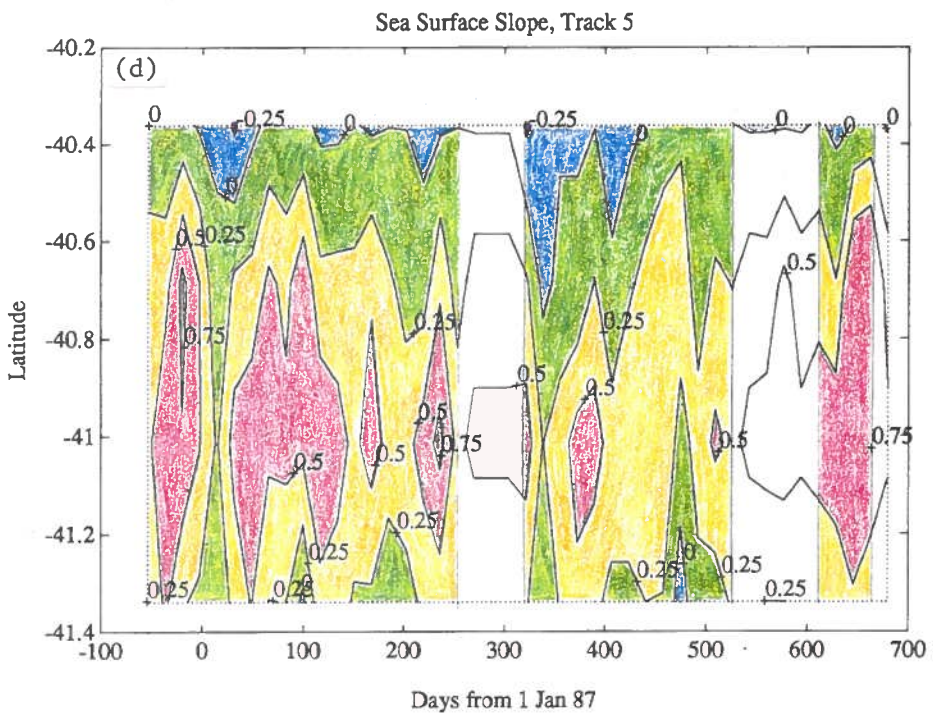
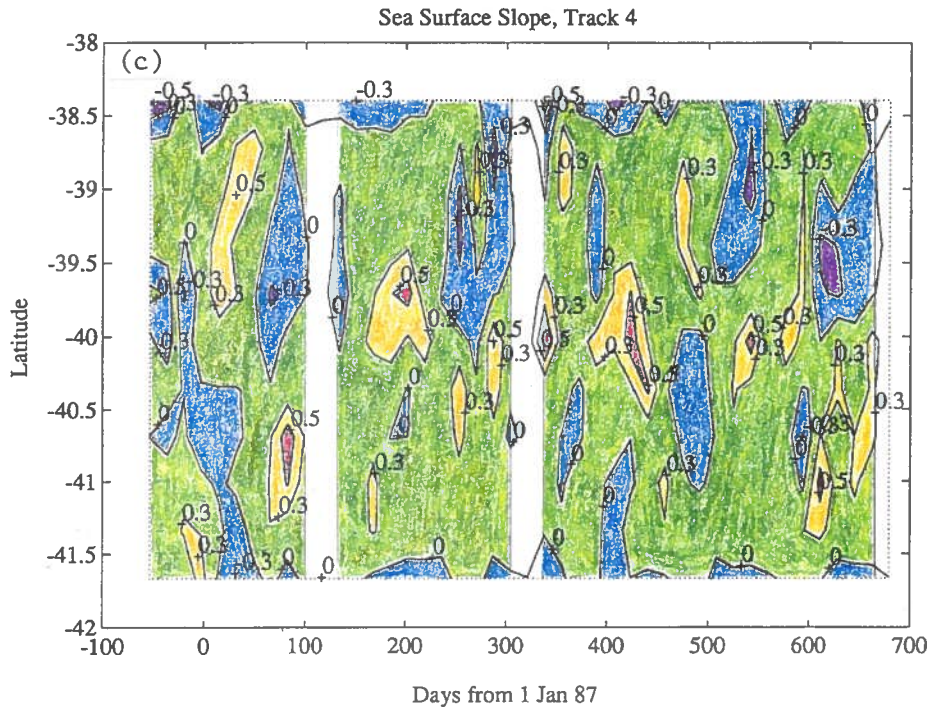


Fig. 13. Time series of absolute sea surface height slope along (a) track 2, (b) track 3, (c) track 4 and (d) track 5. This slope is directly proportional to absolute current flow across the tracks. Gaps in GEOSAT data are unshaded.



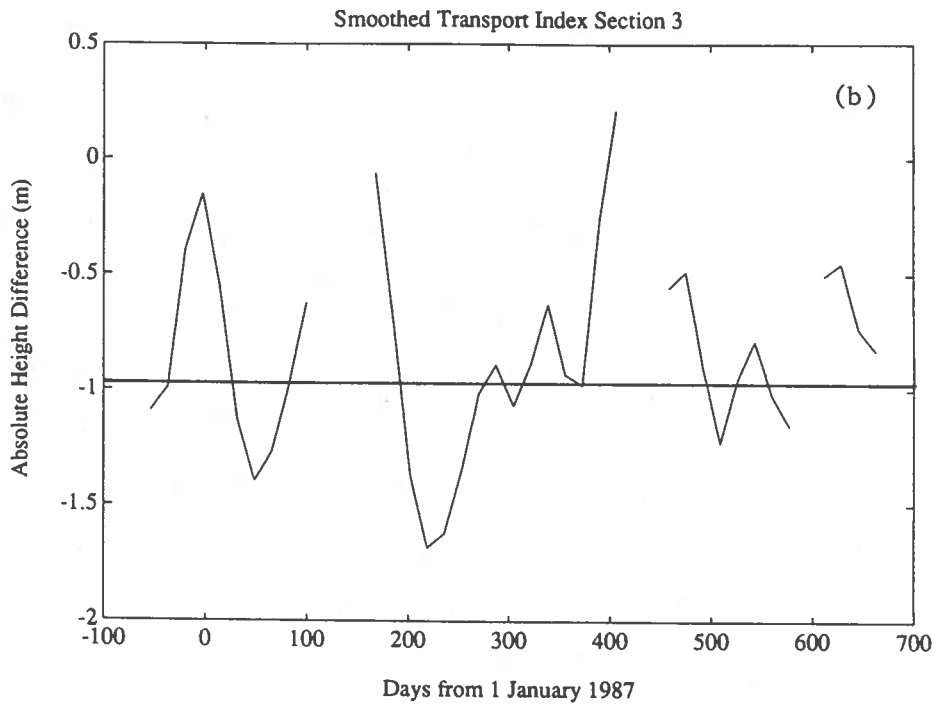
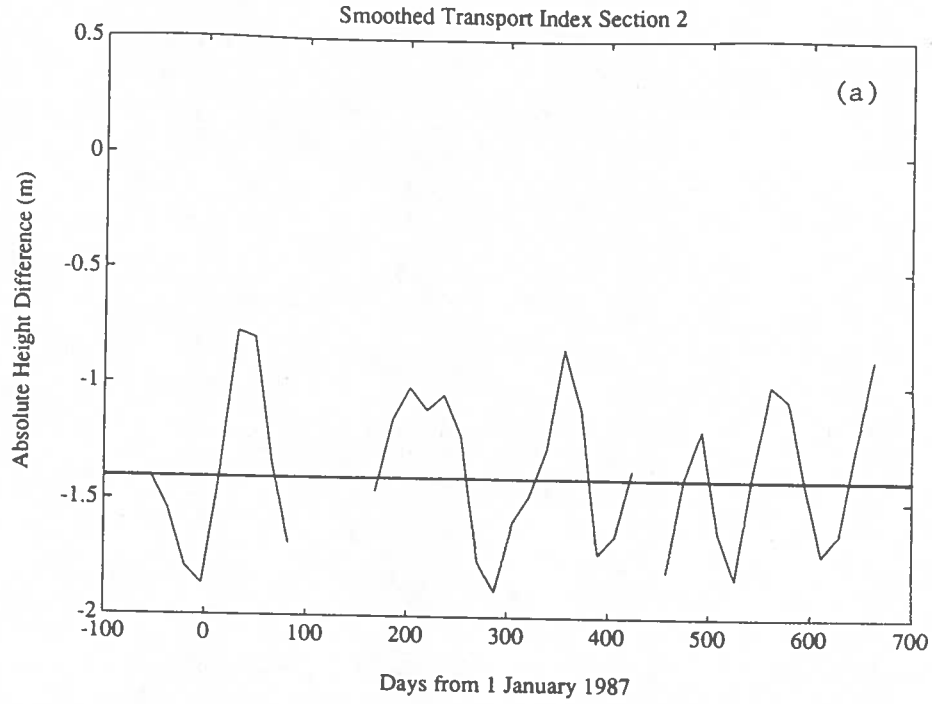
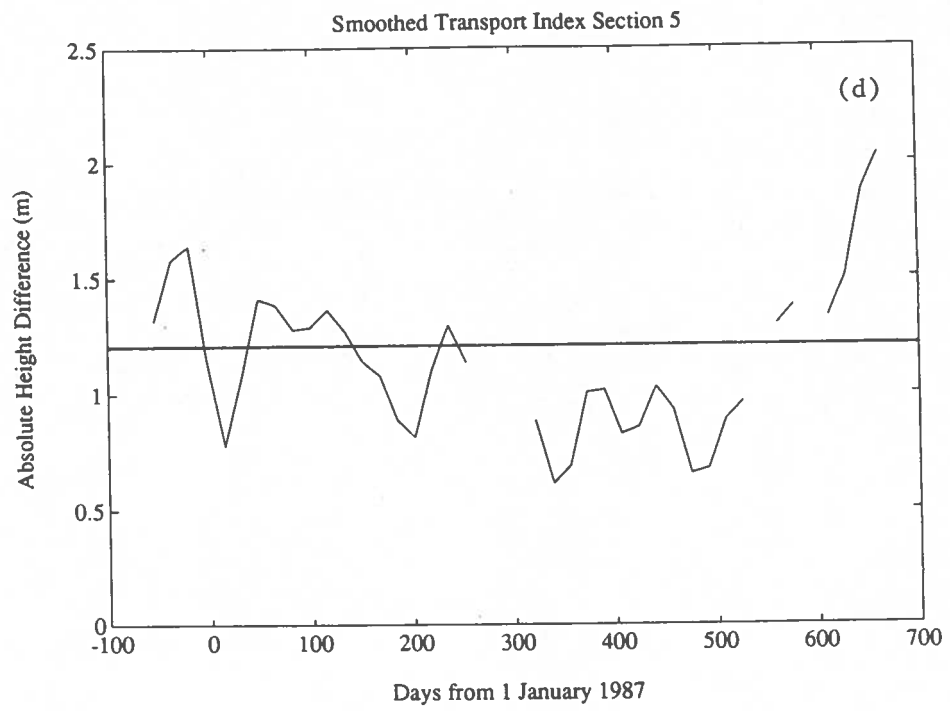
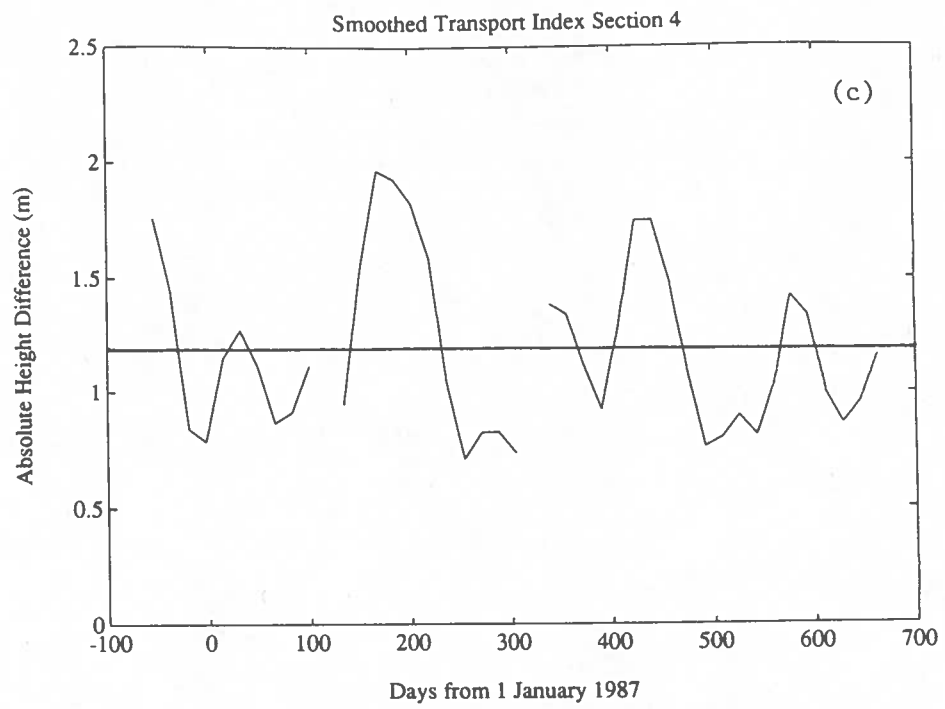


Fig. 14. Smoothed absolute sea surface height difference between selected points on (a) section 2, (b) section 3, (c) section 4 and (d) section 5. Absolute height difference serves as an index for transport across the section. Breaks in plots are GEOSAT data gaps.



CHAPTER 7

FINAL CONCLUSIONS

The method of combining shipboard and GEOSAT measurements to obtain a mean sea surface height and then adding GEOSAT relative sea level measurements to this mean height to obtain absolute flow seems promising based on this work. For the RRS Discovery cruise in the Agulhas retroflection, measurement uncertainties and ageostrophic effects amounted to 12.5% of the mean sea surface height difference computed across the current, which should not seriously degrade final estimates of absolute flow. The absolute current series obtained seems reasonable based on what is known about the retroflection area and displays many interesting features for future study.

Ageostrophic effects and measurement uncertainties may become more significant problems if the technique is used in areas of weaker current flow. In such areas, using an absolute sea level calculated from combined hydrographic and ADCP data as discussed in chapter 5 may help reduce errors due to ageostrophic effects. Careful pre-cruise calibration of the ADCP (not available on the RRS Discovery cruise) would reduce instrument error and subtracting a longer-term mean from the GEOSAT data during processing would reduce altimeter measurement uncertainty. Future cruises might be designed to take advantage of this method by timing ship transits to coincide as closely as possible with satellite passes in addition to planning the ship's route over GEOSAT ground tracks (*cf.* Joyce *et al.*, 1990). The ship tracks could also be arranged in grids which would allow for more rigorous estimation of divergence and advection terms. Because of its strong flow, these issues have a minimal impact on the results obtained for the Agulhas current. This method provides a realistic picture of the Agulhas current and has potential application to other areas of the ocean.

APPENDIX A

SIGNIFICANT WAVE HEIGHT IN THE AGULHAS CURRENT

Numerous ships have reported unusually steep, high waves in the Agulhas current off of South Africa. It is estimated that a supertanker is damaged or sunk in the region every year by such a wave (Irvine, 1987). Case studies indicate that the waves appear unexpectedly from relatively calmer seas and reach heights of up to 18 meters (Mallory, 1974). A long, sloping trough is typically followed by an extremely steep wave face which can break over the bow of a ship, making the waves particularly dangerous.

The cause of these extreme waves is still unknown. One hypothesis, proposed by Mallory (1974), is that superimposed swells from two or more different weather systems come into phase with each other for a short time. The fast Agulhas current, when flowing against the swell, adds to the height of the superimposed waves. Consistent weather patterns were prevalent before many of the reported incidents, implying that particular combinations of swell may be more likely to produce the unusual waves. Another possible cause suggested by Irvine (1987) is the refraction of waves by the Agulhas current. Irvine uses a model to demonstrate various effects of an opposing current on an incident wave field. The model shows that a slight curvature in the Agulhas could cause an opposing wave field, incident at 10 degrees or less, to reflect off of its inner boundary. This reflection concentrates the wave field in the current. Meanders could cause enough refraction to produce wave trapping within the current. Focusing of wave energy by refraction might be responsible for the formation of unusually large waves in the midst of otherwise ordinary local wind and wave conditions. Study of wave height patterns and corresponding current flow could help to determine the actual cause of the unusual waves.

GEOSAT altimeter data provides a means to identify wave height patterns in the area which would help to confirm or disprove the theories on extreme wave formation. The GEOSAT altimeter exact-repeat mission provides significant wave height data over identical tracks in the Agulhas region every 17 days. Significant wave height is defined as the average height of the highest one-third of the waves. Significant wave height during the first two years of the GEOSAT exact repeat mission (November 1986 - November 1988) was accessed using software designed by Caruso *et al.*, (1990) and plotted along several tracks crossing the Agulhas current (Fig. A-1). Since the chosen tracks cross portions of the current where meanders are usually found, increased wave height along these tracks may indicate concentration of wave energy by refraction or superposition. The altimeter does

not measure heights over land, so some of the tracks end at the South African coast. The Agulhas flows along a narrow continental shelf, within 10-15 km of the coast in some places. Therefore, when smoothing the data, a small filter width is desired to minimize data loss over the Agulhas. Significant wave height was filtered using an 11-point least squares fitted line. Since altimeter measurements are taken approximately every 7 km along-track in this region, the filter loses about 38 km at the end of each track. The Agulhas is between 90 and 165 km wide (Mallory, 1974), so its effect on significant wave height should be retained in the smoothed plots.

Figs. A-2a and A-2b show the un-filtered and smoothed significant wave heights ($H_{1/3}$) along track d006 for repeat pass 034 (June 9, 1988). Note the two large peaks near 36S and 40S. The peaks coincide with a typical position of the Agulhas current and its retroflection depicted in Fig. A-1. Similar peaks at current crossings were common in significant wave height plots along all the tracks studied. However, large significant wave height was also prevalent to the south of the Agulhas. This is not surprising in view of the strong storms and long fetch of the Southern Ocean. Development of extreme waves which are uncharacteristic of the surrounding sea state would be better identified by plots of the change in significant wave height along the track. Such plots would peak where superposition of waves or refraction caused sudden intensification of the wave field, but not where waves were consistently large. Therefore, the rms slope of the smoothed significant wave height plots was computed. Fig. A-2c shows this slope for track d006, pass 034. Note the small rms slope to the south of 42S in Fig. A-2c compared to the large significant wave height for this section in Fig. A-2b. The plot of significant wave height slope highlights the peaks which seem to coincide with the Agulhas crossing. Significant wave height rms slope for several other representative tracks and passes is shown in Figs. A-3a through A-3d. Most major features in these plots coincide with the expected position of the Agulhas current.

If the increased significant wave height slope indicated by individual GEOSAT passes over the Agulhas current reflect a regular wave-building phenomenon, we could expect a similar increase in a long-term average rms slope as well. Both significant wave height and its rms slope were averaged over approximately two years. The rms slope was filtered with a 24-point, along-track averaging filter before being time-averaged. This filter preserved important features on several test plots of the data while removing much of the noise. Fig. A-4 shows representative plots of the averages. Although the average significant wave height declines steadily from south to north, the peaks in average significant wave slope occur in the vicinity of the Agulhas current and retroflection. This characteristic is common to all the GEOSAT tracks along which averages were plotted.

Individual and averaged plots of significant wave height and rms slope seem to indicate some type of wave-building phenomenon associated with the Agulhas current. Although the correct

theory of how extreme waves are formed in the Agulhas current cannot be confirmed with height and slope fields alone, the combination of this type of data with other observations may provide the answer.

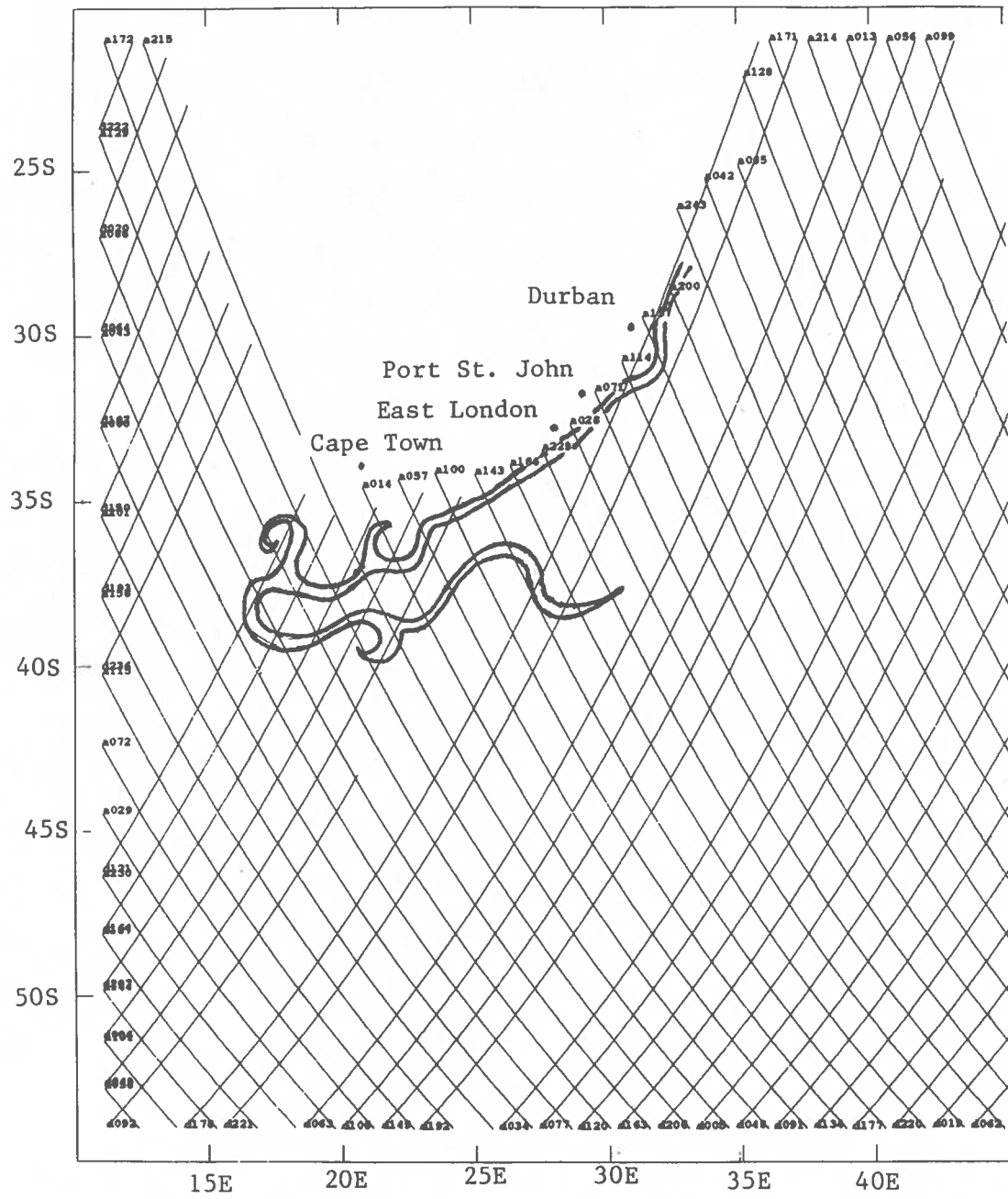
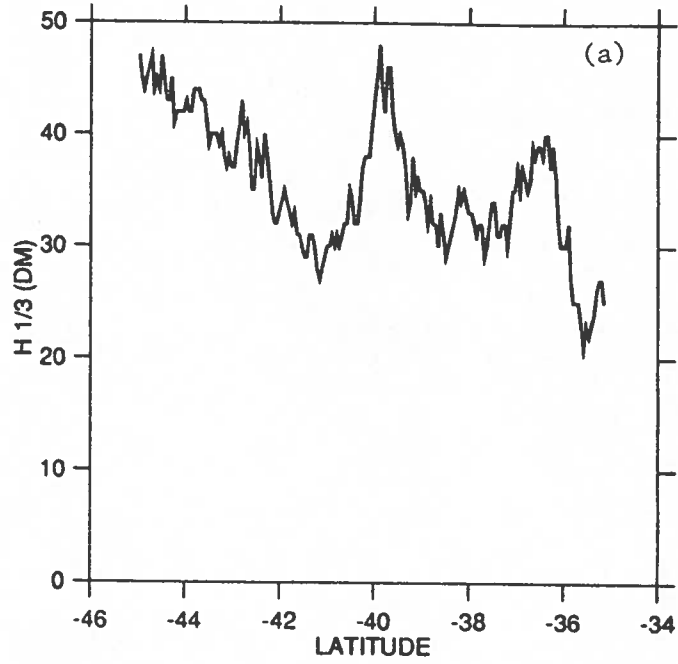


Fig. A-1. Numbered GEOSAT tracks near South Africa. A typical position of the Agulhas current is depicted.

w034.d006



w034.d006.av

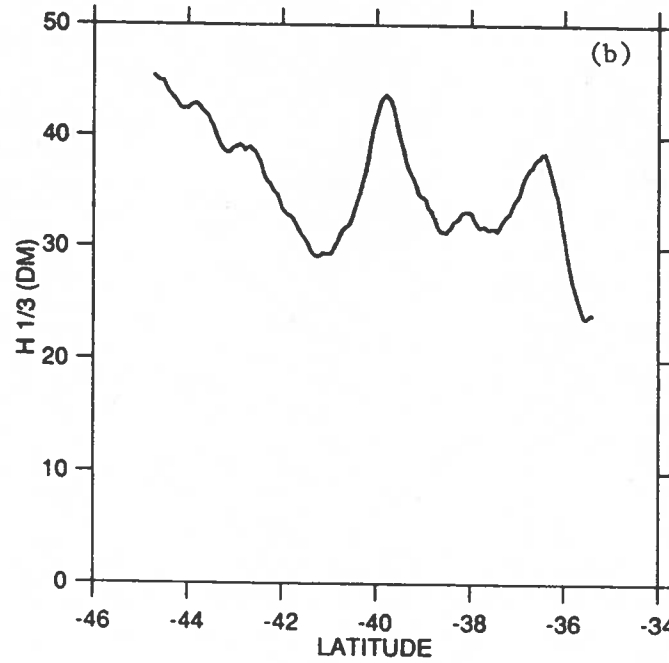
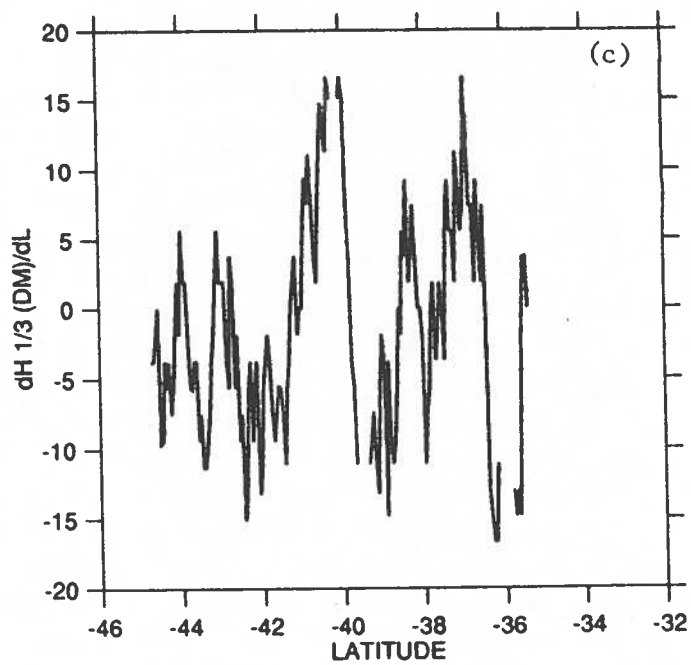
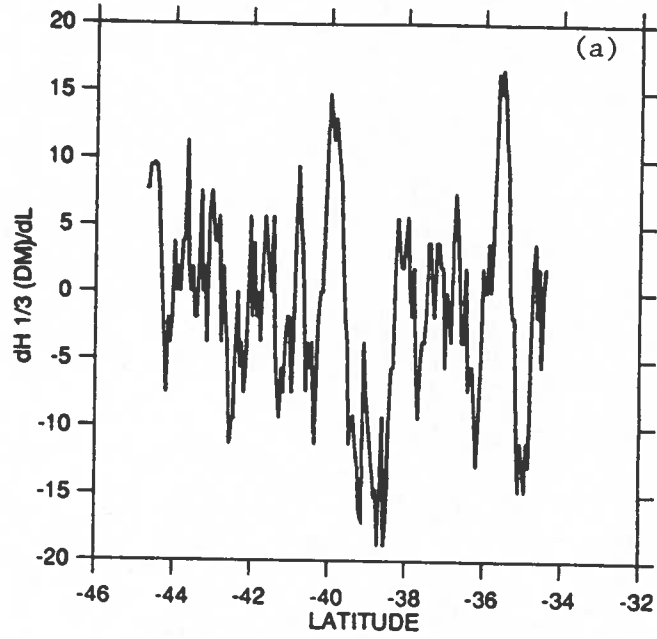


Fig. A-2. Un-filtered (a), smoothed (b) and rms slope of(c) significant wave height along GEOSAT track d006, pass 034 (June 9, 1988). Height is in decimeters; slope is in decimeters/degree latitude.

w034.d006.av.dif



w006.a057.av.dif



w033.a057.av.dif

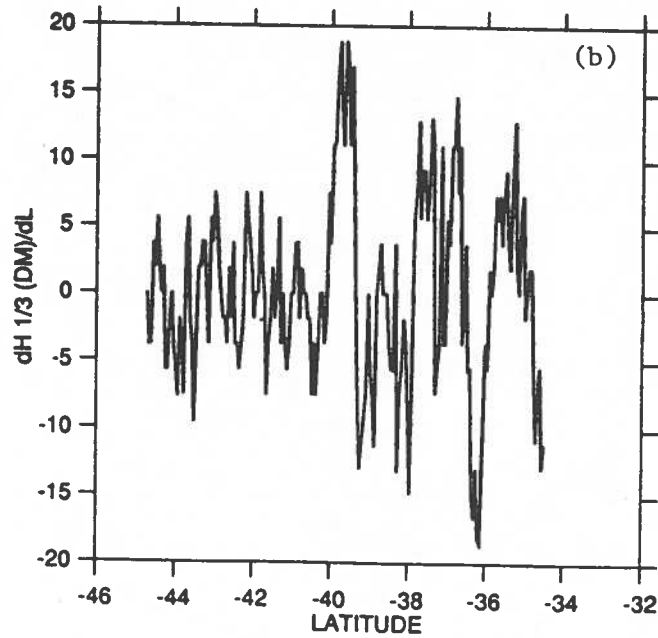
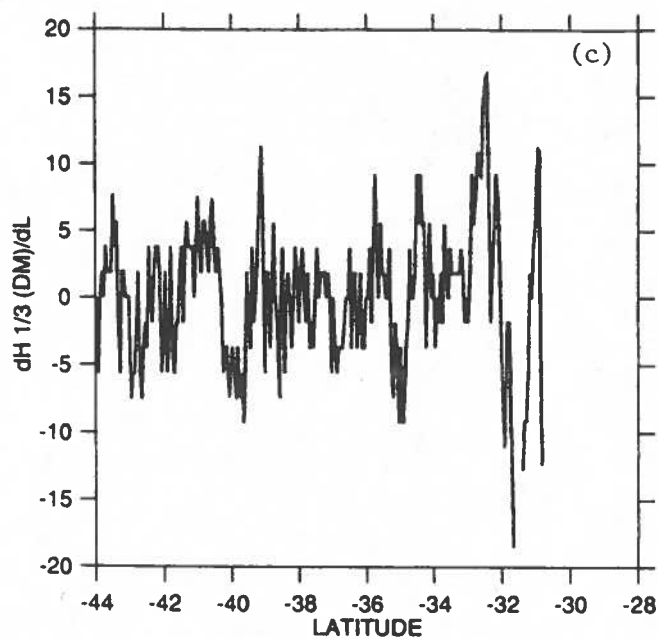
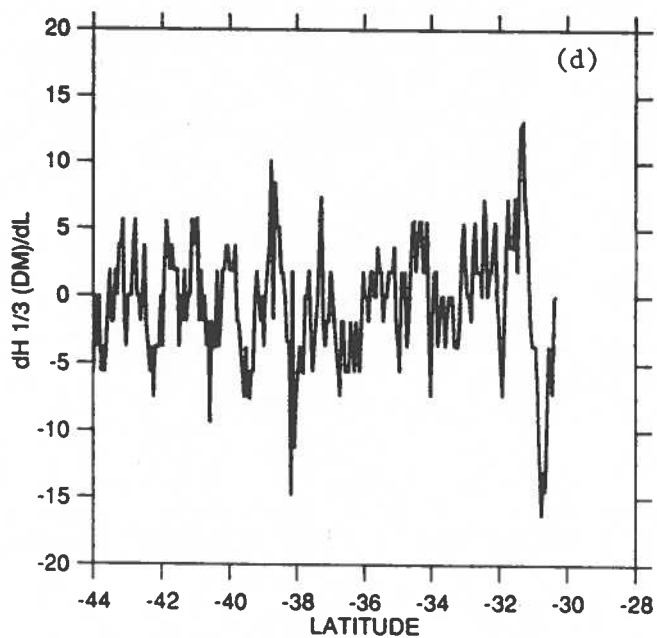


Fig. A-3. Representative plots of significant wave height rms slope (in decimeters/degree latitude) for individual passes along the tracks.

w005.a114.av.dif



w001.a157.av.dif



(a)

a129

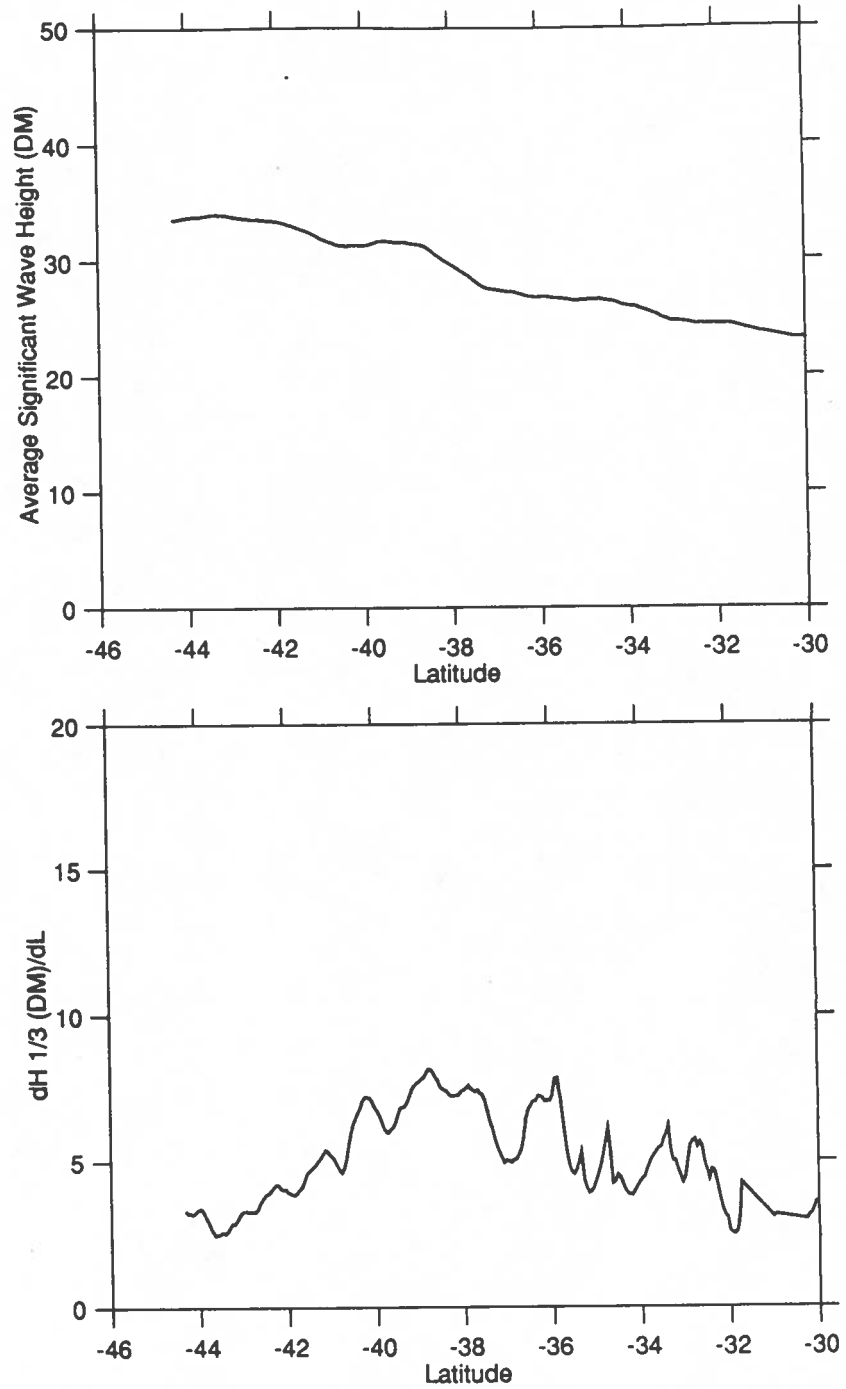
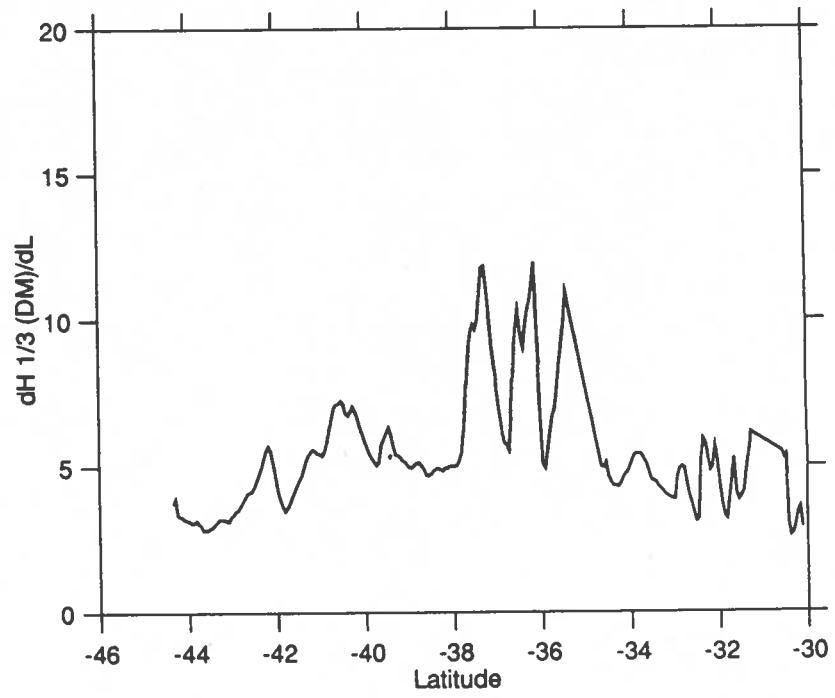
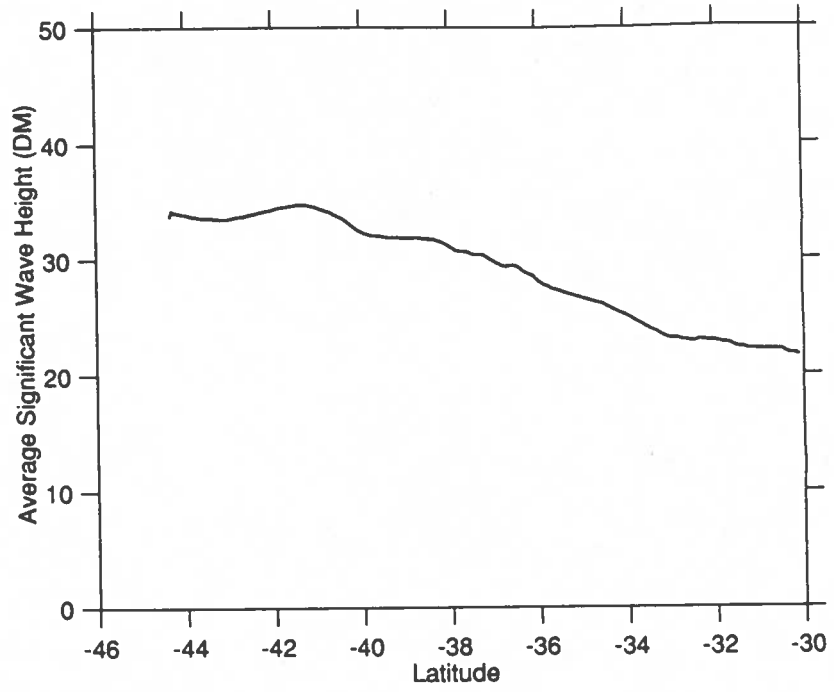


Fig. A-4. Representative plots of average significant wave height (in decimeters) and rms slope (in decimeters/degree latitude).

(b)

a172



APPENDIX B

ACOUSTIC DOPPLER CURRENT PROFILING OF THE AGULHAS RETROFLECTION DURING R.S.S. DISCOVERY CRUISE 165A

1. Introduction

Acoustic Doppler Current Profiler data was collected in the Agulhas Current and Retroflection zone during *R.R.S. Discovery* Cruise 165A. A description of the data processing is provided along with the resulting current measurements, presented in vector plots on a horizontal map and in along-track contour plots of cross-track velocity.

2. Instrumentation

The *R.R.S. Discovery* operated an RDI VM-150 (150 khz) Acoustic Doppler Current Profiler (ADCP) throughout most of the cruise. The ADCP transducer transmits sound pulses approximately once per second in four separate beams. Each beam is oriented at a 45 degree angle from the ship's fore and aft axis and a 30 degree angle from the ship's vertical axis. The Doppler frequency shifts of the backscattered sound signals are then used to compute current velocity relative to the ship. The transducer was mounted approximately 20 meters aft of the bow of the ship on a shaft which could be retracted within the ship's hull or extended about 2 meters below the hull. The system was generally operated in the extended position, where noise from the propellers and aeration of the water due to wave action would be reduced. The returns were averaged into 8-meter bins, with an available data range of 16 to 408 meters. An IBM-PC computer was used with the standard software provided by RDI to control the profiler, receive the data, vector-average profiles in two minute ensembles and record the data on disk. Heading information was obtained from the ship's gyro stepper interface. Navigation data from a Trimble GPS Surveyor and a Magnavox 1107 Transit system were logged separately by the ship's Plessey computers for post-processing with the ADCP data.

3. ADCP data processing

ADCP processing was done using a series of programs developed at UH which are centered around the Common Oceanographic Data Access System (CODAS), a database originally designed by Ramon Cabrera. Some modifications were made to apply the routines to the Agulhas data set, but the

basic processing procedures described by Bahr *et al.* (1989) were unchanged. Figure B-1 summarizes the processing steps.

3.1. Quality evaluation

Average ADCP information along straight segments of the ship track was plotted to get an initial feel for the quality of the data. Profiles of the average value and standard deviation of amplitude, percent good, w -component velocity, error velocity, U -component first difference and V -component first difference revealed several characteristics of the overall data set. Figs. B-2 through B-7 are representative samples of these plots.

The amplitude (returning signal strength recorded at the instrument) was typically high at shallow depths, and dropped off to the noise level at depths between 200 and 300 meters. Percent good (percentage of pings within the two minute ensemble which had acceptable data from all four of the transmitting beams) was generally 95-100 percent down to a depth of around 200 meters, where quality of the current velocities began to deteriorate due to distance from the transducer. As described by Bahr *et al.* (1989), two independent estimates of vertical velocity are given by the ADCP. The w -component velocity is the average of the two estimates, and the error velocity is $\cos(30^\circ)/2$ (≈ 0.433) times the difference between the two. As true vertical velocity in the ocean is normally small, both the w -component and error velocities should also be small over the depth range of reliable ADCP data. Although most of the w -component profiles were approximately zero down to a depth of 200-300 meters, the error velocities ranged from 0 to -6 cm/s. Standard deviation of both w -component and the error velocity was small (~ 1 -3 cm/s) in this depth range. Study of cruise conditions, ship's heading and ADCP data collection did not reveal any explanation for these non-zero error velocities. A "tail" or sudden change in most profiles near the surface (especially percent good and velocity profiles) indicated erratic measurements in the top bin (16 meters). Therefore, the top bin was edited out of the data.

Two segments from 10-12 Feb had lower overall quality than the others, as evidenced by lower percent good values and higher standard deviation in percent good and error velocity. This may have resulted from rough weather, as high winds were noted in the ship's log during this time. All profiles were compared to detect any pattern of error due to ship's heading, but no consistent differences appeared between segments of different heading.

3.2. Loading and Editing

The first step in ADCP data processing is to load the data into the database and check for data errors. During this process, sound speed in the water is normally calculated from surface water temperatures measured at the ADCP transducer. However, many of the recorded temperatures were uncharacteristic of Agulhas surface water temperatures. The ADCP log indicated that the ADCP system had "crashed" many times due to temperature problems. On 9 Feb at 16:30, the setting on the ADCP was changed to a constant sound speed, thus avoiding further system failures due to erratic temperature measurements. The fixed sound speed selected did not correspond to temperatures and salinities measured by the CTD during the cruise. Therefore, nearly the entire data base had to be adjusted for sound speed errors. The average 10-20 db level water temperature and salinity based on CTD information provided by Read *et al.* (1987) were used to calculate the corrections. The variation in temperature and salinity measured by the CTD at this level corresponds to a maximum sound speed error of 6.3 m/s, which would have a negligible effect on horizontal velocity measurements.

The next step is to test each profile for several conditions which may indicate interference, glitches or other anomalies. Profiles flagged by this test were plotted and studied to determine what portion of the profile should be disregarded. Upon first inspection, several profiles with glitches coincided with the time frame of CTD stations. Therefore, profiles during CTD stations were systematically inspected, and anomalous values were edited out of the database.

3.3. Calibration

No calibration run was performed during this cruise. Calibration runs were conducted on the Discovery during the preceding cruise by steaming past transponders in opposite directions. However, calibrations from previous cruises are not reliable indications of the offset on subsequent cruises (Kosro, 1985). If sufficiently accurate navigation information is available during large turns or changes in ship velocity, amplitude and angle errors can be computed from the ADCP velocities during post processing (Pollard and Read, 1989). GPS navigation was only available during seven short periods of changing ship speed/direction. Angle offsets computed for these periods were all less than one degree and were not consistent enough to warrant a correction to the data. However, amplitude offsets for the seven calibration computations were consistent. Only five of the seven calibrations appeared reliable based on variance of the current measurements. The average amplitude offset for these five calibrations was 1.0154, which is close to the values calculated for the calibration runs from the previous cruise (between 1.015 and 1.067). This amplitude factor was applied to the data.

3.4. Navigation

The final step in processing ADCP data is to determine the ship velocity over the ground with navigation fixes, which is then used to calculate absolute water velocities. Basically, ship speed plus water velocity relative to the moving ship is equal to true water velocity. In practice, though, profile velocities are differenced from a reference layer velocity (average over bins 5-15, in this case). The absolute reference layer velocity is the sum of the ship speed over the ground and the average relative water velocity in the reference layer, measured by the ADCP. The final estimate of true velocities is made by adding the differenced profile to the final absolute reference layer velocity.

Fixes from Trimble GPS and Magnavox dual channel TRANSIT systems were screened and formatted by an editing program. GPS fixes are the most accurate (Pollard and Reed, 1989, indicated an accuracy of 10 m), but GPS was not available for much of the cruise. The accuracy of TRANSIT fixes is variable and depends heavily on the speed from the electromagnetic log. For TRANSIT fixes, if satellite elevation was not between 7 and 70 degrees, the number of iterations exceeded 3, or if the distance from the dead-reckoning position to the fix exceeded 4 NM, the fix was ignored in further calculations. After automatic screening and elimination of bad fixes, ship speed between remaining fixes was used to calculate an absolute reference layer velocity from bins 5 to 15 (40-120m depth). Additional erroneous fixes were identified by unlikely jumps in the plotted absolute reference layer velocity. These fixes were manually edited out.

Two sections of the absolute reference layer velocity (near decimal days 35.6 and 39.0) seemed oddly displaced, indicating a possible transducer rotation problem. Two incidences of "transducer slewing" were noted in the ship's ADCP log at times coinciding with these sections. GPS was not available during the first incident. Since TRANSIT cannot provide accurate enough ship speeds for rotational corrections, this section was edited out of the data. The second segment was corrected with a rotation angle calculated using adjacent water and ship velocities as follows. Using the notation of Bahr, *et al.* (1989), the velocity vector is expressed as a complex number $U = u + iv$. The corrected velocity U_c is related to the uncorrected velocity U_u by

$$U_c = A e^{i\theta} U_u$$

where θ is the misalignment angle in degrees counterclockwise from the gyro compass forward axis and A is the amplitude factor. Absolute reference layer velocity U_a is equal to the sum of the ship speed U_{ship} calculated from GPS fixes and the relative reference layer velocity U_r . If we assume that the absolute reference layer velocity was unchanged before and after the transducer misalignment, we can write

$$U_{a1} - U_{a0} = U_{ship1} + A e^{i\theta} U_{r1} - U_{ship0} - U_{r0} = 0$$

where the subscripts 0 and 1 denote values before and after the misalignment. Therefore,

$$A e^{i\theta} = \frac{U_{r0} - (U_{ship1} - U_{ship0})}{U_{r1}}$$

The correction angle calculated in this case was 65 degrees. After rotating this segment, corrected relative velocities were combined with navigation data to provide an estimate of absolute reference layer velocity.

Because the computed ship speed was constant from fix to fix, the initial reference layer velocity was effectively averaged over the distance between fixes, resulting in a spatial resolution of roughly the distance between fixes. This initial absolute reference layer velocity was then smoothed to provide a more consistent ship velocity throughout. A plot of the final, smoothed absolute reference layer velocity is provided in Fig. B-9. The smoothed ship velocity (difference between the smoothed reference layer velocity and the measured relative velocity for the reference layer) was fit with the available fixes to obtain the final ship track which was written into the data base and used in analysis and plotting. We used a Blackman and Tukey (1958) filter for this smoothing, with a half-width of 0.125 days or 3 hours. Since the maximum speed of the ship was about 10 knots, this gives a spatial resolution of 30 NM or better. The total resolution would then depend on both the fix to fix distance and the distance the ship traveled in 3 hours. The average fix to fix distance was about 30 NM, so the data resolution is about equally dependent upon the distance between fixes and the ship's speed. The maximum distance was 165 NM (occurring twice), the next largest distance was 145 NM, and the remaining distances were all 75 NM or less.

4. Discussion of errors

There are many potential problems with the accuracy of currents measured by ADCP. Kosro (1985) provided a thorough discussion of errors from which the following highlights are extracted.

First, noise-induced variability occurs as a result of the finite bandwidth and finite time for frequency resolution within each range bin. Kosro analyzed the variability of his data and concluded that wave induced variability was the major contributor at periods up to one minute. Block averaging over 100 or more samples reduced the noise to a few cm/sec. The Agulhas data were averaged over approximately 120 samples (1 ping per second for two minutes).

Next, problems occur in the transformation of data from relative to geographical coordinates. Kosro's analysis indicated that the errors in horizontal velocity resulting from pitch and roll

were negligible. Pitch and roll compensation was not applied to the Agulhas data. The primary source of error in coordinate transformation is the heading angle. The equations for rotation of a coordinate plane about the origin counterclockwise through n degrees are:

$$x' = x \cos n - y \sin n$$

$$y' = x \sin n + y \cos n$$

These formulas can be applied to velocities in the x and y directions to obtain the velocity errors resulting from rotational offsets:

$$u' - u = u (\cos n - 1) - v \sin n$$

$$v' - v = v (\cos n - 1) + u \sin n$$

where u' and v' represent velocities in the rotated coordinate system (ie. the velocities which would be calculated if the gyro were n degrees off in the counterclockwise direction). For example, the u and v current velocity errors for a ship travelling north at 10kts (500 cm/s) with a heading offset of 1 degree are 8.7 cm/s and roughly $.018 \times u$, respectively. Table 1 lists errors for several heading offsets and cross-track velocities to demonstrate the range of errors to be expected. The error is much more significant in the cross-ship component, and increases with the ship's speed. Table 1 uses 500 cm/s for v throughout, because this is a typical ship's speed, and would be the major portion of relative velocity in the along-track direction.

Compass checks between the ship's gyro and the ADCP computer were logged daily from the beginning of the cruise until 14 February. The next recorded compass check was on 22 February. The maximum error recorded on these checks was 1.3° during a period of rough weather, with all others being 1° or less. The one recorded compass check against the sun was within 0.5° . According to Pollard and Read (1989), ship gyros can experience a drift of up to 2° during large turns, and ADCP data should be discarded for 10-15 minutes after such turns. Although they were not frequent, there were several major turns during ADCP data collection on this cruise. No special treatment of the data accounted for possible drifting errors after these turns. The ADCP log noted that the gyro experienced no apparent slippage through a 90 degree turn on 29 January.

The major source of error in question with this data is the alignment of the transducer with the ship's hull. During the cruise, the transducer "slewed" out of alignment rather drastically on two occasions. These incidents were recorded and have been corrected for in the data. The transducer was normally locked into the hull with a key-like arrangement which allowed less than a degree of rotation when properly installed. We speculate that on the occasions when the transducer slewed drastically out of alignment, it had not been properly locked in. The probability that the transducer

was improperly installed on other occasions, allowing undetected rotation, is not known. Based on the assumption that both the transducer and the gyro had up to 1-degree misalignments, the total rms alignment error is estimated to be 1.4°, resulting in approximately a 13 cm/s velocity error.

Incorrect navigation fixes also cause errors in the final absolute ADCP velocities. The distance between the fixes and the final smoothed ship track is useful in roughly estimating velocity errors due to fix error. This distance actually represents a combination of fix error and smoothing, but can give a conservative estimate of the fix error. The standard deviation of this distance for the Agulhas cruise was used to generate a random distribution of fixes about a given point. Assuming the distance was due completely to fix error, this simulated a time series one might have obtained by recording fixes while the ship was in port. The series of fixes was then differenced and divided by the time between TRANSIT fixes to obtain velocities generated by the fix offsets. The Blackman and Tukey filter was then applied to the resultant u and v velocities. The mean velocities calculated using this process were 1.8 and 1.0 cm/s in the x and y directions, respectively. These velocities are an estimate of the errors induced by the TRANSIT fix inaccuracies.

Finally, several factors can contribute to calibration errors in estimation of the ship's speed. These include errors in the speed of sound and oscillator frequency and errors from scattering of the acoustic beams as a result of the ship's acoustic environment. These errors have a negligible impact on ADCP velocities compared to navigation and misalignment errors.

Combining the estimates for known potential errors, the rms accuracy of this ADCP data is roughly ± 13 cm/s.

5. Initial ADCP results

A multi-purpose program (called ADCPSECT) was used to extract profiles, average them over desired grids and plot the velocities. ADCPSECT was configured to reject all data from depth bins for which the percent good pings fell below 50 percent. The ship track was divided into 10 sections which are shown in Fig. B-8.

Fig. B-10 displays absolute currents computed from the ADCP data in vector form. Data were averaged horizontally over a 0.25 degree latitude and longitude grid and vertically over the depth range shown in each plot. Vectors display plausible directions and velocities for the Agulhas Retroflexion area. Some eddy-like features are evident near the southern tip of what appears to be the retroflexion (along sections 9 and 10 in Fig. B-8).

Two sets of crosstrack countour plots of the data are shown in Fig. B-11. Data were averaged horizontally over 0.1 degrees latitude or longitude (which ever was along track) and in 10 meter

vertical increments. One set shows absolute velocity computed using navigation data as discussed in section 3. The second set shows relative velocity referenced to 200 meters for comparison with the geostrophic crosstrack velocity contours computed by Read, Pollard and Smithers (1987) from SEASOAR data taken along the same ship track. Although the exact velocities do not always agree, the current structure of the plots referenced to 200 meters is very close to that of the published contours.

Fig. B-9. Average reference layer velocity between fixes (piecewise constant) and final, smoothed reference layer velocity. A + underneath the velocity plot indicates a gap in ADCP data. The lower half of each page shows the latitude and longitude of the ship from combined GPS and TRANSIT fixes. A two day interval is shown on each page, with time given in decimal days (time in days measured from 0000 on January 1). These plots are useful in evaluating the quality of navigation information and the resolution of the data based on distance between fixes (see section 3.4 of text).

Fig. B-10. Absolute current velocity vectors computed from the ADCP data. Vectors represent data averaged horizontally over a 0.25 x 0.25 degree grid in latitude and longitude and over the indicated depth range vertically.

Fig. B-11. Two sets of contoured velocities, one set of absolute velocities and one set of relative velocities referenced to 200 meters. Both cross-track and along-track velocities are shown. Contour plots are averaged over 0.1 degree of latitude or longitude (which ever is along track) and over 10 meter depth increments. Contours are plotted along straight segments of the cruise track shown in figure B-8 (from Read *et al.* (1987)). The vertical axis is depth in meters.

Table B-1. Velocity errors resulting from misalignment. n is counter-clockwise offset angle of gyro from ship's true heading or of ship's heading from transducer alignment. u and v are measured cross- and along-track velocities in cm/s. u' and v' are velocities in the rotated coordinate system.

n	u	v	$u' - u$	$v' - v$
1	50	500	8.74	0.975
1	100	500	8.73	1.850
1	150	500	8.72	2.725
1	200	500	8.71	3.600
2	50	500	17.42	2.045
2	100	500	17.39	3.790
2	150	500	17.36	5.535
2	200	500	17.33	7.280
5	50	500	43.41	6.260
5	100	500	43.22	10.620
5	150	500	44.03	14.980
5	200	500	42.84	19.340

REFERENCES

- Bahr, F., E. Firing, and J. Songnian, "Acoustic Doppler Current Profiling in the western Pacific during the US-PRC TOGA cruises 2, 3 and 4," Contribution No. 89-0175, Data Report No. 005, Joint Institute for Marine and Atmospheric Research University of Hawaii, 1989.
- Caruso, M., Z. Sirkes, P. Flament, and M. Baker, "Altimeter processing tools for analyzing mesoscale ocean features," Tech. Rep. WHOI-90-45, pp. 1-200, Woods Hole Oceanographic Institution, 1990.
- Cheney, R.E., B.C. Douglas, R.W. Agreen, L. Miller, D.L. Porter, and N.S. Doyle, "GEOSAT altimeter geophysical data record user handbook," NOAA Tech. Memo. NOS NGS-46, 1987.
- Cheney, R.E., B.C. Douglas, and L. Miller, "Evaluation of GEOSAT altimeter data with application to tropical Pacific sea level variability," *J. Geophys. Res.*, vol. 94, pp. 4737-4747 (1989).
- D'Asaro, E.A. and H. Perkins, "A near-inertial internal wave spectrum for the Sargasso Sea in late summer," *Journal of Physical Oceanography*, vol. 14, pp. 489-505 (1984).
- Flament, P., D. Jarman, P.M. Kosro, and G. Mitchum, "Remarks on using polynomial models for the orbit error of altimetry satellites," *J. Geophys. Res.* (1991). (submitted)
- Flament, P., P.M. Kosro, and A. Huyer, "Mesoscale variability off California as seen by the GEOSAT altimeter," *Proceedings of IGARSS'89*, pp. 1063-1068, I.E.E.E. (1989).
- Gill, A.E., *Atmosphere-ocean dynamics*, Academic Press, Inc., New York.
- Harris, T.F.W., R. Legeckis, and D. VanForest, "Satellite infra-red images in the Agulhas current system," *Deep-Sea Research*, vol. 25, pp. 543-548 (1978).
- Irvine, D.E., "Extreme waves in the Agulhas - a case study in wave-current interaction," *Johns Hopkins APL Technical Digest*, vol. 8, no. 1, pp. 100-106 (1987).
- Joyce, T.M., K.A. Kelly, D.M. Schubert, and M.J. Caruso, "Shipboard and altimetric studies of rapid Gulf Stream variability between Cape Cod and Bermuda," *Deep-Sea Res.*, vol. 37, No. 6., pp. 897-910 (1990).

- Joyce, T.M. and M.C. Stalcup, "An upper ocean current jet and internal waves in a Gulf Stream warm core ring," *J. Geophys. Res.*, vol. 89, pp. 1997-2003 (1984).
- Kosro, P.M., "Shipboard acoustic current profiling during the Coastal Ocean Dynamics Experiment," 85-8, Scripps Institution of Oceanography, 1985.
- Luyten, J., A. Spencer, S. Tarbell, K. Luetkemeyer, P. Flament, and J. Toole, "Moored current meter, AVHRR, CTD and drifter data from the Agulhas current and retroflexion region (1985-1987), vol XLII," WHOI-90-30, Woods Hole Oceanographic Institution, 1990.
- Mallory, J.K., "Abnormal waves on the South East coast of South Africa," *Int. Hydrogr. Rev.*, vol. 51, pp. 99-129 (1974).
- Neumann, G. and W.J. Pierson, Jr., *Principles of physical oceanography*, Prentice-Hall Inc., Englewood Cliffs, NJ (1976).
- Pollard, R. and J. Read, "A method for calibrating shipmounted Acoustic Doppler Profilers and the limitations of gyro compasses," *Journal of Atm. and Ocn. Tech.*, vol. 6, No. 6, pp. 859-865 (1989).
- Pollard, R.T., "On the generation by winds of inertial waves in the ocean," *Deep-Sea Res.*, vol. 17, pp. 795-812 (1970).
- Pollard, R.T. and R.C. Millard, Jr., "Comparison between observed and simulated wind-generated inertial oscillations," *Deep-Sea Res.*, vol. 17, pp. 813-821 (1970).
- Pollard, R.T., J.F. Read, J. Smithers, and M.W. Stirling, "SEASOAR sections from the Antarctic Circumpolar current at 52S, 32E to the Subtropical front at 37S, 52E," Report No. 244, Institute of Oceanographic Sciences, Wormley, 1987.
- Pond, S. and G.L. Pickard, *Introductory dynamical oceanography*, Pergamon Press, Oxford (1983).
- R.J.Slutz,, S.J.Lubker, J.D. Hiscox, S.D. Woodruff, R.L.Jenne, D.H.Joseph, P.M.Steurer, and J.D. Elms, *Comprehensive ocean-atmosphere data set, release 1*, Boulder, Colorado (1985).
- Read, J.F., R.T. Pollard, and J. Smithers, "CTD and Seasoar data from the Agulhas retroflexion zone," Report No. 245, Institute of Oceanographic Sciences, Wormley, 1987.
- Stewart, R.H., *Methods of satellite oceanography*, University of California Press, Berkeley and Los

Angeles (1985).

Unesco,, "Tenth report of the joint panel on oceanographic tables and standards," *Unesco Technical Papers in Marine Science*, no. 36, p. 24 (1981).